PONTIFICIA UNIVERSIDAD CATOLICA DE CHILE
SCHOOL OF ENGINEERING

1-G PHYSICAL MODELING OF DYNAMIC SOIL-STRUCTURE INTERACTION FOR SEMI-BURIED STRUCTURES USING CONTINUOUS MONITORING IN SPACE AND TIME

HUGO JAVIER SEGALINE BUSTAMANTE

Thesis submitted to the Office of Graduate Studies in partial fulfillment of the requirements for the Degree of Doctor in Engineering Sciences

Advisor:
ESTEBAN PATRICIO SÁEZ ROBERT

Santiago of Chile, September 2022

PONTIFICIA UNIVERSIDAD CATOLICA DE CHILE
SCHOOL OF ENGINEERING

1-G PHYSICAL MODELING OF DYNAMIC SOIL-STRUCTURE INTERACTION FOR SEMI-BURIED STRUCTURES USING CONTINUOUS MONITORING IN SPACE AND TIME

HUGO JAVIER SEGALINE BUSTAMANTE

Members of the Committee:

ESTEBAN SÁEZ

FERNANDO LOPEZ-CABALLERO Fernando Lopez Caballero

JOSÉ LUIS ALMAZÁN Jose Luis Almazan

JAVIER UBILLA Javier Ubilla V

JUAN CARLOS TIZNADO Juan Carlos Tiznado Aitken

JUAN DE DIOS ORTÚZAR

Thesis submitted to the Office of Graduate Studies in partial fulfillment of the requirements for the Degree of Doctor in Engineering Sciences

Santiago of Chile, September 2022

Gratefully to my parents who have been my inspiration.

ACKNOWLEDGEMENTS

I would like to thank all those who have collaborated in the development of this Thesis. Particularly to the Chilean National Research and Development Agency (ANID) through the National Doctoral Scholarship number 21161061 and the FONDECYT project 1200324.

I would like to express my sincere appreciation to my advisor Dr. Esteban Sáez, from whom I have received all the support and encouragement to successfully complete my PhD studies. It was a great honor to have the opportunity to work with him and learn from his great knowledge. I would also like to thank the members of the committee: Dr. Javier Ubilla, Dr. Fernando López-Caballero, Dr. José Luis Almazán, Dr. Juan Carlos Tiznado and Dr. Juan de Dios Ortúzar for their advice and recommendations in preparing this Thesis document. I also express my gratitude to Professor Dr. Nawawi Chouw who integrated me into his research team during my internship at The University of Auckland, New Zealand.

To the school of engineering of the Pontificia Universidad Católica de Chile for accepting me and giving me the opportunity to expand my knowledge.

Many thanks to Professors Dr. René Espinoza and Dr. Mauricio Prudencio for encouraging me to start my postgraduate studies.

My entire family who gave me all their support during these years. Special thanks to my father Javier, my mother Gloria and my uncle Luis for providing me the confidence I needed to finish my studies.

Finally, I would like to thank my friends who have collaborated and given me all their support during this research: Claudio Fernández, Ricardo Gallardo, Camilo Guzmán, Jairo Rojas, Valeria Soto, Nicolás Tapia and Miguel Valencia. Particularly thanks to Belén Llanquilef and Francisco Zamorano who collaborated with me during this research and gave me their unconditional support, suggestions and advice.

TABLE OF CONTENTS

LIST OF TABLES

LIST OF FIGURES

ABSTRACT

Dynamic soil-structure interaction (DSSI) has been a topic of great interest during the last decades. Several investigations have shown the importance of considering the soil as part of the structural design evaluation, since the response of the structure can be strongly influenced by the soil depending on its properties. In common practice, it is often believed that neglecting the effects of DSSI invariably leads to conservative design. However, several studies have shown that this hypothesis is not necessarily true, since there are many factors to be considered. Therefore, various strategies, including numerical, analytical or physical modeling, have been developed to study different aspects of the DSSI phenomenon.

This research is based on the development of a new laminar box able to approximately simulate the lateral boundary conditions of the soil. The main characteristic of this laminar container is the transparency of its front side. This feature allows a complete visualization of the soil and its interaction with different semi-buried structures considering a 2D analysis through the digital image correlation (DIC) technique. In addition, the dynamic pressure distribution is obtained by means of a tactile sensor, which allows correlating the displacement images with the pressure pattern developed in the partially buried structures.

For the basements of shear-wall buildings, it was found a direct relation between the kinematic interaction effects and the seismic thrust exerted on the walls. For the retaining walls systems, a variation in time of the active wedge shape as a function of the input magnitude was found. Finally, for both the underground walls and the retaining walls, the pressure distribution for different design configurations is presented as a function of the embedment depth and the frequency content of the input.

Keywords: Dynamic soil-structure interaction, Digital image correlation (DIC), Non-linear soil behavior, Physical modeling, Numerical modeling, Retaining wall, Underground stories, Shaking table, Transparent laminar box

RESUMEN

La interacción dinámica suelo-estructura (DSSI) ha sido un tema de gran interés durante las últimas décadas. Varias investigaciones han demostrado la importancia de considerar el suelo como parte del diseño estructural, ya que la respuesta de la estructura puede estar fuertemente influenciada por el suelo en función de sus características. Por el contrario, en la práctica común se suele despreciar los efectos del DSSI pues se asume que es una hipótesis invariablemente conservadora, sin embargo, varios estudios revelan que esta hipótesis no es necesariamente cierta ya que hay varios factores a considerar. Por ello, a lo largo del tiempo se han desarrollado diferentes estrategias, ya sea de modelización numérica, analítica o física, para estudiar distintos aspectos del fenómeno DSSI.

Esta investigación se basa en el desarrollo de un nuevo dispositivo de caja laminar capaz de simular las condiciones de contorno lateral del suelo. La principal característica de este contenedor laminar es la transparencia de su parte frontal, lo que permite una visualización completa del suelo y su interacción con las estructuras semienterradas considerando un análisis 2D a través de la técnica de correlación de imágenes digitales (DIC). Además, la distribución de la presión dinámica se obtuvo mediante un sensor táctil, que permite correlacionar las imágenes de desplazamiento con el patrón de presión en las diferentes estructuras parcialmente enterradas.

Para el caso de los pisos subterráneos de edificios de muros de corte, se verificaron los efectos de interacción cinemática y su relación con la fuerza ejercida sobre estos muros. Para el caso de muros de contención, se evaluó la variación en el tiempo de la forma de la cuña activa como función de la amplitud del movimiento dinámico. Finalmente, tanto para los muros subterráneos como para los muros de contención, se presenta la distribución de presiones para diferentes configuraciones de diseño en términos de profundidad de enterramiento y contenido frecuencial de la carga.

Palabras Clave: Interacción dinámica suelo-estructura, Correlación de imágenes digitales (DIC), Comportamiento no lineal del suelo, Modelación física, Modelación numérica, Muro de retención, Pisos subterráneos, Mesa vibrante, Caja laminar transparente

1. INTRODUCTION AND MOTIVATION

Nowadays it is frequent to find partially buried structures in cities. One of the main reasons is the constant increasing of urban population accompanied by their demand for more living spaces. This need has promoted the construction of tall buildings with several underground stories for parking, usually associated with the execution of deep excavations in urban environments. This type of structures require the development of new or updated construction and analysis methodologies to meet the safety requirements. Among these buried structures, two types are of special interest as they are very frequent: (1) Buildings with basement stories and (2) Soil retaining systems. Both have in common that a large part of the structure is buried and in contact with the soil, which makes the system highly influenced by the soil-structure interaction. In a highly seismic country like Chile, the dynamic component of this interaction is particularly complex and difficult to evaluate.

Generally, this kind of structures do not receive the special attention that they require, since commonly used design procedures are assumed to lead to conservative designs. Indeed, seismic analysis of buildings with basements has been adapted from the shallow foundation theory, and the lateral confinement of the soil is ignored. Therefore, different strategies have been assumed to simplify this problem, one of the most common is to consider a fixed base foundation with no interaction with soil. However, it is not clear how conservative this approach can be, in fact, depending on the aspect ratio of the building and other parameters, it may not be conservative.

Throughout the years, there have been significant earthquakes that have prompted the improvement of seismic design of engineering structures. In general, all structures are prone to the interaction with the soil and, under seismic or vibratory conditions, this phenomenon is denominated Dynamic Soil-Structure Interaction (DSSI). Important seminal contributions were made that helped to understand the nature of this interaction (e.g. Luco & Contesse, 1973; Veletsos & Verbič, 1973; Bielak, 1974; Chopra & Gutierrez, 1974; Seed & Lysmer, 1977; Luco, 1980; Kausel, 1981; Bielak & Christiano, 1984; Wolf & Obernhuber, 1985; Dobry et al., 1987). In general, the phenomenon of DSSI can be divided into two types of interaction: kinematic interaction (KI) whose main characteristic is the incompatibility of motion between the soil and the structure due to their significant difference in stiffness, and inertial interaction (II) where the translational and rotational forces are transferred from the structure to the soil due to the incorporation of soil flexibility. As a result of both interactions, the soil behaves differently when in contact with a structure, and at the same time the response of such structure is conditioned to the surrounding soil. As a consequence, a lengthening of the first vibration mode and a damping increase in buildings have been identified as the most common effects of DSSI (e.g. Stewart, Fenves, et al., 1999; Stewart, Seed, et al., 1999). However, for the case of embedded foundations, previous work have observed a reduction in natural period of vibration due to the increased stiffness of the foundation (Todorovska, 1992). Avilés & Pérez-Rocha (1996) reported no major changes in the natural period and damping of the system when considering only inertial effects. Therefore, it seems that an accurate analysis of the DSSI effects must include both inertial and kinematic effects (Avilés & Pérez-Rocha, 1998). Partially buried structures caught the attention of many researchers through the development of numerical (FEM) or analytical models (Asadi-Ghoozhdi & Attarnejad, 2020; Bararnia, Hassani, Ganjavi, & Amiri, 2018; Didier Clouteau, Broc, Devésa, Guyonvarh, & Massin, 2012; Riccardo Conti, Morigi, & Viggiani, 2017; Fu, Liang, & Han, 2017; Fu, Todorovska, & Liang, 2018; Lin & Jennings, 1984; Mahmoudpour, Attarnejad, & Behnia, 2011; Mahsuli & Ghannad, 2009; Politopoulos, Sergis, & Wang, 2015; Saxena & Paul, 2012; Sotiriadis, Klimis, Margaris, & Sextos, 2020; Takewaki, Takeda, & Uetani, 2003; H. feng Wang, Lou, Chen, & Zhai, 2013). While most building codes and guidelines describe the KI and II interactions already mentioned, inertial interaction (II) effects are generally given greater importance in the analyses (FEMA P-2082-1, 2020). In contrast, the ASCE (2017) defines the interaction effects only in terms of kinematic interaction (KI). Nevertheless, for a more specific analysis, recommendations and practical applications can be found in guides such as FEMA P-2091 (2020). Additionally, it has been shown that a nonlinear approach provides a more realistic evaluation of the DSSI problem (Çelebi, Göktepe, & Karahan, 2012; Chau, Shen, & Guo, 2009; Jardine, Potts, Fourie, & Burland, 1986; Pecker, Paolucci, Chatzigogos, Correia, &

Figini, 2014; Romero, Galvín, & Domínguez, 2013; Sáez, Lopez-Caballero, & Modaressi-Farahmand-Razavi, 2011).

In addition to buried buildings, “yielding” retaining systems are characterized for having larger displacements when compared to basement walls (non-yielding retaining systems). Under dynamic conditions, the complexity of the problem increases since the retaining walls are usually designed from static equilibrium equations corresponding to Coulomb`s theory and pseudo-static extensions to approximate dynamic loads. Based on the damage caused by large earthquakes (e.g. the Great Kanto Earthquake, Japan, 1923), Mononobe (1929) and Okabe (1924) developed a pseudo-static strategy that extended the original Coulomb’s equations of limit equilibrium, obtaining the induced force exerted by the “dynamic” pressures on the wall. The applicability of these equations has been discussed for many years, however their use in international design guidelines, for instance NCHRP (Anderson, 2008) is still prevalent. Commonly, these structures are designed using the limit-state theory (Mononobe, 1929; Mylonakis, Kloukinas, & Papantonopoulos, 2007). However, different alternative approaches have been reported, such as linear-elastic methods (Wood, 1975; Sherif et al., 1984; A. Veletsos & Younan, 1994; Veletsos & Younan, 1997) or pseudo-dynamic analysis (Bellezza, 2014, 2015; Choudhury & Nimbalkar, 2006).

Given the difficulty of these structural systems, several strategies have been developed to estimate these DSSI effects, either through analytical or semi-analytical methodologies, computational strategies, or physical models. Since the focus of this thesis is the physical modeling of the problem, such strategy is described in the section **1.2**.

1.1 Analytical and numerical method in DSSI

Thanks to the rapid advance of computational capabilities, currently there are much more sophisticated computational tools that allow the development of numerical FEM models that perform the evaluation of the soil-structure system (Figure 1-1a). Among the main strategies to address the DSSI phenomena standout: (i) **the direct method**, which is

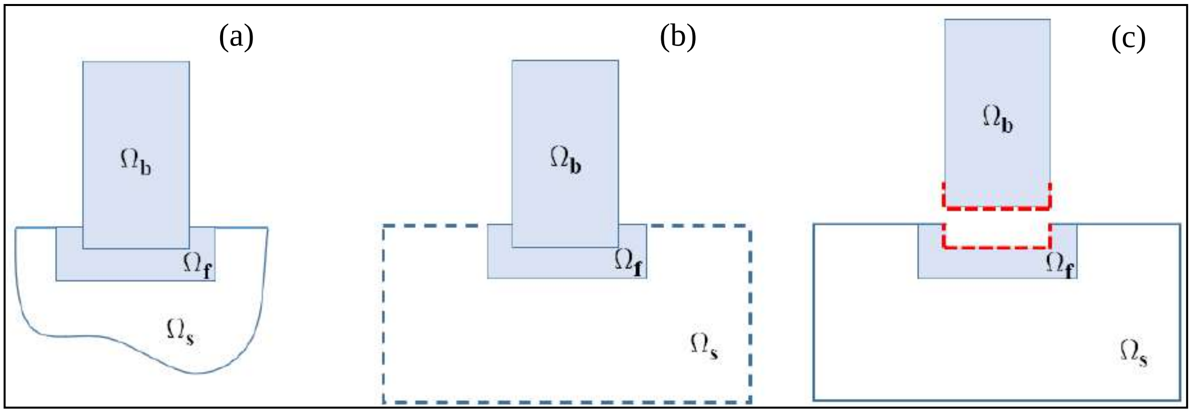

Figure 1-1: (a) Global model; (b) Direct method; (c) Substructure method

characterized by the development of an artificial boundary that includes both the soil and the structure (Figure 1-1b). This method must deal with the treatment of boundaries capable to dissipate partially or totally the waves propagating outward. In principle, to solve this issue, the size of the soil domain ($\mathbf{\Omega}_S$) had to be large enough to prevent contamination of the dynamic response of the near field by reflected waves. However, this idea led to significant computational costs. In this way, a variety of boundary conditions, capable to absorb energy, have been developed with the purpose of imitating an infinite half-space. The most common boundary conditions that may be encountered are: (a) viscous boundary, which can absorb the reflected waves since it is based on viscous dampers. This boundary condition is expressed in terms of normal and shear stress (Lysmer & Kuhlemeyer, 1969); (b) superposing boundaries, are established from the analysis of two boundary conditions, i.e., Dirichlet and Neumann solutions (Smith, 1974); (c) paraxial boundaries, where a dynamic impedance is approximated locally in space and time (R. Clayton & Engquist, 1977); (d) transmitting boundary based on the extrapolation of the boundary (Liao & Wong, 1984); (e) viscous-spring boundary, that is based on the plane strain boundaries with the particularity of being a frequency-independent model (Deeks & Randolph, 1994); (f) Perfectly Matched Layers (PML) introduced by Berenger (1994), based on material layers that have absorbing attributes. Other discretized formulations such as Perfectly Matched Discrete Layers (PMDL) were developed for the implementation on finite element models (Guddati & Tassoulas, 2000) and for DSSI nonlinear problems (Lee et al. 2014). More recently, Nguyen & Kim (2018) incorporated analytical wavelengths into the PMDL method for frequency domain analysis (AW-PMDL).

For the direct method, the DSSI study can be performed through commercially available software that have the numerical implementation of the above-mentioned models, just to mention some of them: ABAQUS®, PLAXIS® and ANSYS®, while other software stand out for having specific tools to address DSSI problems such as MTR/SASSI® or LS-DYNA®, the latter is based on the effective seismic input method, which considers the scattered waves and the PML method.

Another analysis method is (ii) **the substructure method**, which is strongly related to the boundary element method (BEM). This approach separates the analysis of DSSI into inertial and kinematic interaction and solve the equations by the superposition principle (Figure 1-1c). These equations are generally based on Green's functions and are characterized by their high complexity. Although this method has been mostly used for linear systems, different strategies to perform nonlinear analysis have been addressed (Lysmer & Richart Jr, 1966; Kutanis & Elmas, 2001; Kim et al., 2016; Liu et al., 2019). The interface between soil and structure is modeled by impedance functions and is expressed in the frequency domain. Although there are alternatives, which are called frequency-time domain approaches; they are the basis for the boundary reaction method (BRM) (Kim et al., 2016). This type of analysis is considered rigorous, since it satisfies by its formulation the energy radiation condition, producing radiation damping on the system.

Generally, these numerical formulations are characterized by a high computational cost. The models can run for weeks depending on their size and the hardware resources. On the other hand, physical modeling is characterized by a much more representativeness of the complexities of the problem, although it also has some disadvantages. These will be discussed in the following section.

1.2 Physical modeling in DSSI

As a way of improving the understanding of complex physical phenomena, it has been implemented the concept of physical models in controlled environments, which consist of representing the main characteristics of a prototype in a reduced scale with greater control over the variables affecting the problem. This type of approach has been used for decades in geotechnical engineering due to the complexity of the soil behavior. In the case of seismic problems, to simulate the boundary conditions of the soil, laminar containers are usually employed to mimic the lateral flexibility of the soil in the field (Dietz & Muir Wood, 2007; B. Jafarzadeh, 2004; Prasad, Towhata, Chandradhara, & Nanjundaswamy, 2004; Tabatabaiefar, 2016; Turan, Hinchberger, & El Naggar, 2009; D. M. Wood, Crewe, & Taylor, 2002). The use of these kind of devices has driven valuable research in the field of DSSI (Abate, Massimino, Maugeri, & Wood, 2010; Hokmabadi, Fatahi, & Samali, 2014; Meymand, 1998; Pitilakis, Dietz, Wood, Clouteau, & Modaressi, 2008; Rayhani & El Naggar, 2012; Z. Zhang, Wei, & Qin, 2017).

There are two main strategies for performing laminar box testing of geotechnical systems, differentiated by the confining pressure to which the model is subjected through variations of the gravitational acceleration: n-g tests and 1-g tests.

In the centrifugal n-g testing, the gravity and the unit weight of the soil are increased, until the actual confining stresses of the model are similar to the prototype. Much of the development of physical models in geotechnical engineering comes from centrifugal modeling, which is preferred because it preserves the stress state of the soil during the experiment (e.g. Bolton & Steedman, 1982, 1985; Ortiz et al., 1983; Steedman & Zeng, 1990; Dewoolkar et al., 2000; Nakamura, 2006; Al Atik & Sitar, 2010; Geraili Mikola et al., 2016).

For a 1-g environment, the use of semi-buried physical models has also been explored. For the case of buildings with underground stories, many experiments are focused on the evaluation of the structural response (Turan, Hinchberger, & El Naggar, 2013), since the soil surrounding the basement walls can only be instrumented locally, losing valuable information in the continuous space, for instance, the pressure distribution on basement walls, which is rarely studied. In contrast, the case of retaining systems has received more attention (e.g. Matsuo & Ohara, 1960; Sherif et al., 1982, 1984; Ishibashi & Fang, 1987) because the failure mechanism is highly influenced by the pressure distribution and seismic induced force. In addition, other parameters have also been investigated, such as the modification of geometric features to improve the performance of these walls (Gao, Hu, Wang, Wang, & Chen, 2017), or in some cases it has been explored the reinforced retaining walls (Madhavi Latha & Murali Krishna, 2008; Panah, Yazdi, & Ghalandarzadeh, 2015). However, documentation referred to seismic induced forces and pressure distribution is scarce. Some physical models have attempted to evaluate these variables using pressure transducers (Wilson & Elgamal, 2015). These works, as a qualitative approach, can be very useful, but a more precise vision through a continuous analysis is still needed considering the induced seismic forces and the pressure distribution in both basement walls and retaining systems. Both still need further investigation of their influence on the DSSI.

The role of physical modeling in geotechnical engineering has been crucial in many aspects, as it has contributed to the understanding of complex factors involved in soil-structure interaction. This effort to understand the dynamic response of the system has promoted the development of new technologies in sensing and data acquisition, to retrieve more and better-quality information. This investigation combines different data acquisition systems rarely used before in geotechnical engineering applications, especially for dynamic testing. Thanks to the development and construction of an innovative laminar shear box and the use of modern instrumentation, it is possible to evaluate the dynamic pressure distribution for both: (a) the wall basement in buildings, and (b) the retaining systems.

The experimental validation of the laminar container by the nonlinear characterization of the soil was developed in ***Paper I***, already published in Acta Geotechnica journal. Thanks to the capabilities of this device, the relation between dynamic pressures and the full field motion in the surrounding soil tracked by high-speed digital image correlation was studied.

The case of scaled shear wall buildings with underground stories is presented in ***Paper II***, while ***Paper III*** summarizes the study performed in the case of partially embedded yielding retaining system. In all these papers, Ricker wavelets were used as input motions to simplify the interpretation and preserve the seismic equivalence in terms of amplitude and frequency content.

1.3 Hypothesis and Objectives

The main hypothesis is that the effects of DSSI can be estimated from physical experimentation using small-scale models in a laminar box and a shaking table at 1-g. In addition, the transparent sidewall of the laminar box will allow tracking the soil motion in an unprecedented way and relating it to other measurements performed during the tests.

The general objective of this investigation is to evaluate the dynamic soil-structure interaction effects in buildings with underground stories and a retaining wall system, considering the soil non-linear behavior.

The specific objectives are the following:

1. Design, construct, and validate of a new transparent laminar box, as a tool for the analysis of the non-linear soil behavior during dynamic testing in a 1-g shaking table (***Paper I***).

2. Evaluate the effects of DSSI using a scaled building with underground stories in the physical model (***Paper II***).

3. Evaluate the effects of DSSI using a scaled retaining wall system in the physical model (***Paper III***).

4. Carry out numerical models reproducing the physical models using the finite element method for the studied configurations (***Paper I*** and ***III***).

1.4 Scope of work

This investigation is intended to determine the DSSI effects of partially buried structures. For this purpose, a sequence of steps were followed. Initially, the design and construction of a new laminar box was completed. The box was filled with clean natural sand without fines and, mounted on a shaking table to test the system under a wide range of amplitudes and frequencies, allowing the evaluation of the non-linear soil behavior. These results were compared with the standard laboratory tests for validation purposes. Then, physical models were built following widely accepted similitude laws to represent the dynamic characteristics of prototype configurations. For the case of buildings with underground stories, it was measured the pressure distribution acting on the basement walls during dynamic testing, this distribution was complemented with the Digital Image Correlation (DIC) technique, where the soil motion was measured. In the same way, for the case of retaining systems, the active and passive thrusts were studied from Ricker wavelet inputs covering a wide range of amplitudes. Finally, numerical validation was made for the laminar box and the retaining systems.

1.5 Methodology

The tests were conducted using a shear laminar box (Figure 1-2). This novel device was made of tempered glass in the front side making it transparent. This allows full visualization of the soil inside, along with any structure placed in the container in contact with the glass. This way, it is possible to compute the soil particles displacement, velocity, and acceleration field through the DIC technique. The configuration of each experiment can be found in the following chapters. Below, the procedure is explained in general terms.

The shaking table used in this investigation has 1 degree of freedom (1-DOF), achieving a maximum acceleration of 1-g. The operational range of displacement has a mean of ± 450 mm and can handle up to 2000 kg payload. The servo-hydraulic table was designed by ANCO Engineers Inc. Most of the tests described in the following chapters are subjected to Harmonical signals and Ricker wavelets. The latter due to the seismic equivalence that the signal has compared to real earthquakes in terms of maximum amplitude and frequency content. Wavelets also reduce the duration of the tests, simplify the interpretation of results and reduce the computational cost of image analysis.

Figure 1-2: Transparent laminar box

DIC technique is a valuable tool to track the particles displacement and study the non-linear soil behavior. Different configurations and camera arrays were used to improve the data acquisition in each experiment (Figure 1-3). As the tests are performed under dynamic conditions, they require a high rate of frames to have a good description of the model's movement. All tests were recorded at 60 frames per second (fps). This sampling rate allowed to obtain results up to a maximum frequency of approximately 20 Hz. On the other hand, the resolution of images depends on the system configuration. For the initial experiments, a 2.7k resolution was set up (i.e., 2704 x 1520 pixels), while for DSSI tests, a resolution of up to 4k was used (i.e., 3840 x 2160 pixels). Additionally, all pressure maps were measured using a tactile pressure sensor (TekScan®), which consists of a grid of highly sensitive piezoelectric cells. This tactile sensor is placed between the soil and the structure. The sampling rate for this sensor was 100 Hz.

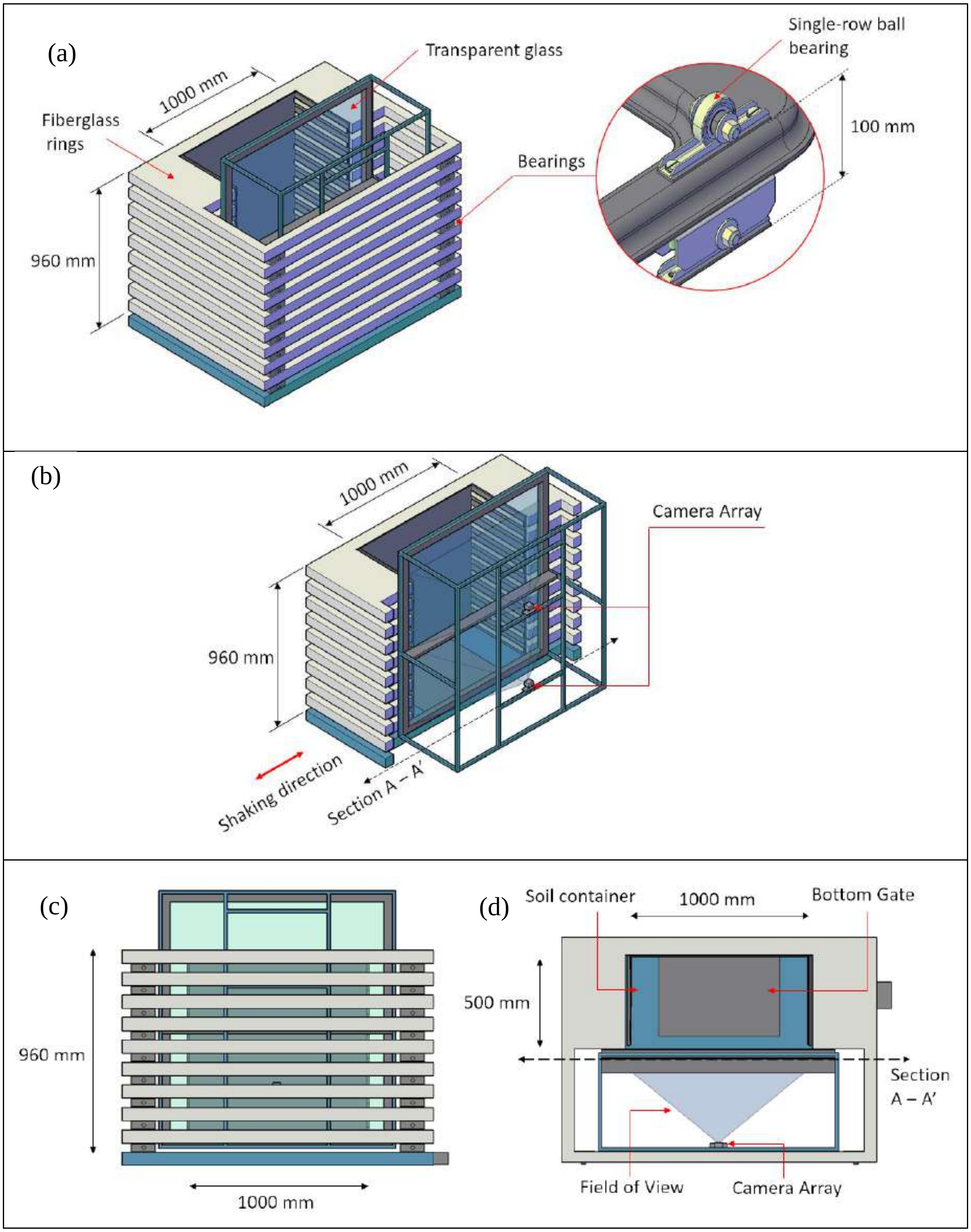

Figure 1-3: Drawings of the transparent laminar box: (a) Isometric view; (b) Section A-A' and camera array distribution; (c) Front view; (d) Plan view

The main devices and analysis tools used for this research were described above. Hereinafter, the procedure for the development of physical experimentation is described in general terms as follows: (a) The first step consists of placing the accelerometers as the sand is placed into the laminar box. The relative density control method depends on the type of test to be performed, as described below. (b) Then, in the case of the physical models corresponding to the scaled buildings, the tactile pressure sensor is placed on the walls of the underground stories. For the case of retaining systems, the tactile sensor covers both active and passive sides of the wall. (c) After installing all sensors, the model is located in the laminar container. (d) The camera array is synchronized and installed equidistantly from the transparent wall of the laminar box. (e) Once the set-up is complete, the tests are conducted, which depending on their characteristics (i.e., destructive or non-destructive), the assembly must be performed again at the end of the test. The general assembly scheme is described in Figure 1-4.

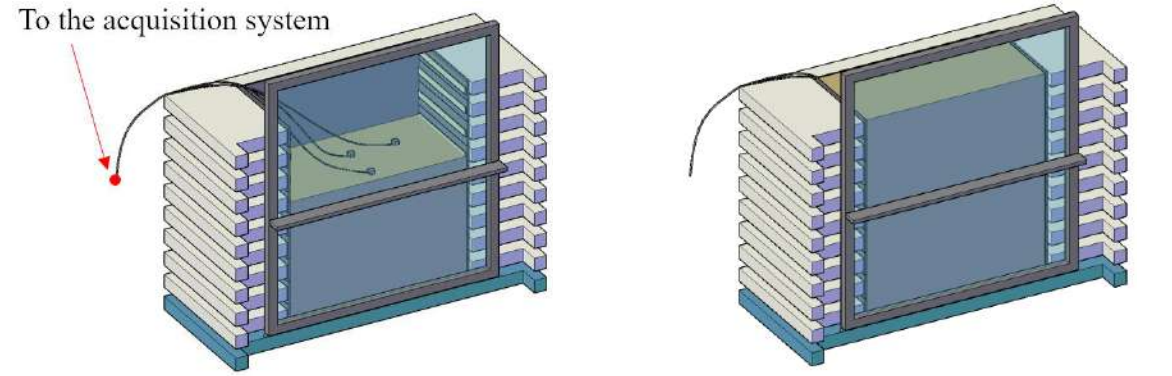

(a) Installation of accelerometers and placement of soil

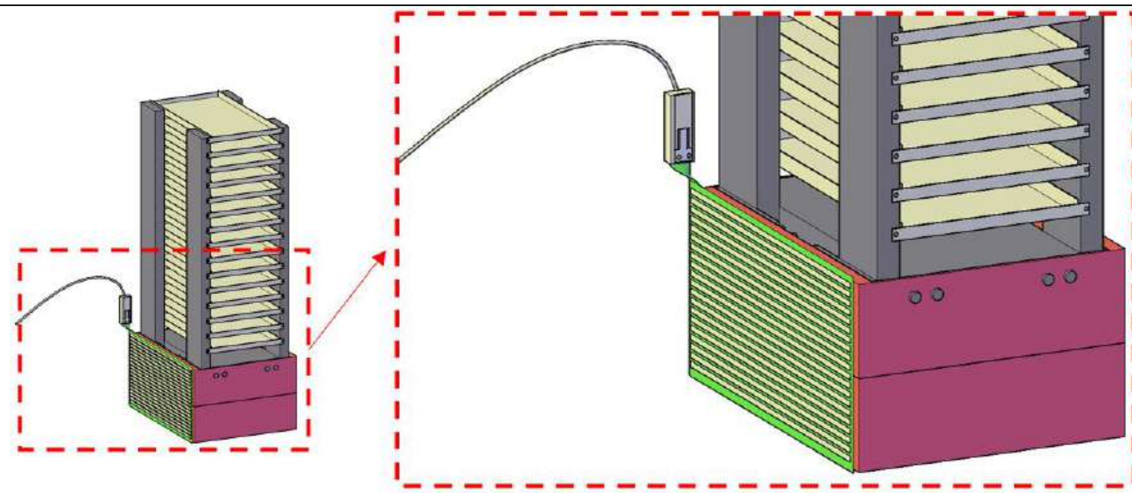

(b) Installation of pressure sensor

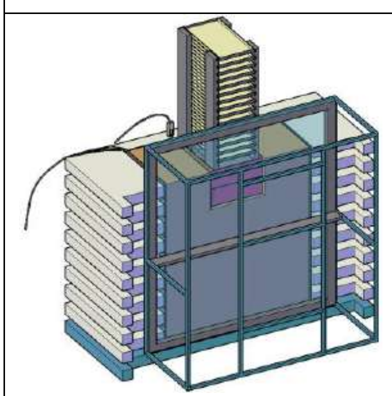

(c) Physical model placement

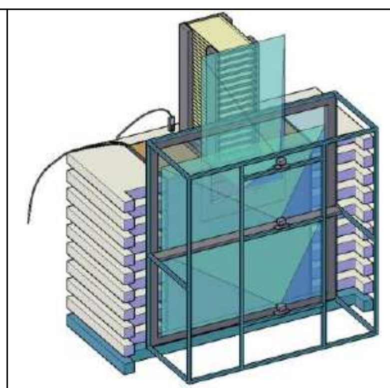

(d) Camera array

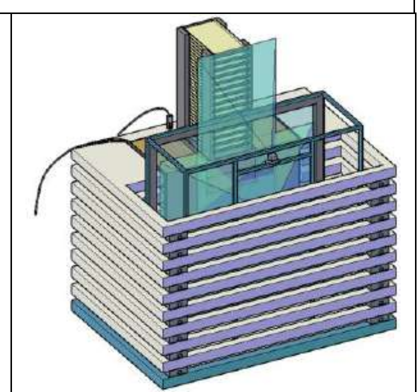

(e) Final scheme of tests

Figure 1-4: General assembly scheme

Several physical and technical aspects were considered for the experimental design. One of the main conditioning factors was the capacity of the shaking table in terms of acceleration and maximum frequency. Preliminary tests were intended to evaluate the operational range of the laminar container along with the maximum capacity of the shaking table, both harmonic and synthetic signals were tested. At the same time, several lighting tests were carried out, and the appropriate resolution for the images was defined. For the next stage, corresponding to the ***Paper I*** tests, the main purpose was to evaluate the different ranges of soil deformation in the laminar box. Thus, the selected inputs meet the requirement of mobilizing the shear strain of the soil. On the other hand, FEM numerical modeling of the interaction between the soil and the container walls was performed. The objective was to analyze the friction effects and their possible influence on the results.

Then, for the testing stage summarized in ***Paper II*** and ***Paper III***, different prototypes were defined according with the characteristics of actual buildings and retaining walls. For each of them, several case studies were defined. In the case of the building with underground stories, six configurations of both number of underground levels and floors were considered. In the case of retaining walls, the effects of burial height on the performance of the wall under dynamic loads were also considered. Once the study prototypes were defined, the type of scaling for the models was chosen. The most appropriate method was the one proposed by (Iai, 1989), which is also one of the most widely used in physical modeling (Biondi, Massimino, & Maugeri, 2015; Moghadam & Baziar, 2016; Tabatabaiefar, 2016; Turan et al., 2013; K.-L. Wang & Lin, 2011). To choose the scaling factor (λ), it must be verified that the geometrical similarity of the model does not exceed the size limits allowed in the laminar box. Both kinematic and dynamic similarities must be within the operating range of the shaking table, i.e., the natural frequency, in the case of the building, should not exceed the maximum frequency range of the table, unless a case of rigid body motion is evaluated. After having selected the most appropriate scaling factor, the construction materials are chosen according to the above-mentioned specifications, to finally perform the physical tests. This methodology is summarized in Figure 1-5 as a flow chart explaining the step by step of the physical modeling procedure.

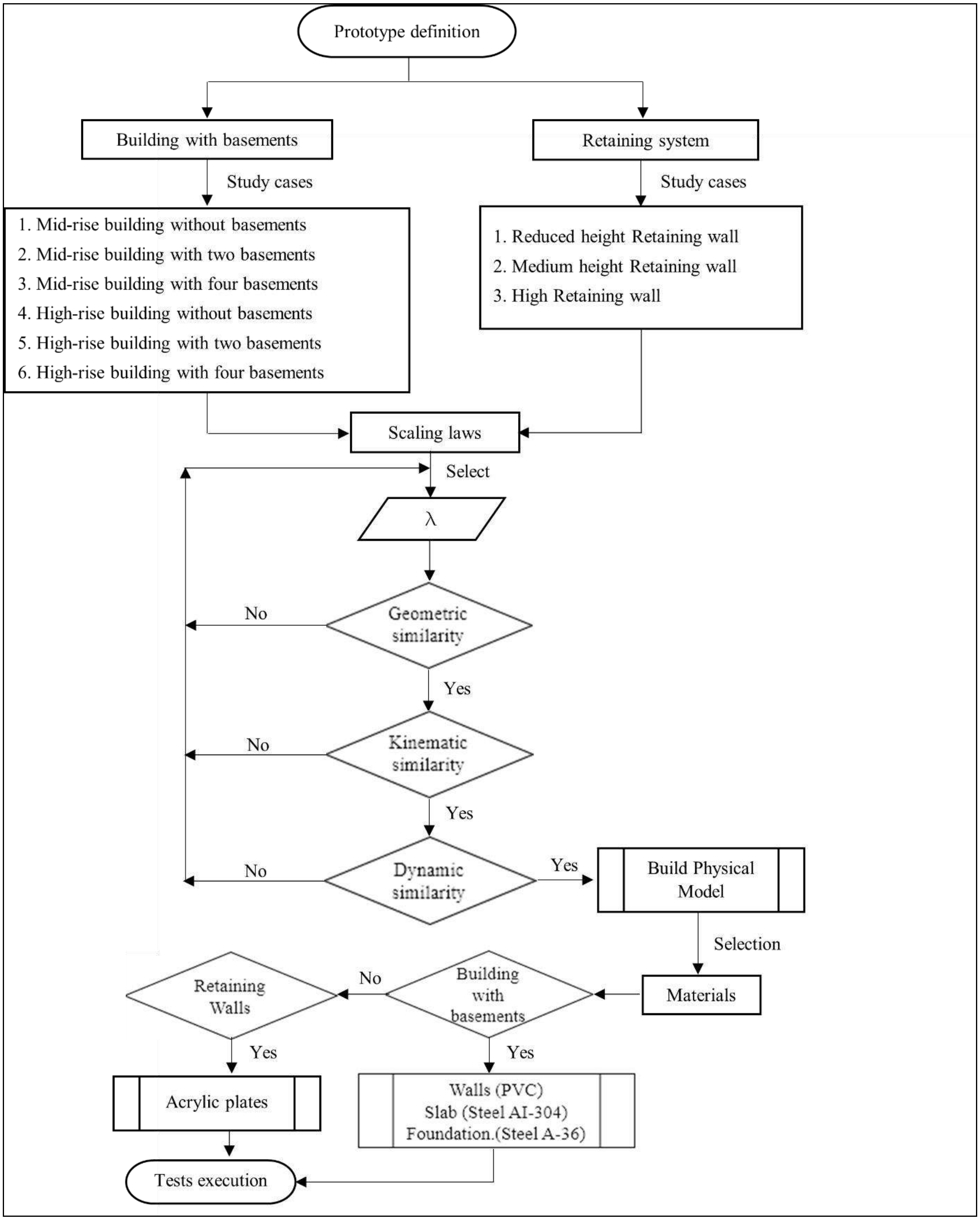

Figure 1-5: Flow chart of the experimental design

The total set of tests performed in this research are listed below in Table 1-1 together with their main objective:

Table 1-1: Set of tests

Stage	Test group	Purpose	Signal	Frequency range (Hz)	Amplitude (g)	Number of tests
Preliminary tests	1	Evaluation and calibration of laminar box	Harmonic	0.50	0.05 - 0.10 - 0.20	3
	2			1.00	0.05 - 0.10 - 0.20	3
	3			1.50	0.05 - 0.10 - 0.20	3
	4			2.00	0.05 - 0.10 - 0.20	3
	5			2.50	0.05 - 0.10 - 0.20	3
	6			3.00	0.05 - 0.10 - 0.20	3
	7			3.50	0.05 - 0.10 - 0.20	3
	8			4.00	0.05 - 0.10 - 0.20	3
	9			4.50	0.05 - 0.10 - 0.20	3
	10			5.00	0.05 - 0.10 - 0.20	3
	11		Ricker Wavelet	0.50	0.20 - 0.30 - 0.40	4
	12			1.00	0.20 - 0.30 - 0.40	4
	13			2.00	0.20 - 0.30 - 0.40	4
	14			3.00	0.20 - 0.30 - 0.40	4
	15			4.00	0.20 - 0.30 - 0.40	4
	16			5.0	0.20 - 0.30 - 0.40	4
	17			6.0	0.20 - 0.30 - 0.40	4
Paper I	1	Boundary effects	Harmonic	8.00	0.20	2
	2			12.00	0.10	2
	3	Nonlinear dynamic soil properties	Harmonic	5.00	0.30	2
	4			7.00	0.30	2
	5			8.00	0.30	2
	6			10.00	0.30	2
	7			10.00	0.20	2
	8			11.00	0.20	2
	9			12.00	0.20	2
	10			12.00	0.08	2
	11			13.00	0.08	2
	12			14.00	0.08	2
	13	Numerical simulation	Ricker Wavelet	3.00	0.60	2
	14		Harmonic	6.00	0.90	2
Paper II	1	SSI effects and dynamic pressure distribution on basements	Ricker Wavelet	2.30	0.65	1
	2			3.40	0.20	6
	3			5.00	0.20	6
	4			7.00	0.20	6
Paper III	1	Dynamic pressure distribution, active and passive wedge formation	Ricker Wavelet	5.40	0.27	3
	2			6.30	0.12	3
	3			5.40	0.38	3

1.6 Thesis Outline

All chapters of this Thesis are organized in such a way that they can be read independently of each other. Chapter 1 describes the organization of this document, presents a brief discussion of the activities, the main objectives, methodology and scope of this research. Chapters 2, 3 and 4 correspond to papers that have been published or are in the process of being reviewed. Finally, Chapter 5 summarizes the main conclusions of this research and recommendations for future investigations are provided.

Chapter 2 corresponding to ***Paper I*** “Continuous characterization of dynamic soil behavior by Digital Image Correlation in a transparent shear laminar box”, describes the non-linear behavior of a dry granular soil by means of a laminar box container developed for this research, which main characteristic is the frontal transparency allowing the full monitoring through a high-speed and high-resolution camera. Results from DIC and accelerometers analysis, showed a good agreement in terms of particle movement. Furthermore, the analysis of the particles movement in the physical model compared well with the results from cyclic torsional and resonant column tests. Additionally, DIC analysis showed a minimum observable shear strain of about 10^{-4}. Thus, the transparent container provides a remarkable opportunity to develop more sophisticated tests in the field of DSSI.

Chapter 3 corresponding to ***Paper II*** “Evaluation of Dynamic Soil-Structure Interaction effects in buildings with underground stories using 1-g physical experimentation in a transparent shear laminar box”, describes the behavior of different physical scaled models subjected to Ricker wavelets. The experimental phase included a new configuration of the laminar container used in Chapter 2 by including an array of three cameras for better visualization. Moreover, to correlate the dynamic induced pressures and non-linear soil behavior, a tactile sensor was incorporated in the underground walls, this analysis combined with DIC technique allowed a detailed description of the dynamic interaction between the building and the soil. The results showed that the lateral thrust is mainly influenced by the superstructure vibration. In addition, higher depths of confinement showed a reduction in the effective input motion. Therefore, neglecting DSSI effects in the analysis of buried studied structures provides a conservative design. This chapter has been submitted to Engineering Structures journal last December and comments have already been received. The comments are simple, and the revised version is being prepared.

Chapter 4 corresponding to ***Paper III*** "Dynamic pressures and soil displacement assessment in rigid partially embedded cantilever retaining walls using a transparent laminar box", describes the dynamic earth pressure distribution on retaining systems through a tactile sensor. Besides, the measurements are correlated with the non-linear behavior of the soil from the Digital Image Correlation technique and against a finite element model of each tested configuration. It was shown that the pressure tends to decrease during a dynamic event from static thrust which correlates well to backfill displacement field. It was also found that the vertical location of the resultant force tends to increase its value as the wall rotates with respect to its base. This chapter has been recently submitted to Acta Geotechnica journal.

1.7 Practical aspects, experiences and recommendations for future research with the transparent laminar box

The design and construction of the laminar box was, undoubtedly, a laborious and exhaustive task. Its implementation in this research presented unforeseen challenges that required ingenious solutions. This section summarizes the most relevant practical aspects that are not included in the description of experiments in the papers and may be useful to future users of the device.

The soil to be used is one of the most important elements for the development of tests, the sand must be clean and dry, the color contrast must be sufficiently visible for the correct functioning of the digital image correlation technique. Otherwise, for example in the case of soils with very fine particles that do not allow its differentiation, its composition must be altered by adding color components such as white lime.

The soil used for this investigation satisfied all the necessary characteristics described above, after sieving about 2 tons of sand to reach an optimal particle size distribution. However, silty-clay particles are difficult to separate from the sand, so that when the soil is placed into the container by dry pluviation, the dust impregnated the glass, preventing a correct visualization. Therefore, all the sand used in this investigation was washed and oven-dried, removing the fines portion. While the sand meets the color contrast condition, the models of the structures were prepared with a random pattern of colors to generate a high color contrast on their front side (Figure 1-6).

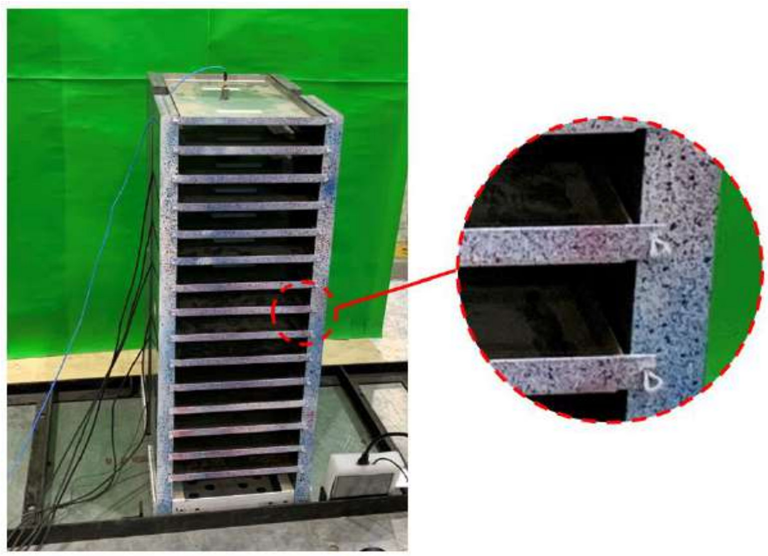

Figure 1-6: Preparation of physical model of structures for DIC tests

On the other hand, the transparency characteristic of the laminar box requires more preparation compared to traditional laminar containers. The area of sand to be visualized in the front side should be naturally delimited by the edges of the rings. These in turn are in contact with the front glass and an aluminum plate at the back. These boundaries must be sealed with a round rubber with an adequate thickness which does not introduce friction to the ring system (Figure 1-7), since the slightest variation in the thickness of this element would allow a sand leakage, or increase in ring-wall friction, that would affect the results of the experiment.

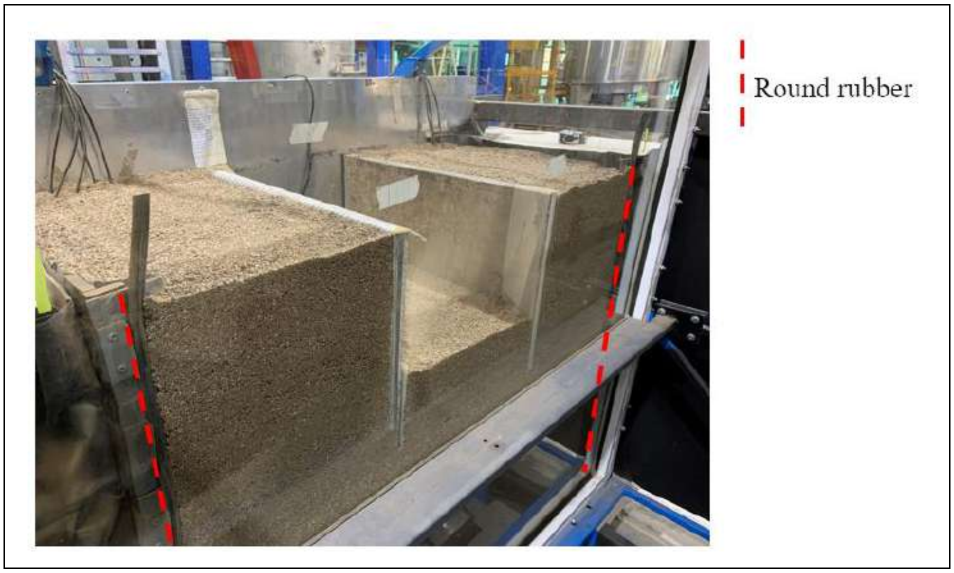

Figure 1-7: Rubber sealing system

The experiments of this research are classified as destructive and non-destructive tests. Those in which the experiments can be performed one after the other without the need to repeat the preparation procedure, are considered non-destructive, this is the case of the tests developed in ***Paper I*** and ***II***, where the soil does not present permanent deformations or residual rearrangement of particles. While destructive tests are referred to those in which each test requires a new model preparation after finishing the previous one. This type of tests is developed in ***Paper III*** where, in addition to large deformations, they were permanent, which requires a new installation of the sensors. Therefore, according to the type of test, non-destructive or destructive, the most suitable method of sand density control in the laminar box was chosen. For the first case (i.e., non-destructive), a vibration compaction method was used, consisting of a series of harmonical signals for each filling stage until no settlement is recorded. Once the last layer of soil was reached, the density distribution was verified by means of a nuclear density gauge. On the contrary, the density of sand for destructive tests is controlled by the dry pluviation method. This procedure ensures a homogeneous distribution of the density throughout the laminar box as the sand is placed in the container and does not require any prior vibration. Different heights of fall were tested in a mold of known volume to obtain a target density (Figure 1-8).

Additionally, a perforated aluminum plate with different sizes of openings was made to study its effect on the final density (Figure 1-9).

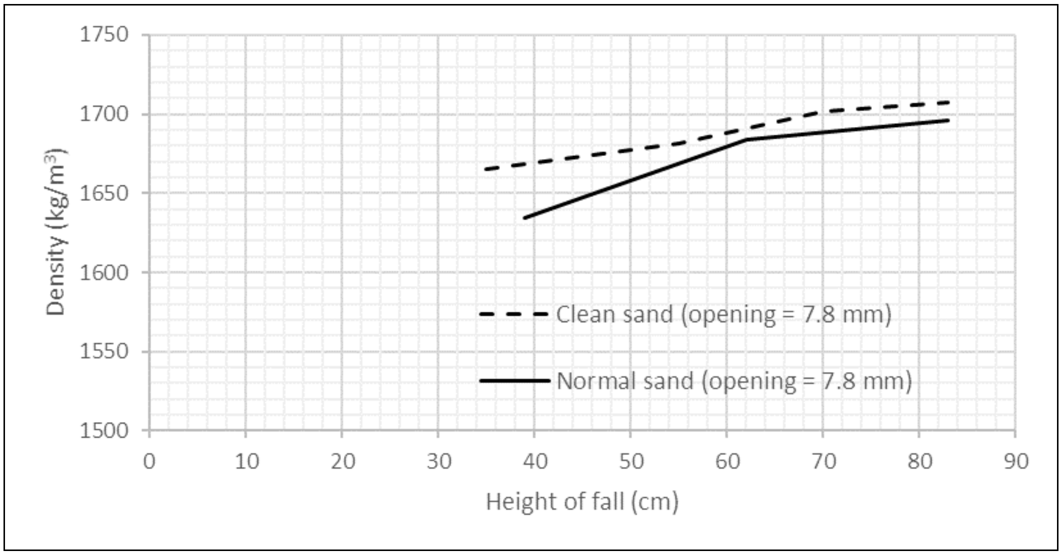

Figure 1-8: Density analysis by the Dry pluviation method

Figure 1-9: Scheme of Dry pluviation method

Once the sand is clean and properly placed into the container, the next step is to adjust the light intensity by means of spotlights distributed equidistantly. Four spotlights equivalent to 6400 lumens each were needed to eliminate any shadows. However, these must be in such a way that their reflection in the glass is not observed in the image, at least the portion that will be photographed must be free of any reflection (Figure 1-10). Since the internal space where the cameras and spotlights are installed is relatively small, it should be covered by a dark cardboard (Figure 1-11) to insulate the lighting.

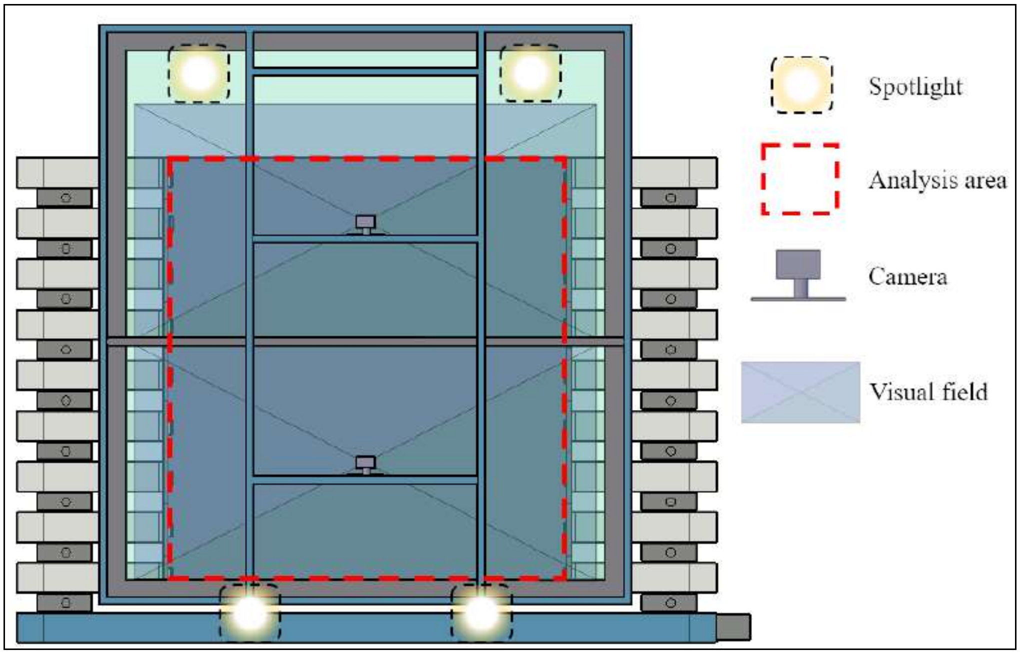

Figure 1-10: Diagram of spotlights distribution

Figure 1-11: Installation of the dark cardboard

Even though the sand is completely clean and dry, it is necessary to protect the measurement sensors before they are buried (Figure 1-12), this task can be done by simply covering the devices (i.e., accelerometers and pressure sensor) with masking tape or transparent bags, and it should be verified that they are entirely sealed since very small particles could damage their operation.

Figure 1-12: Buried sensors

The placement of some physical models on the shaking table, especially the heavier ones, required the use of a crane for installation (Figure 1-13).

Figure 1-13: Placement of the physical model using a crane

Another important aspect to consider is referred to the shaking table, since the theoretical signals, depending on the frequency range, are difficult to replicate accurately. However, in most cases, as long as the acceleration amplitude and frequency range do not exceed the limits allowed by the shaking table, tests can be performed with very reasonable accuracy (Figure 1-14). Otherwise, inputs must be previously executed to calibrate the signal to be replicated. Although the table is currently being upgraded with a more sophisticated and powerful actuator, for future tests the previous calibration of signals should be relatively simple. In any case, it is recommended to verify the theoretical signals by means of an accelerometer installed at the base of the shaking table and correct the input if necessary. Since the input analyzed in the experiment will be the one recorded in the shaking table base and not the theoretical one.

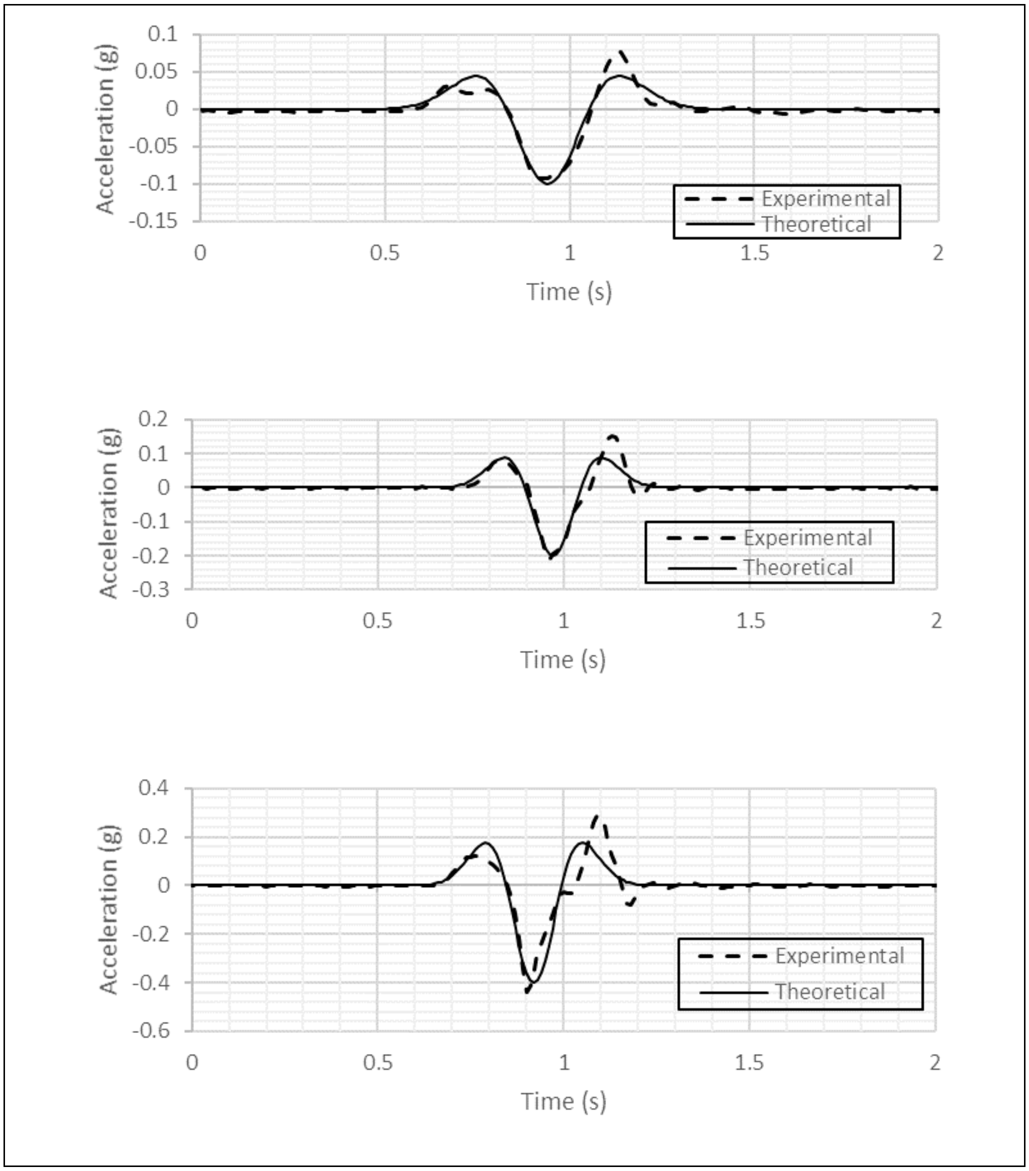

Figure 1-14: Comparison of theoretical and experimental signals

Finally, this research was also characterized by grouping different types of data acquisition systems, including accelerometers, displacement transducers (LVDT), high-speed cameras and pressure sensors. To perform a correct analysis of results, all devices must be perfectly synchronized in the sampling. Initially, an attempt was made to perform this synchronization by means of an automation process. However, there were still time lags of about 0.01 seconds in the acquisition. Therefore, a procedure was designed to achieve the required synchronization. The digital chronometer of the acquisition software for accelerometers and LVDT is considered as the main timer, therefore this is projected in a mini display which is placed in the front part of the laminar box, allowing its visualization with one of the main cameras ensuring that the reference time is photographed. At the same time, the handle that is responsible for starting the pressure sampling will indicate the start of the acquisition by means of a light marker that will also be photographed with the main camera. As a result, all acquired data are synchronized.

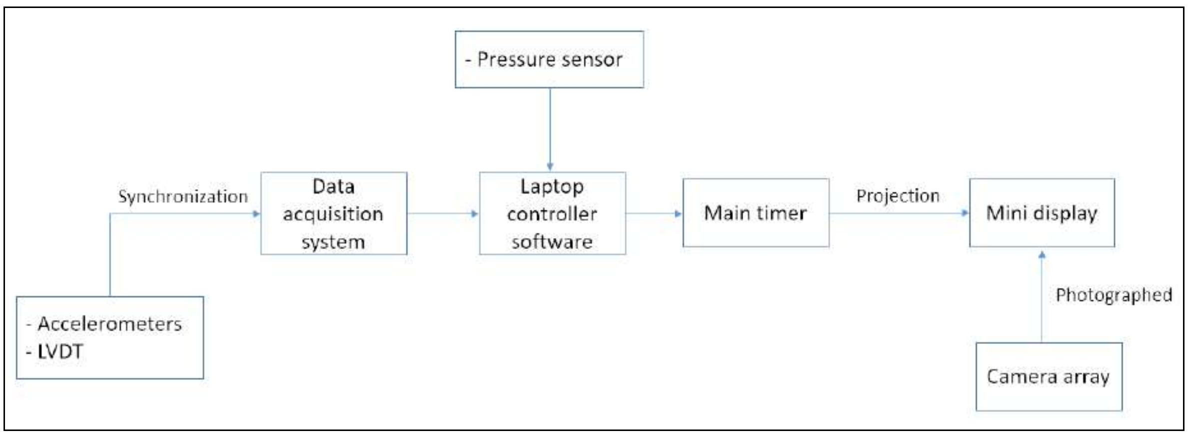

Figure 1-15: Diagram of synchronization

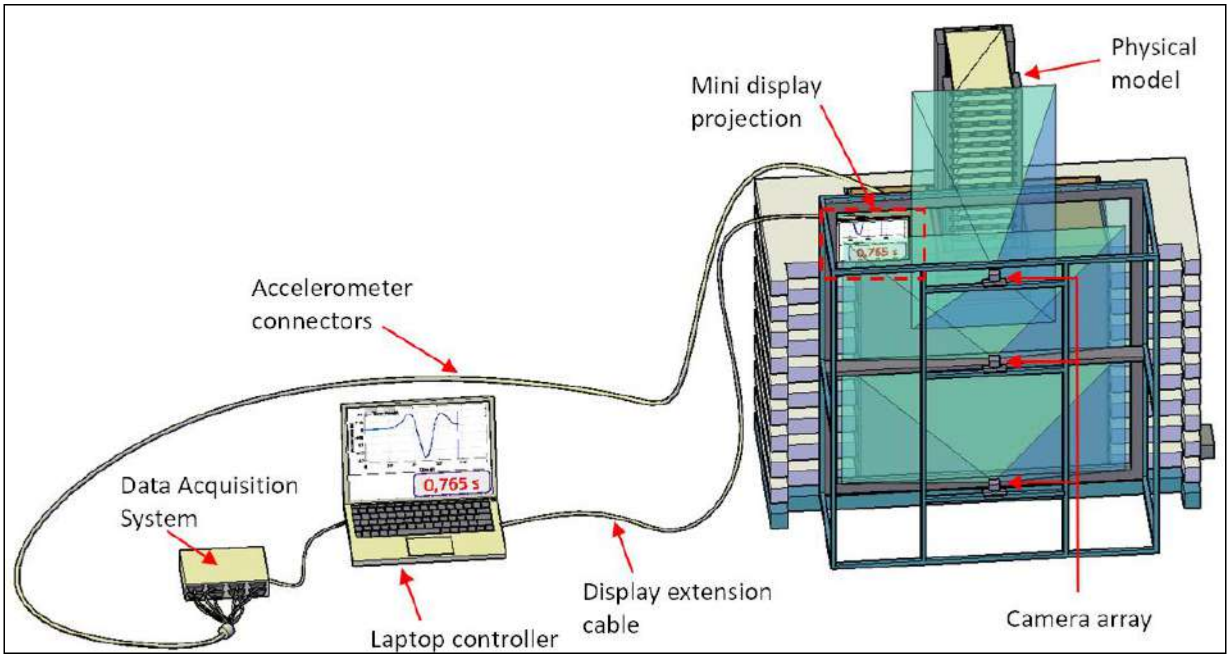

Figure 1-16: Scheme of synchronization

2. CONTINUOUS CHARACTERIZATION OF DYNAMIC SOIL BEHAVIOR BY DIGITAL IMAGE CORRELATION IN A TRANSPARENT SHEAR LAMINAR BOX

2.1 Introduction

The measurement of dynamic soil properties is an important issue in geotechnics, since they have a fundamental role in the understanding of Earthquake Geotechnical Engineering. With this purpose, extensive numerical and experimental research studies have been carried out during the last years. Both types of analyses have certain advantages and limitations. On the one hand, numerical models have a high degree of complexity in their formulation and require a series of parameters that may be difficult to calibrate or validate. On the other hand, physical models performed either at 1-g or *n*-g, if done properly, can replicate real prototype conditions in a controlled environment. Results from experimental models performed at 1-g must be treated carefully because of their low level of confinement.

In the literature, experimental soil response measurements are generally restricted to a few discrete points, associated with the location of a limited number of sensors (e.g., accelerometers, displacement transducers). Hence, the capability to obtain information through a continuous field becomes a useful advancement. In the following sections, a methodology to measure the continuous soil response under dynamic loading is presented.

A series of tests to validate the use of the 1-D transparent laminar box under dynamic shaking are presented, allowing us to evaluate the main dynamic properties of the soil and its nonlinear response. Boundary effects are evaluated to verify lateral flexibility of the container, while the field displacement of the soil is analyzed by Digital Image Correlation (DIC) technique. In order to perform this analysis, a model was built using dry sandy soil, with the main feature of a clear contrast of colors between particles.

Afterwards, dynamic soil properties are compared, i.e., shear modulus and damping ratio, evaluated from cyclic tests in the shaking table and dynamic/cyclic standard laboratory tests. Then, ambient vibration analysis is conducted to evaluate the fundamental frequency of the system. Finally, the experiment is modeled using the finite element method to evaluate the influence of friction on the glass face of the soil container.

2.2 Soil Dynamic physical modeling at 1-g

Measuring and understanding the soil behavior are key factors in geotechnical engineering, so different laboratory test devices have been developed to study the response of soil under near realistic conditions. In this sense, a laminar container meets the requirements for replicating free field boundary conditions and it has proven to be a useful tool for earthquake engineering research in seismic wave propagation, liquefaction and soil-structure interaction. However, one limitation is the uncertainty of the deformation profile of the soil, due to the impossibility of having a lateral visual field of the sample. Thus, the information obtained is restricted to discrete points, where an accelerometer or pore pressure transducer is placed. In this sense, the analysis of the visual field has gained importance in geotechnical models, being widely explored with different techniques (i.e., Particle Image Velocimetry or PIV, and DIC). In the following sections, a brief literature overview of these procedures is presented.

2.2.1 Laminar shear box

Physical models, in 1-g or *n*-g conditions, are still a fundamental tool for research, due to the limitations that numerical methods have when attempting to reproduce complex problems in Earthquake Geotechnical Engineering. First insights of rigorous physical modeling were introduced in the 1950s. The main idea was to replicate real conditions of a prototype in a reduced-scale model, where similarity rules must be satisfied. Langhaar (1951) identifies three main factors to be respected in a scaled model, i.e., geometric, kinematic and dynamic similitude. This work led to the first steps of physical models in different fields of engineering. Rocha (1958) was one of the first authors to investigate geotechnical physical models and analyze similitude laws able to relate physical dimensions, stress and strain of the prototype with a model at different scales. This first qualitative insight has been discussed by many authors throughout the years and the methodology has been highly improved. Among the most important works are Roscoe (1968) who pointed out that it is not necessary to replicate all physical quantities, but rather the most significant parameters, in order to satisfy the principles of similitude. Iai (1989) developed a compilatory work about the theory of scaling models and their application to soil-structure-fluid interaction problems by deriving similitude laws. Two main restrictions for the applicability of the similitude laws are emphasized: (a) loss of contact in soil particles is not allowed, and (b) only small strains are permitted so that linear equations can be used.

Particularly, when modeling dynamic soil behavior, boundary conditions have an important role in soil response, due to the limitations of performing this kind of test in a reduced space in comparison with real conditions (i.e., lateral free field and half-space media). In this way, laminar containers are designed to simulate lateral boundaries of soil when subjected to seismic waves (e.g., Jafarzadeh et al., 2008; Meymand, 1998; Moss et al., 2011; Dihoru et al., 2016; Tabatabaiefar, 2016; Turan et al., 2009), since the walls are flexible and have the capacity to follow the soil movement and avoid wave reflections as a rigid wall would. Alternatively, Lombardi et al. (2015) explored the use of a rigid container with absorbing boundaries.

Most recent advances allow the evaluation of dynamic soil behavior and the study of specific problems in earthquake geotechnical engineering. Dietz and Muir Wood (2007) studied the dynamic soil properties by applying three different excitation forms, i.e., random, pulse and sinusoidal. Chau et al. (2009) provide a solution for nonlinear soil-pile-structure interaction by comparing experimental and Finite Element Method (FEM) analysis. Turan et al. (2013) investigated the effects of soil-structure interaction (SSI) in buildings with embedded stories. They used a laminar container, consisting of several layers supported by an external frame, to avoid additional mass in the shaking table.

Tsai et al. (2016) investigated how boundary effects can affect the determination of dynamic parameters of the soil in a two-layer container. In some cases, a centrifugal test is used to replicate gravitational stress of soil (Brennan, Thusyanthan, & Madabhushi, 2005; Elgamal, Yang, Lai, Kutter, & Wilson, 2005; Ulgen, Saglam, & Ozkan, 2015; Zeghal, Elgamal, Zeng, & Arulmoli, 1999). Nevertheless, those tests are sophisticated, centrifuge equipment is expensive, and the models require a significant amount of time to be developed.

2.2.2 DIC and PIV in geotechnics

In recent years, digital image processing for strain analyses has been implemented as an alternative to measure physical phenomena; the first insights were carried out into the field of fluid mechanics with the PIV technique, which consists of tracking different markers seeded in the flow, and therefore velocity vectors can be determined (Adrian, 1991). The application of this technique in soil deformation measurement did not take long to be developed. White et al. (2001; 2003) improved this method significantly by establishing a combination of digital photography, the PIV technique and close-range photogrammetry. However, this combination has not been utilized under dynamic conditions. Cilingir and Madabhushi (2010) focused on the acquisition of images using a high-speed camera. They analyzed the soil deformation around four different types of tunnels in centrifuge tests; although the resolution of images strongly affects the quality of the results, the reflection of lighting due to the tight space represents an important issue in this kind of experiment, even if the visual field is relatively small (200mm x 200mm). However, more recent investigations have improved the algorithm analysis through new numerical implementations (Stanier, Blaber, Take, & White, 2016) or the acquisition of data from synchronized cameras (Teng, Stanier, & Gourvenec, 2017).

Digital image correlation technique consists in determining the deformation by comparing the changes in the image of the surface of a tested object before and after loading. This method has been widely developed to quantify and analyze the strain field of materials, whether they are subjected to external forces or a known displacement pattern (Murray, Hoult, & Take, 2017). More precisely, some geotechnical tests in sands, such as triaxial tests (Hall, Bornert, et al., 2010) or strain increments in two dimensions (Hall, Wood, Ibraim, & Viggiani, 2010), have been obtained by using this technique. Additionally, in literature, a combination of both methods (PIV and DIC) is studied in problems of fluid-structure interaction (P. Zhang, Peterson, & Porfiri, 2019) and failure mechanisms of slopes (Kapogianni, Tsafou, & Sakellariou, 2019).

According to literature review, there is no previous research that has attempted to combine the advantages of DIC with dynamic geotechnical tests in 1-g laminar boxes. Probably the main reason is that the usual laminar shear boxes are made of steel or aluminum, preventing the direct lateral visualization of the soil inside the box during the test. The purpose of this research was to develop a transparent laminar box allowing direct visualization of the soil during the cyclic loading. The idea was to apply DIC technique to characterize the continuous dynamic behavior of the soil through the photographed portion of soil. This article describes the equipment, the study that was carried out to assess the boundary effects and the dynamic results obtained through DIC. The results were compared against direct measurements, laboratory results and simple nonlinear behavior models to show the agreement between the different data sets.

2.3 Methodology

2.3.1 Laminar box description

The laminar shear box, shown in Figure 2-1, is capable of propagating seismic waves in a single axis and was designed to study physical models in a 1-g environment. One of the main characteristics is a transparent glass on the front side, making it possible to observe and compute the strain field through DIC analyses. To take pictures of the complete glass side using a standard camera of 22 mm of focal length, a minimum distance of 1m from the glass is required. This requirement significantly enlarges the dimensions of the laminar box, and it makes the operation of the device somewhat difficult. Additionally, it introduces an unbalanced weight, displacing the center of mass horizontally from the soil. To reduce this distance by about 55 cm, a mirror was incorporated at one side of the filming area.

This laminar container is composed of nine fiberglass rings whose individual weight is 10.4 kg, with total dimensions of 960 mm in height, 1000 mm long and 500 mm wide; these frames are connected to each other through four single-row ball bearings to reduce the friction between rings, and designed to reach a maximum shear strain of about 15%. To prevent soil leakage, a reinforced polyester bellows membrane covers the deformable sides of the soil container. In this way, lateral flexibility is guaranteed. Because the weight of soil contained is about eight times more than the fiberglass laminar box, inertial effects are expected to be negligible.

The backside is covered by aluminum, and the front side is composed by tempered glass with a thickness of 8 mm; additionally, a rubber round (like a wiper) is placed between the front glass and the perimeter of the soil container. The aluminum wall and tempered glass are fixed, and the rings can move laterally due to a low-friction contact with these lateral walls. According to literature, the value of the friction coefficient between the soil and solid surfaces, such as glass, is around 0.12 (Tatsuoka & Haibara, 1985), nevertheless, this value can only be considered as a general reference since friction strongly depends on factors such as surface roughness, material, humidity, particle size distribution and shape that vary case to case. The tempered glass and mirror, along with the camera, are mounted in a fixed frame, independent of the stack of rings, as shown in Figure 2-1.

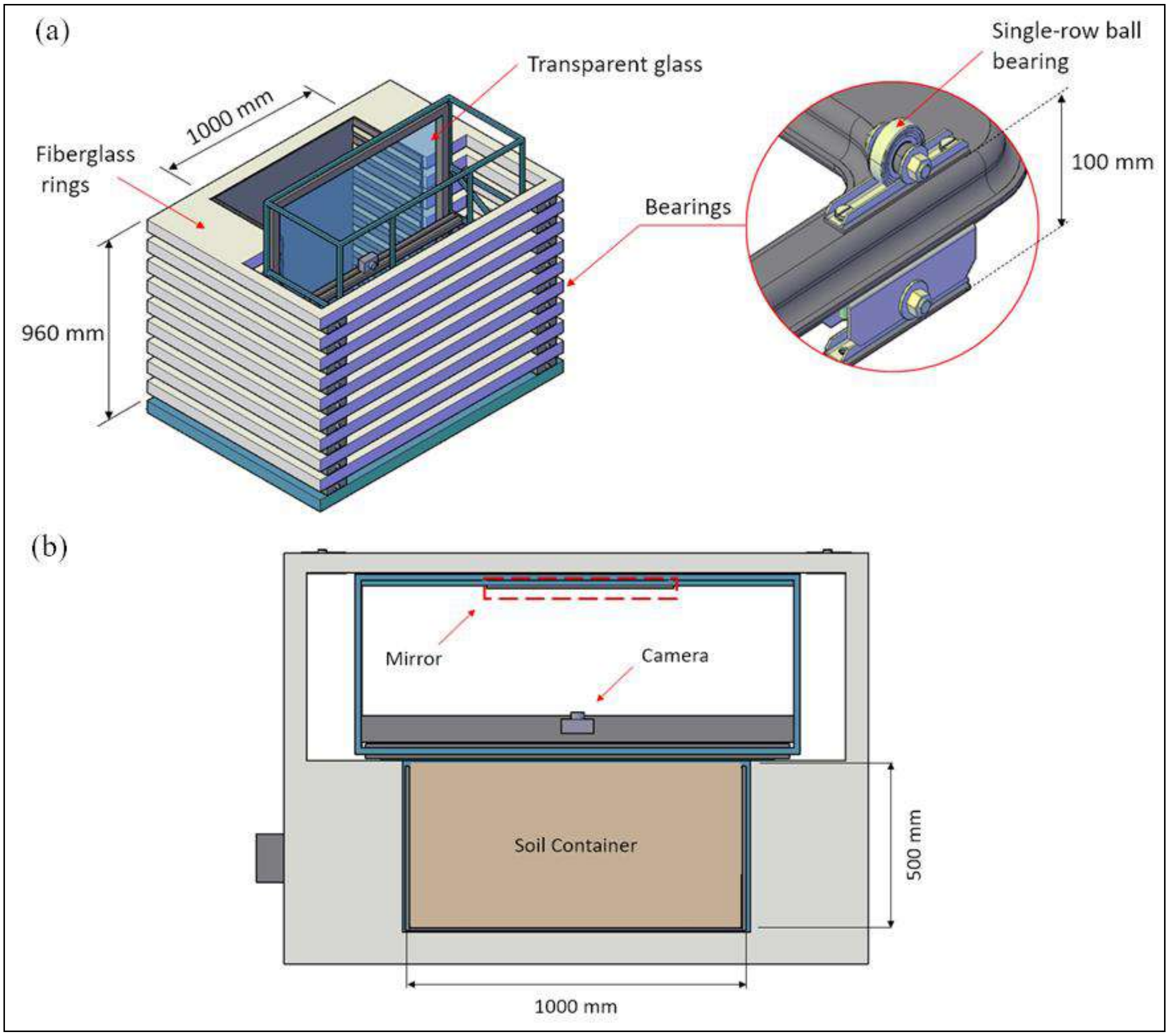

Figure 2-1: Shear laminar box: (a) Isometric view, (b) Plan view.

2.3.2 Shaking table tests

The servo-hydraulic shaking table designed by ANCO Engineers Inc. (ANCO) has one degree of freedom (1-DOF); its major features include a maximum acceleration of 1.0 g and lateral displacement of ± 450 mm with an allowable payload of 2000 kg approximately (Figure 2-2).

The first stage of this research was to evaluate boundary effects in the laminar box, whereas the second part is intended to identify the nonlinear dynamic properties of the soil. Thus, once the optimal operating range was determined in the shaking table, an experimental program was developed to study both aspects, including different signal amplitudes in a wide frequency range (Table 2-1). The experimental program was not developed to reproduce any prototype, but rather to explore the performance of the laminar box and assess the ability of DIC to infer the dynamic properties of the contained soil.

Figure 2-2: Shaking table (ANCO) and the laminar box

Table 2-1: Summary of tests in shaking table.

Test Group	Purpose	Signal	Input amplitude (g)	Frequency (Hz)
1	Boundary effects	Harmonic	0.2	8
2			0.1	12
3	Nonlinear dynamic soil properties	Harmonic	0.3	5;7;8;10
4			0.2	10;11;12
5			0.08	12;13;14
6	Numerical simulation	Ricker wavelet	0.6	3
7		Harmonic	0.9	6

2.3.3 Data acquisition and instrumentation

A total of eight accelerometers (ACC 1 - ACC 8) were located inside the container to measure the response of the soil at different depths (Figure 2-3) and to study possible boundary effects by comparing the Fourier Amplitude Spectra (FAS) of accelerations measured at the middle of the container and close to the rings. Additionally, one accelerometer (Acc Base) and one displacement transducer (LVDT) were placed at the base of the shaking table.

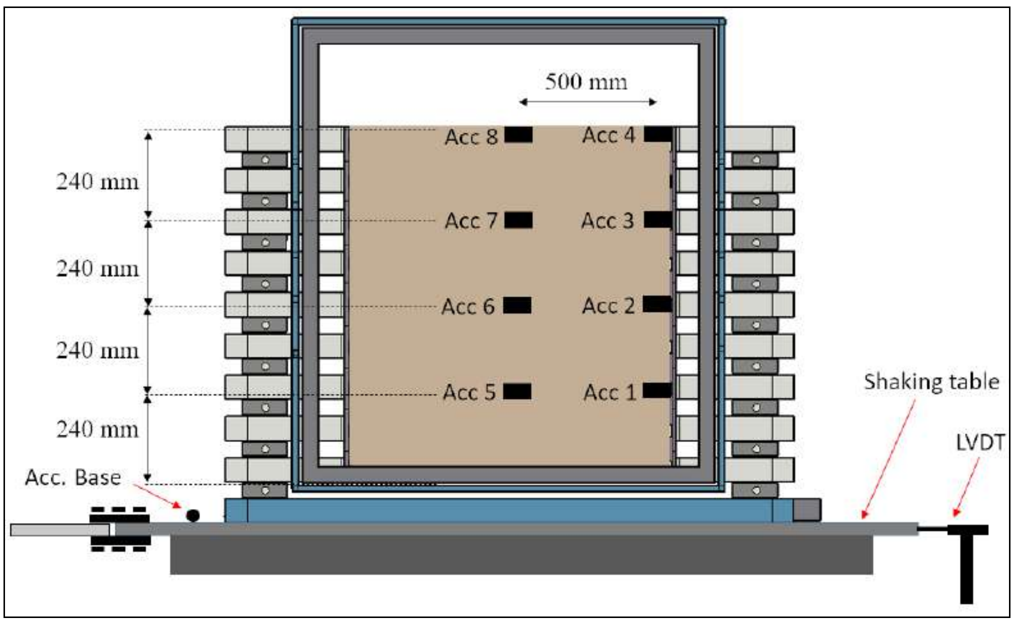

Figure 2-3: Instrumentation in the laminar box and the shaking table

2.3.4 Image collection and analysis

In the case of dynamic tests, a reasonable number of frames per second (fps) are required in order to take the maximum information during the test and to properly characterize the higher frequency content of the experiment. In this research, all tests were monitored at 60 fps. The resolution of each frame is relevant to obtain an accurate soil deformation tracking. After several trials, a resolution of 4.1 Megapixels was identified as satisfactory for this purpose, since the motion of the particles was computed adequately from images.

Post-process results were obtained from the Match ID® software (Lava & Debruyne, 2010). This software uses an iterative approach based on a two-step process. Firstly, an initial coarse correlation is done assuming pure translation of the subset. This initial estimation is iteratively improved following a forward additive Gauss-Newton method (FA-GN). Regarding the correlation criteria, we used a Normalized Sum of Squared Differences (ANSSD), which approximates the Hessian (i.e., the second-order derivatives of the correlation criterion) by a multiplication of the Jacobians. Global bicubic splines were used as interpolation scheme for the intra subset, while affine second-order shape functions allowing to subset to shear, rotate and translate were considered. After evaluating various combinations, little better results were obtained using a subset size of 21 pixels and a step-size of 10 pixels.

2.3.5 Preparation and soil placement

In order to have a first insight of laminar box performance and to guarantee the proper functioning of DIC technique, a dry sandy soil characterized by a high color contrast between particles was selected. This material was placed in the flexible container in ten layers, each one with a specific weight and volume; then, a series of loading cycles were carried out to induce compaction by vibration to avoid the occurrence of significant settlements during the tests. The final density inside the container was verified using a nuclear density gauge as 1.62 gr/cm^3, which corresponds to 70% of the relative density. Figure 2-4a illustrates the location of the transparent soil container inside of the laminar box.

According to the Unified Soil Classification System (USCS), the soil is categorized as poorly graded sand without fines (SP) (see Figure 2-4b). The dynamic properties obtained by a combined Resonant Column/cyclic Torsional Shear device (RC/TS), conducted at a confining pressure of 50 kPa, were compared against reference values for sands (Harry Bolton Seed, 1970). Experimental results of shear modulus and damping ratio are in good agreement with the standard curves for cohesionless soils. However, there is a variability in the damping for strains larger than 0.1% (Figure 2-5).

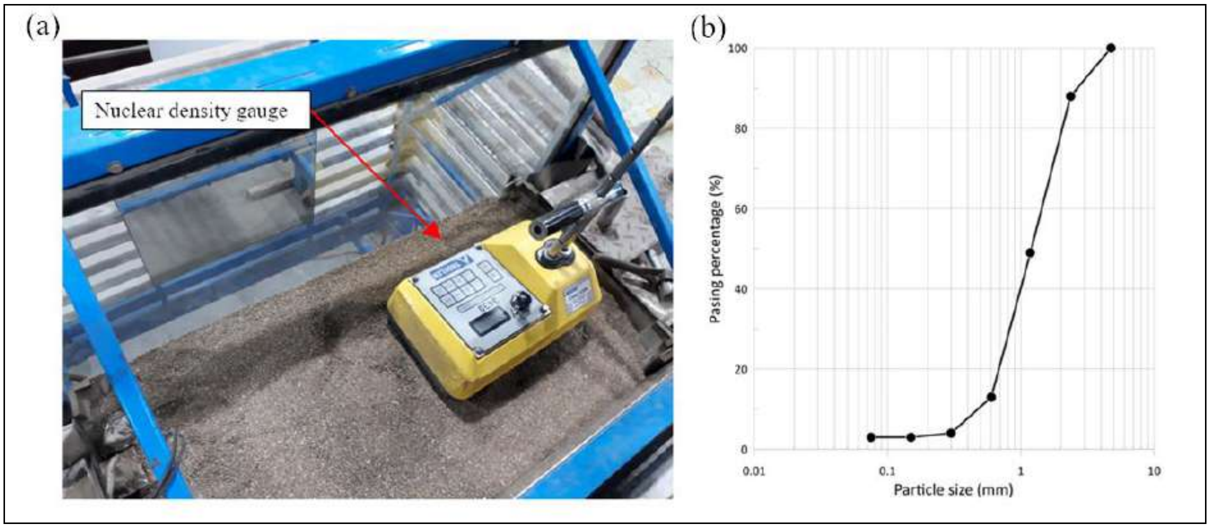

Figure 2-4: (a) Nuclear density gauge located on the surface; (b) Distribution of particle size

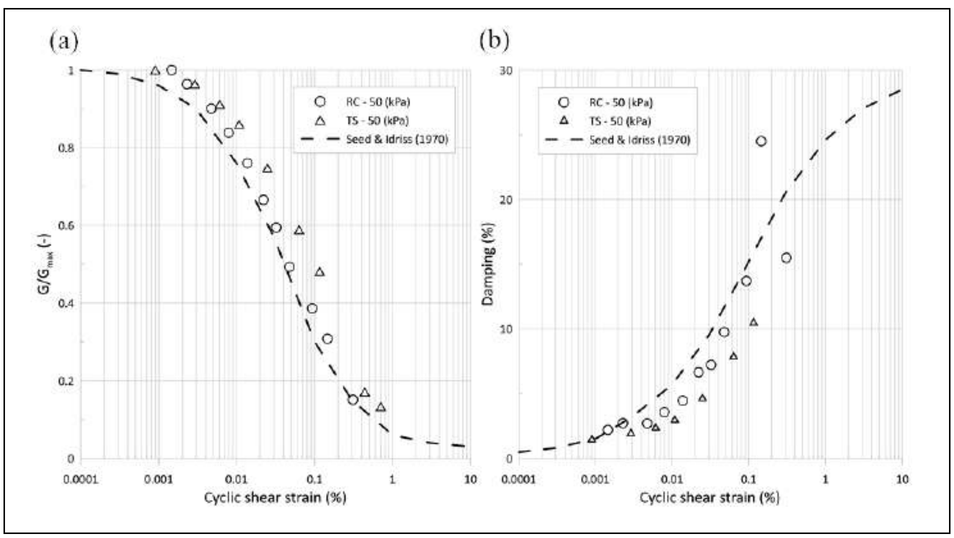

Figure 2-5: (a) Experimental Stiffness degradation, (b) Experimental Damping curve

2.3.6 Static lateral friction and dynamic friction with the glass

The static and dynamic behavior of the laminar box was studied with the objective to identify any drawback associated with the side window. Two aspects were analyzed: the friction of the rings and the friction of model with the glass of the window.

The friction of each ring has three components: the friction in the contact with the rings above and below in the stack, and the other is the friction of the ring with the fixed glass of the window, where a sliding rubber seal was implemented, to prevent sand particles to enter in this area. The test consisted in laterally fixing all the rings but the ring to be tested, and the force required to move the ring was measured, with the box empty. This force corresponds to the frictional resistance from the contact with the ring above and below, plus the friction of the contact of the ring with the window. The test was repeated for all the 9 rings (see Figure 2-6), and the average friction coefficient obtained is 0.02, which can be associated with a frictional angle of 1.0 degrees. In this figure, we removed the outlier value obtained for the ring 3.

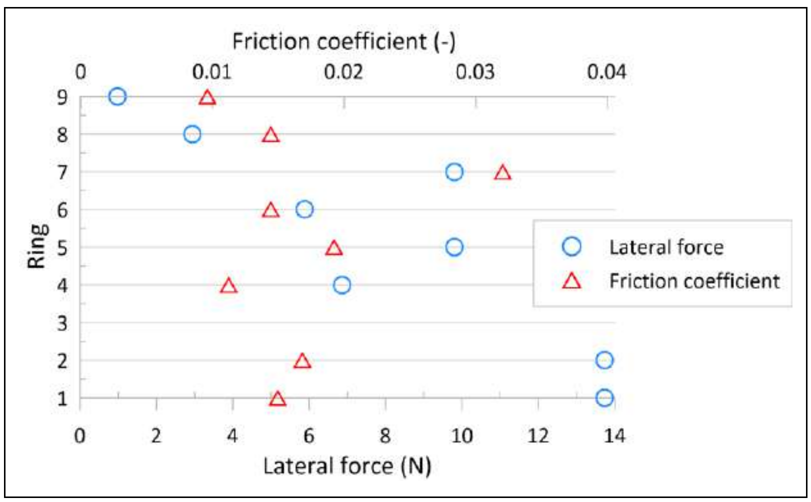

Figure 2-6: Lateral force measured in each ring

Usually, in the literature this friction is reported as a friction between two rings, but we were not able to decouple the three components of the friction measured (ring above, ring below, and window). However, we consider that the friction measured is very low, and comparable with the friction of other small laminar boxes reported in the literature (Ecemis, 2013; Hushmand, Scott, & Crouse, 1988; B. Jafarzadeh, 2004; Suzuki, Babasaki, & Suzuki, 1991; Turan et al., 2009).

The other aspect is the friction of model with the glass of the window. The glass of the laminar box is fixed, and the soil particles in the model move during the experiments, generating some friction with the glass. With the objective to evaluate the magnitude of this friction, the measurements from two accelerometers located at 340 mm from the soil surface are analyzed: one at the center of the soil and the other at the same height and distance from the longitudinal boundaries, but next to the glass. The Figure 2-7 below shows the comparison of measurements from both sensors, during a Ricker Wavelet excitation with a maximum acceleration of 0.26g.

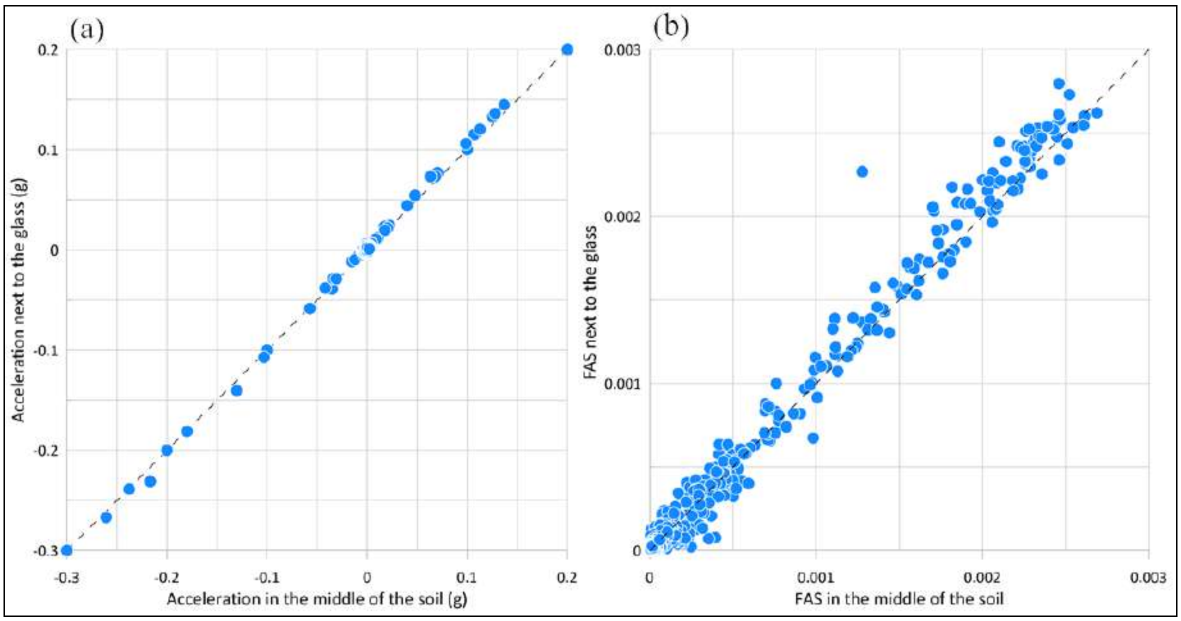

Figure 2-7: Comparison of measurements at the center of the soil against measurements next to the glass.

The Figure 2-7a presents the acceleration measurements at the center of the soil against the measurements next to the glass. The datapoints are aligned around a 45 degrees line, showing that both sensors record nearly the same acceleration at the same time during the test. Furthermore, the Figure 2-7b shows the Fourier Amplitude Spectrum (FAS), obtained from the acceleration records of both sensors, and plotted against each other. The data also aligns around a 45 degrees line, meaning that the Fourier amplitudes are very similar at the same frequencies.

Based on this analysis, we consider that there is not significant disadvantage in the laminar box behavior, due to the implementation of the side window. Additionally, in Section 4.5, we present a computational model developed to numerically study the friction between the front side of the soil and the glass, to quantify the influence of this boundary on the results obtained from DIC analysis.

2.4 Results

2.4.1 Boundary effects

Several amplitudes and frequencies were studied to analyze boundary effects; as an example, Figure 2-8a-b show the acceleration generated by harmonic signals at 8 Hz and 12 Hz of frequency and 0.2 g and 0.1 g of amplitude at the base, respectively. The input amplitude was gradually increased using a tapering function, i.e., these figures show a window of quasi-stationary motion. A comparison between accelerometers at the same depth, in the center and near the rings of the laminar box, shows a very similar motion, suggesting that these boundary effects are negligible.

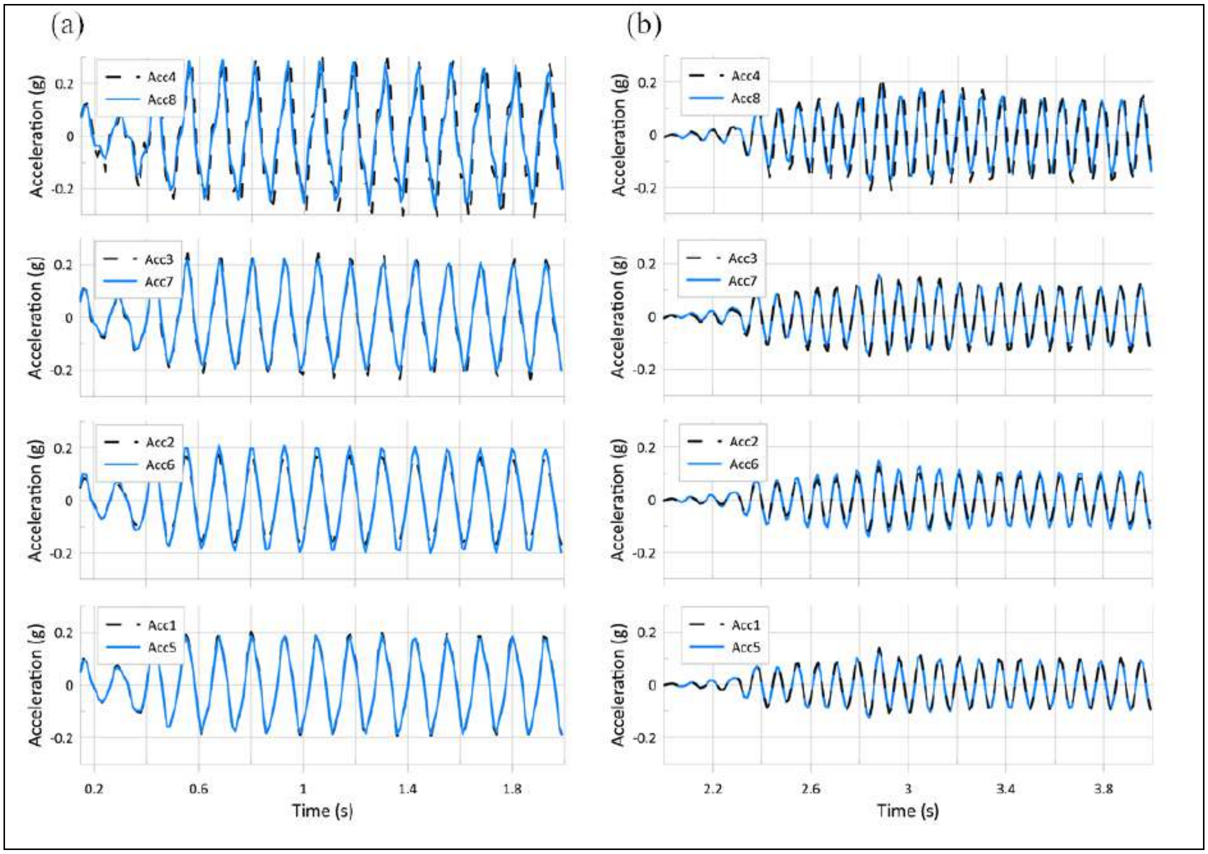

Figure 2-8: Evaluation of boundary effects: (a) Harmonic motion of 8 Hz and A=0.2 g; (b) Harmonic motion of 12 Hz and A=0.1 g.

2.4.2 Assessment of low-strain dynamic properties of the soil in the box

Based on resonant column tests (RC), a model of the shear-wave velocity dependency on the confinement pressure of the following form was calibrated from equation (2-1):

$$V_s = V_{s,ref}\left(\frac{p}{p_{ref}}\right)^{1/n} \tag{2-1}$$

where V_s is the shear wave velocity; $V_{s,ref}$ is a reference shear wave velocity; p_{ref} is a reference stress; p is the mean stress; and n is a calibration parameter to be computed from results at different confinements. Using laboratory results at 50, 100 and 200 kPa, the best fit was obtained for $n = 2.3$, $V_{s,ref} = 200.3$ m/s and $p_{ref} = 50$ kPa. Using this equation, a harmonic average of the shear wave velocity inside the container was computed considering ten layers of soil (see Figure 2-9a):

$$\bar{V}_S = \frac{\sum_{i=1}^{n} \Delta h_i}{\sum_{i=1}^{n} \frac{\Delta h_i}{V_{S,i}}} \tag{2-2}$$

The mean shear wave velocity in the box would be about 59.7 m/s. This value was obtained assuming an at-rest coefficient of lateral earth pressure equal to 0.5. Thus, according to the standard solution for a homogenous elastic layer over an elastic half-space, a first estimation of the first resonance frequency of the soil container f_0 is close to 15.1 Hz.

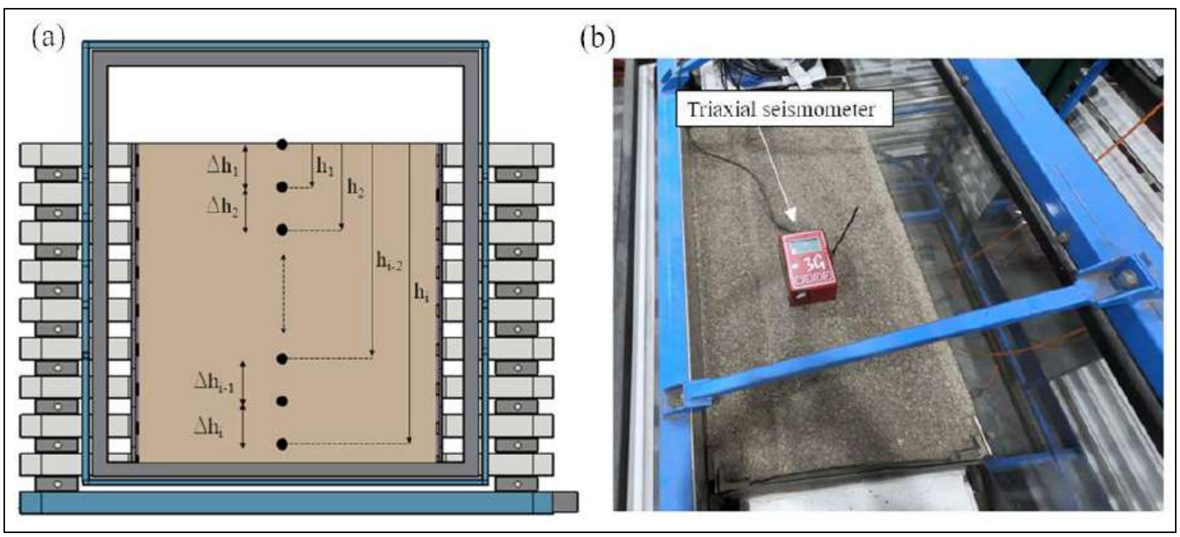

Figure 2-9: (a) Spacing intervals of layers; (b) Soil container and triaxial seismometer located on its surface

The predominant frequency of the soil in the laminar box could be measured using records of ambient noise, by means of the Horizontal-to-Vertical Spectral Ratio (HVSR) or Nakamura’s method (Nakamura, 1989), and by the empirical transfer function obtained from the ratio of the Fourier Spectrum at the surface and at the base of the container. The instrumentation for this measurement consists of a three-component high sensitivity seismometer able to measure ambient noise (Figure 2-9b).

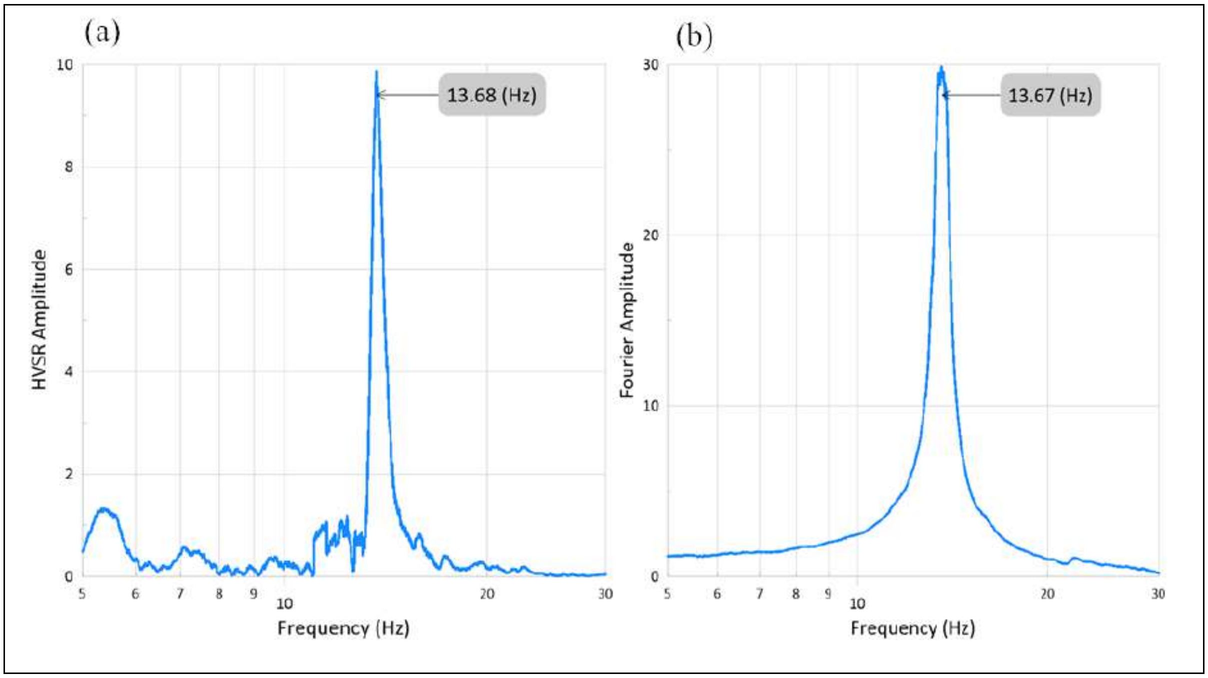

Figure 2-10: Fundamental frequency of soil container based on ambient vibration measurements: (a) HVSR; (b) Transfer function.

Figure 2-10a shows the HVSR amplitude curve from an ambient noise recording of 20 minutes using a triaxial portable seismometer placed on the surface of the sand (Figure 2-9b), while Figure 2-10b shows the empirical transfer function obtained from ambient noise recorded at the base and at the surface of the container. Both results are in good agreement with the first resonance frequency analytically estimated of 15.1 Hz. Differences are probably related to the estimation of the soil confinement in the box and because Eq. (2-1) was calibrated at confinements greater than those in the box.

2.4.3 Shear stress-strain and damping analysis

The hysteretic soil behavior was analyzed at three different confinements (or depths) inside the container, using the data from the accelerometers shown in Figure 2-3 (accelerometer method or ACC). Thus, dynamic soil properties, shear modulus and damping ratio can be estimated from the theory of one-dimensional shear beam described in Zeghal et al. (1995) (Eq. (2-3)). This equation can be expressed in its discrete form by considering a linear interpolation between the different depths (Eq. (2-4)):

$$\tau_{(z,t)} = \int_0^z \rho \, \ddot{u} \; dz \tag{2-3}$$

$$\tau_{i(t)} = \sum_{k=1}^{i-1} \rho \frac{\ddot{u}_k + \ddot{u}_{k+1}}{2} \Delta z_k \tag{2-4}$$

where τ represents the shear stress, ρ is the density of the soil, $\ddot{u}$ is the absolute acceleration and z is the depth along the soil column or, in the discrete case, Δz_k is the vertical spacing interval.

The shear strain is evaluated from values obtained by double integration of the acceleration data at levels z_i (Eq. (2-5)), then:

$$\gamma_{i(t)} = \frac{u_{i+1(t)} - u_{i(t)}}{\Delta z_i} \tag{2-5}$$

where $\gamma_{i(t)}$ is the shear strain, $u_{i+1(t)}$ and $u_{i(t)}$ are the absolute displacements at levels z_{i+1} and z_i, respectively. The shear modulus, G, is approximated by Eq. (2-6), which represents the secant slope of an idealized shear stress-strain loop (see Figure 2-11).

$$G = \frac{\tau_{(\gamma_m)}}{\gamma_m} \tag{2-6}$$

While the damping ratio, D, was evaluated by calculating the dissipated energy, W_d, and elastic energy, W_e, as follows:

$$D = \frac{W_d}{4\,\pi\,W_e} \tag{2-7}$$

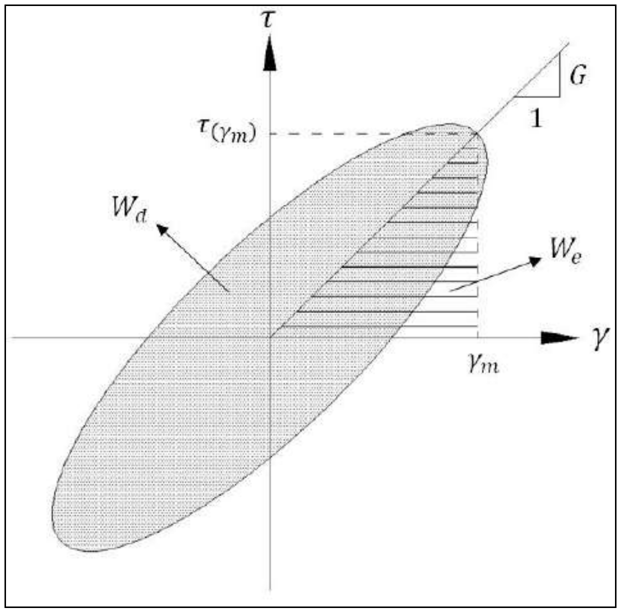

Figure 2-11: Idealized hysteresis loop. W_d is the dissipated energy, W_e is the elastic energy and G represents the secant shear modulus

The same expressions have been considered to generate a second estimation based only on Digital Image Correlation. Because horizontal displacements are directly estimated by DIC, no double integration of records is required. The three representative loops shown in Figure 2-12 correspond to an input motion of 5 Hz of frequency and 0.3 g of amplitude; these illustrations are based on ACC and DIC measurements considering the same time window, depth and input motion. In general terms, both sets of results agree in terms of secant stiffness and damping; however, ACC-derived loops are smoother. Two datasets in the deepest loop show a slightly different inclination (or secant stiffness), while damping (or inner area) is similar. On the other hand, damping differences can be noted in the shallower loop.

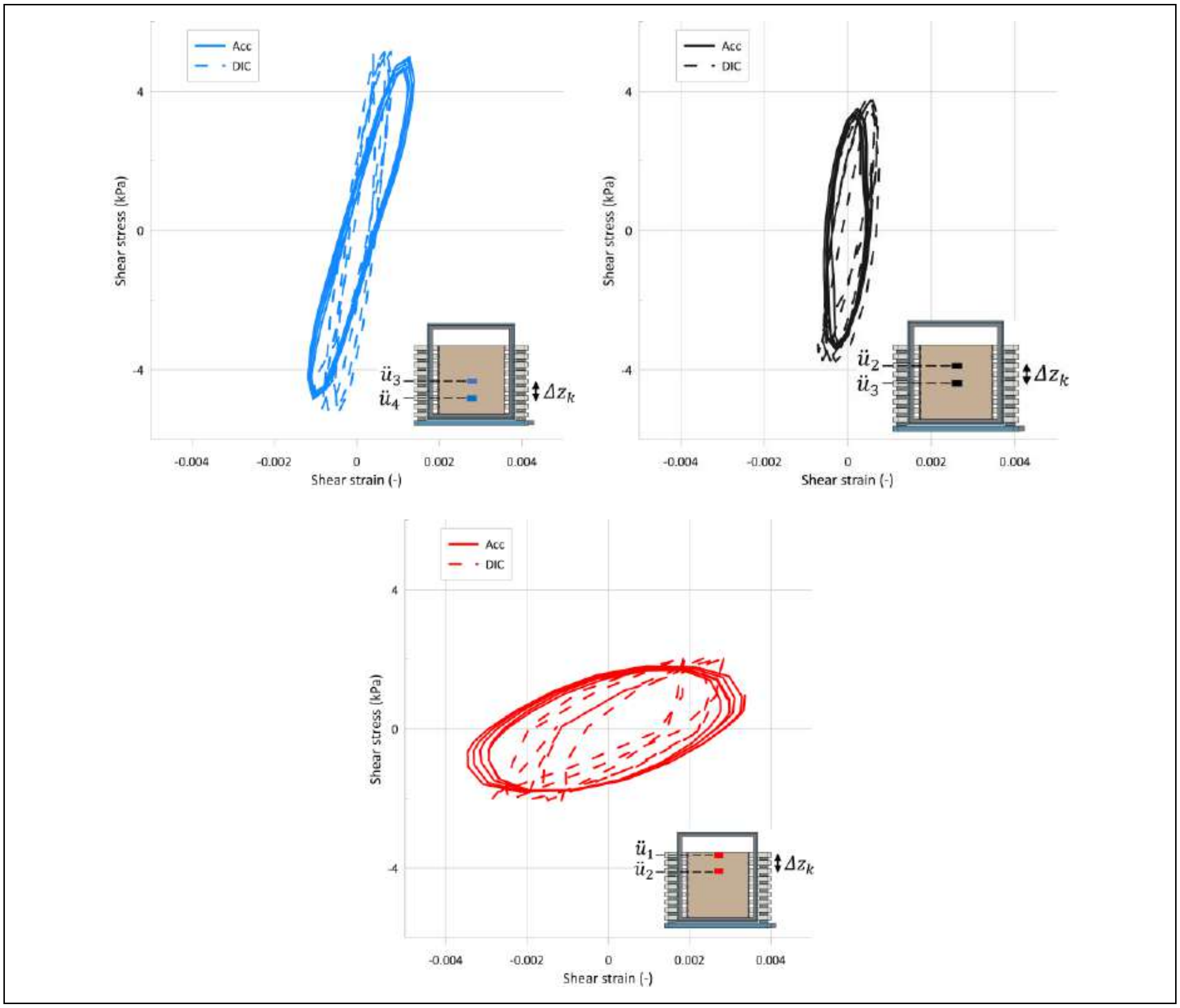

Figure 2-12: Comparison between hysteresis loops at different confinements

The modulus reduction and damping curves are analyzed based on test groups 3, 4 and 5 (Table 2-1), where all input motions are classified according to a peak input acceleration of 0.3 g, 0.2 g and 0.08 g, respectively. Figure 2-13a-b summarize results from ACC in comparison to standard laboratory testing. In general terms, a good agreement between RC/TS and accelerometer measurements was obtained. As expected, results corresponding to 0.08 g-input are generally stiffer because of lower cyclic shear strains in the range from 1 to 2×10^{-2}%. On the contrary, strong input motions induce a more pronounced degradation, reaching maximum cyclic shear strains of about 10 %. The fourth group of tests at 0.2 g generates intermediate strains. The damping curve (Figure 2-13b) shows some dispersion for values larger than 1.5×10^{-1}%. Differences could be related to variable confinement depending on the location of the accelerometers, since RC/TS and reference curves were obtained at fixed confinement of 50 kPa. Conversely, confinements for Acc 5, Acc 6 and Acc7 are approximately 9, 6 and 3 (kPa), respectively. It is important to note that the minimum observable shear strain was about $1 \times 10^{-2}\%$ from this series of tests.

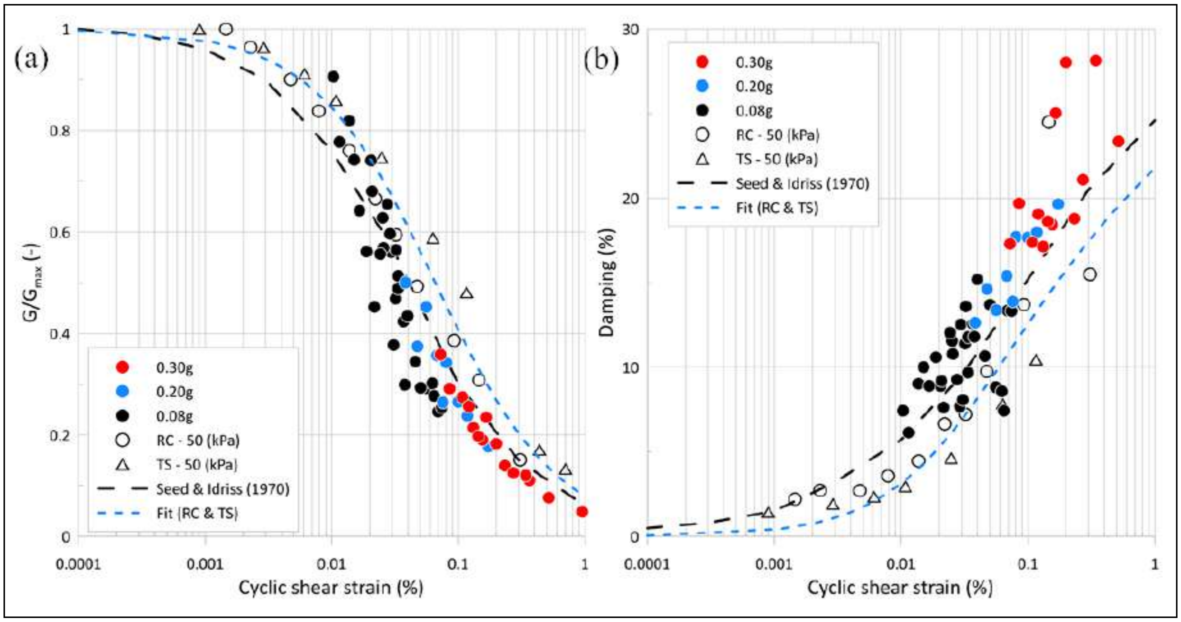

Figure 2-13: Accelerometer method: (a) Shear modulus degradation curve; (b) Damping increase curve

The same analysis was repeated but using only DIC data. Thanks to the transparent front side, it was possible to directly measure the displacement of the soil between areas much shorter than ACC and it is limited only by the number of pixels. Thus, the capability to measure and analyze any area of each photogram becomes the most significant feature. Using the same approach, additional results are shown in Figure 2-14a-b. In contrast to ACC, only 2 input motions were required to compute the reduction of shear modulus and damping curves instead of the 18 tests required by ACC (i.e., Test groups 3, 4 and 5). Figure 2-14a-b also display data obtained from ACC using the same two inputs. This comparison illustrates the benefits and accuracy of applying DIC for dynamic problems.

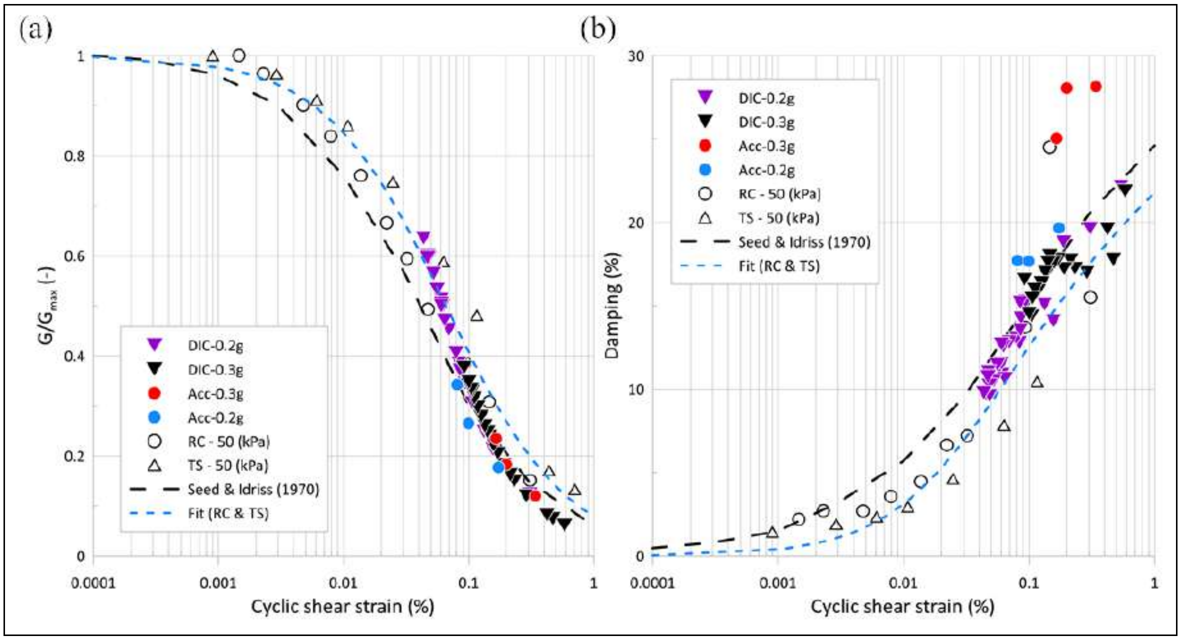

Figure 2-14: DIC method: (a) Shear modulus degradation curve; (b) Damping increase curve

Different levels of shear strain are related to different depths inside the soil container, i.e., the confinement is not constant between points in these curves. This variability of the confinement could partially explain differences between laminar shear box results and RC/TS test, but also the deformation field of the soil is different. Minimum observable strains are of about 4×10^{-2} (%), which was very similar to what we were able to characterize using the accelerometers. This value is small enough for many earthquake applications, but probably could be reduced using a higher resolution camera (higher than 4.1 MP camera used for this investigation), or by using a camera array as suggested in Eichhorn et al. (2020). However, using a higher resolution does not guarantee better results, because other aspects such as particle-size, frequency, texture quality, signal to noise ratio, optical distortion, strain localization, among many others experimental conditions, affect the accuracy of the measurements.

2.4.4 Continuous field displacement estimation by DIC

As described in Section 3.1, the design of the laminar box includes a mirror to increase the distance between the object (the soil container) and the camera, to avoid the use of a wide-angle lens that might introduce some distortion to the image. Consequently, the camera appears in each picture as it is shown in Figure 2-15a. To obtain a continuous displacement field, the DIC analysis was performed in two steps. Firstly, the image correlation is run by removing a region that includes the camera and its supporting beam (dashed area in Figure 2-15a). Secondly, a linear interpolation was performed to fill the area removed in the first step.

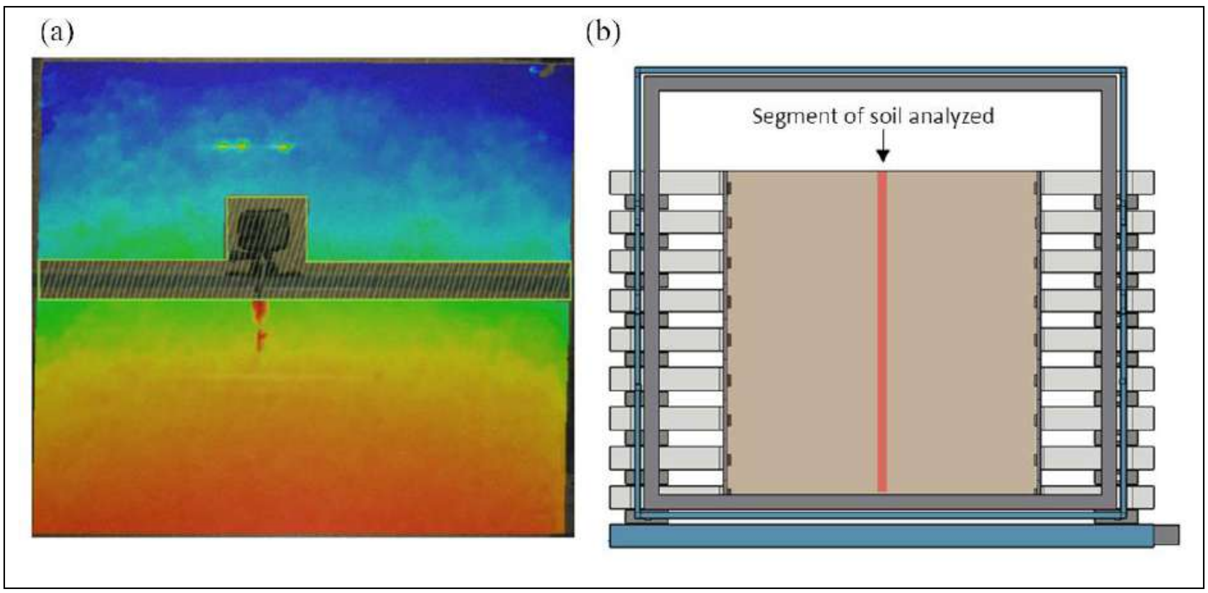

Figure 2-15: Continuous field displacement interpolation based on DIC: (a) Sample processed image prior to interpolation; (b) Vertical segment sample in the soil container.

To compare the continuous DIC measurements profile against the discrete accelerometer readings, a vertical segment of the soil was selected (see Figure 2-15b). For this analysis, two analytical functions characterized by different frequencies were used (Figure 2-16a-b), identified as Test 6 and 7 in Table 2-1. These frequencies have been selected far enough from the first natural frequency of the soil of about 13.67 Hz, to avoid resonance. The first input was a Ricker wavelet with a peak base acceleration of 0.6 g and a mean frequency of

3 Hz. The second input was a modulated harmonic signal of 6 Hz of frequency, characterized by a peak acceleration of 0.9 g.

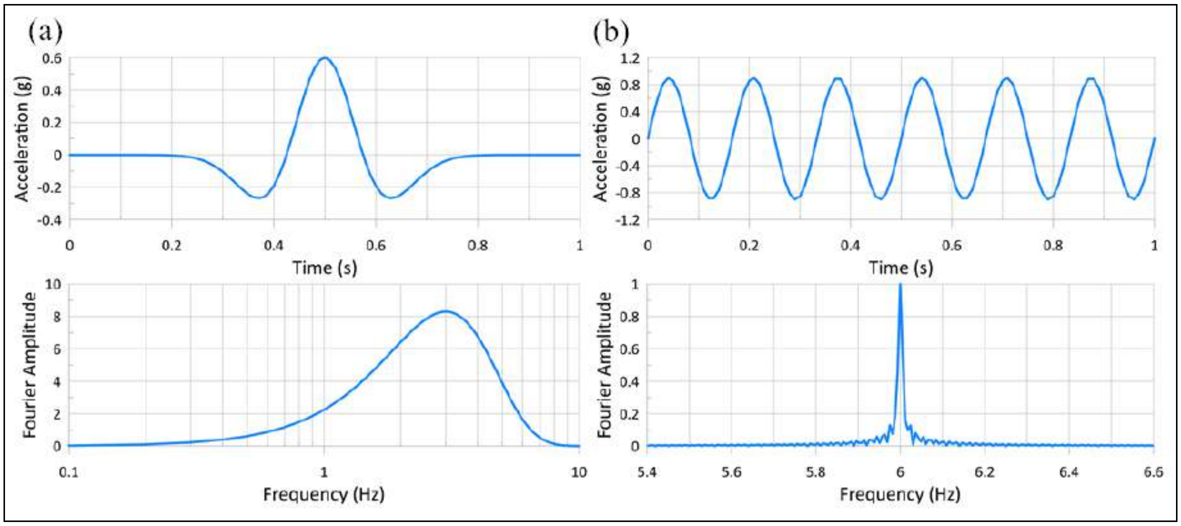

Figure 2-16: Selected input motions: (a) Ricker wavelet: f=3 Hz, A=0.6 g; (b) Harmonic input: f= 6 Hz, A=0.9g

Results presented in Figure 2-17a and Figure 2-17b show lateral displacement of the vertical soil section every 0.05 seconds approximately. Displacements from double integration of accelerometers are also included in these figures for comparison purposes. Continuous lines correspond to profiles obtained with DIC, while dashed lines are linear interpolations between accelerometers. These displacements are relative to the base of the container. However, in the deepest part of the box, the first 4 cm are hidden by the steel frame. These images illustrate that it is possible to obtain a continuous displacement field of the soil response during dynamic analysis. It is important to note the lateral displacements as low as 0.5 mm were identified. In general terms, horizontal displacements from DIC or accelerometers are similar in the upper third of the box; nevertheless, more significant differences could be noted at the center and in the lower third of the box. Indeed, displacements close to the free surface are very similar. In the lower part of the box, differences are probably of the same order as the upper part, but because absolute displacements are smaller, this difference becomes more evident. However, the overall displacement profile is correctly estimated by DIC in terms of shape and mean amplitude. Of course, the main advantage is the continuous information obtained from DIC, i.e. each vertical profile has about 95 points, taking a reading at 0.01 m intervals, while only four data points are available to obtain the vertical profile of displacements from accelerometers. Differences between DIC and accelerometers can come from many sources; for example, the accelerometers can rotate inside the soil or there may be an influence of the friction between the glass and the soil on the photographed face. The quantification of friction effects at the front glass side is discussed in the next section.

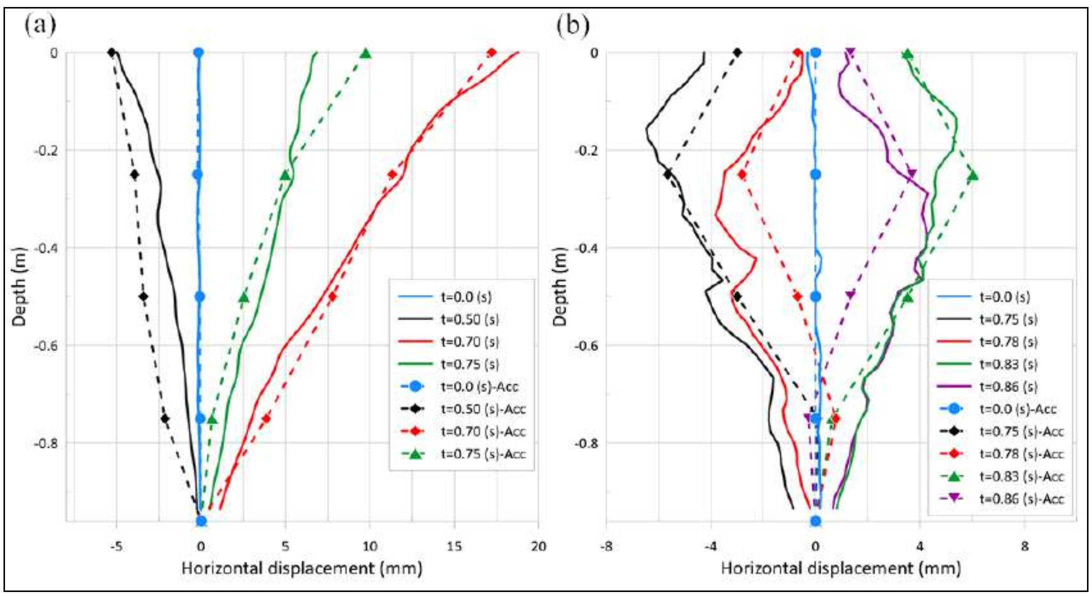

Figure 2-17: Relative horizontal displacements inferred from DIC: (a) Ricker wavelet, mean frequency = 3 Hz, A = 0.6 g; (b) Harmonic, mean frequency = 6 Hz, A = 0.9g

To illustrate the effects on the results of the settings used for DIC, Figure 2-18 shows the profile of horizontal displacements at t=0.70s for the 0.6g amplitude Ricker wavelet for two other combinations of subset and step sizes, as well as for two other correlation criteria: the Normalized Sum of Squared Differences (NSSD), which accounts for scaling in intensity, and the Zero-Normalized Sum of Squared Differences (ZNSSD), which accounts for offset and scaling in intensity variations. The only difference between NSSD and ANSSD is the approximation of the Hessian by a multiplication of the Jacobians included in the later. In Figure 2-18a-c, the displacements inferred from the accelerations are included as reference. The range of explored combinations does not have a significant impact on the results, although a more pronounced impact of the correlation criterion can be noted for the case of subset size of 21 pixels. In this case, ZNSSD criterion produces smaller horizontal displacements at the upper third of the container. On the other hand, the combination of 25 pixels subset size and 10 pixels step size tends to provide smoother results, probably because it averages a slightly larger area. Nevertheless, the obtained results are equivalent for the purposes of this investigation.

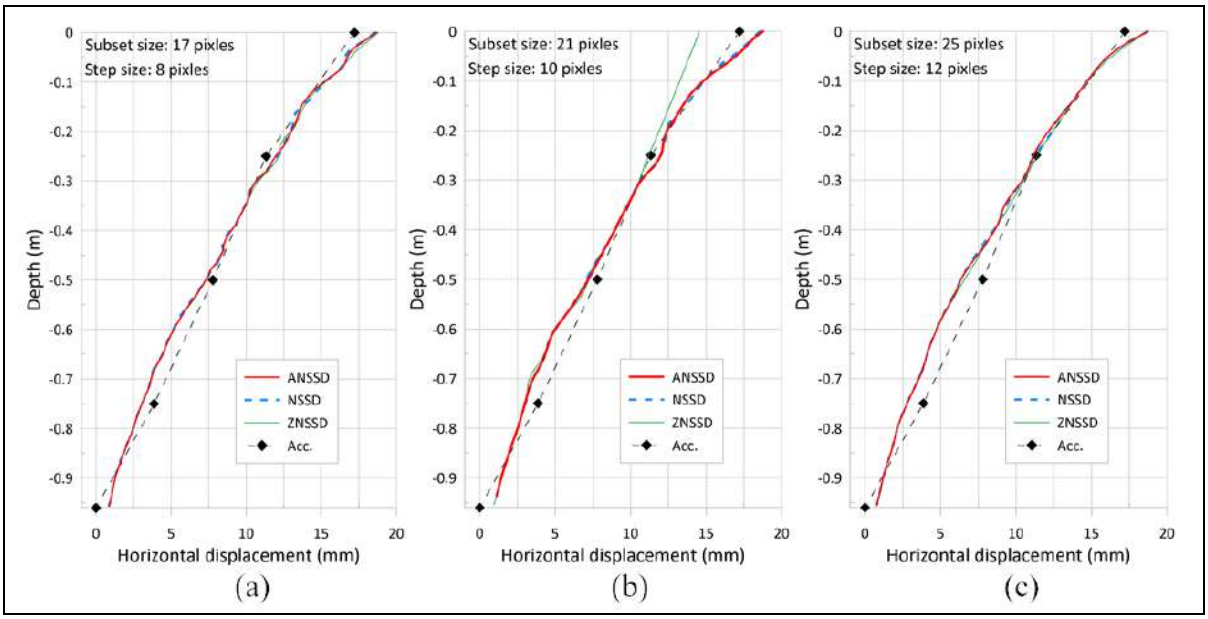

Figure 2-18: Relative horizontal displacements inferred from DIC a t=0.70s for a Ricker wavelet of mean frequency = 3 Hz and A = 0.6 g: (a) Subset size of 17 pixels and step size of 8 pixels; (b) Subset size of 21 pixels and step size of 10 pixels; (c) Subset size of 25 pixels and step size of 12 pixels

On the other hand, a complete displacement field could be obtained from DIC analysis. Figure 2-19 displays the results when the soil is subjected to the Ricker wavelet described above. The interpolated area is demarcated by black squares. The motion can be visualized and properly analyzed at each time step (i.e., 60 fps). It can be noted that in the lower half of the box, the behavior is approximately 1D as expected; nevertheless, some boundary effects are evident especially close to the surface when lateral displacements are larger than those computed at the center of the box. In this area of the container, the confinement is very low, and consequently the material becomes more deformable. Because of this limited stiffness, deformation is increased by the supplementary shear stress induced by lateral wall movements.

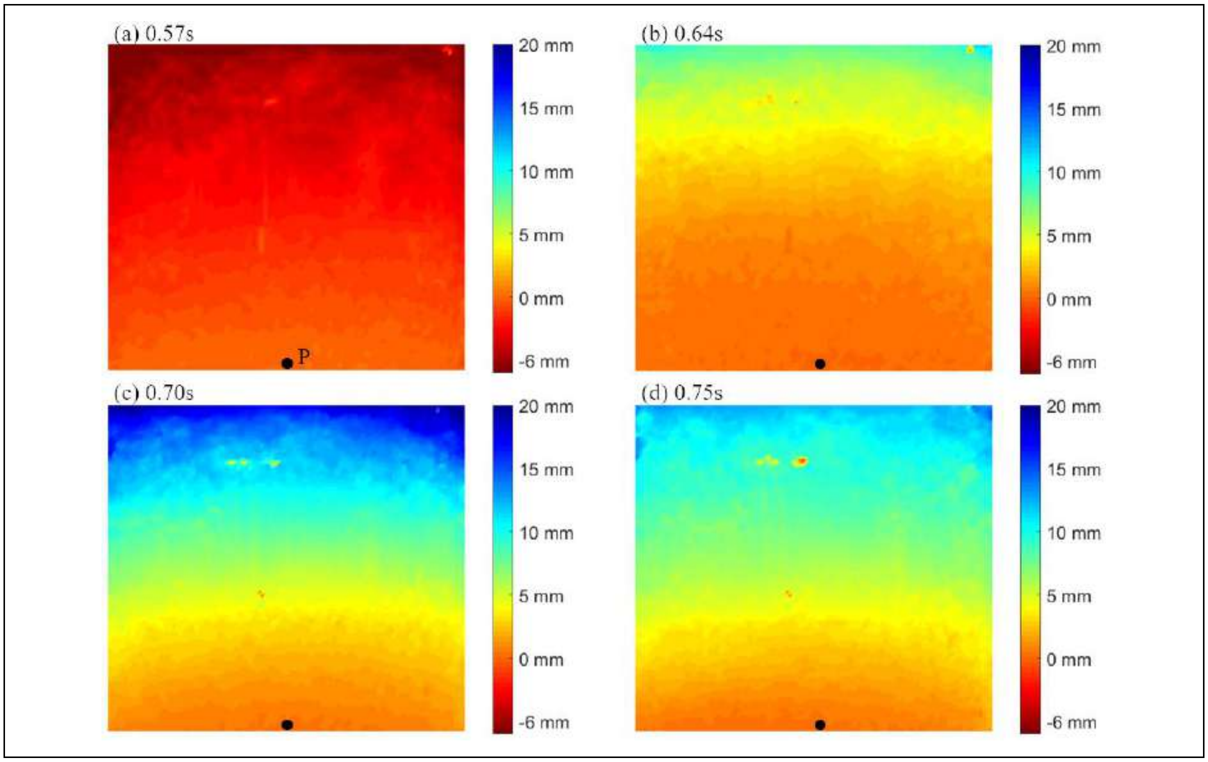

Figure 2-19: Relative horizontal displacement field inferred from DIC

Figure 2-20 shows the relative displacement obtained by DIC at a deep point (P), at 94 cm deep from the soil container surface. It can be noted that even displacements below 0.2 mm can be properly tracked using this technique.

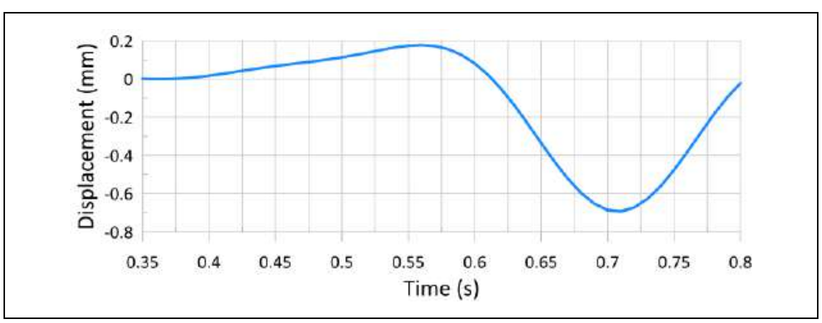

Figure 2-20: Displacement at depth P = 0.94 (m)

2.4.5 Uncertainty quantification of displacement estimation from DIC

Any measurement process has a certain error associated and, therefore, a level of uncertainty regarding its results. According Fayad et al. (2020), there are two main sources of error when using DIC, firstly arising from the numerical matching of the displacement field using some type of minimization scheme and image interpolation, and secondly, experimental error sources. The device developed for this research is not exempt from these errors, and two analyzes were carried out to provide indicators of these errors, as discussed in this section.

With the purpose to assess the first source of error, a large set of images were analyzed before the beginning of the motion, to quantify the uncertainty in the displacement measurements. Two points were analyzed, one located at the surface of the model and the second at 0.2 m of depth. Figure 2-21 shows both horizontal displacements obtained from DIC analysis. Because the motion during this static stage should be zero, we added in this figure a zoom of the first 1.2 seconds. According to the fluctuation observed in this figure, the mean horizontal displacement is slightly below ± 0.01mm and it can reach up 3 times this value as maximum. From this analysis we can conclude that the noise in the measurements should not exceed ± 0.03mm, which is about of one order of magnitude less than the lowest value used to construct the degradation curves.

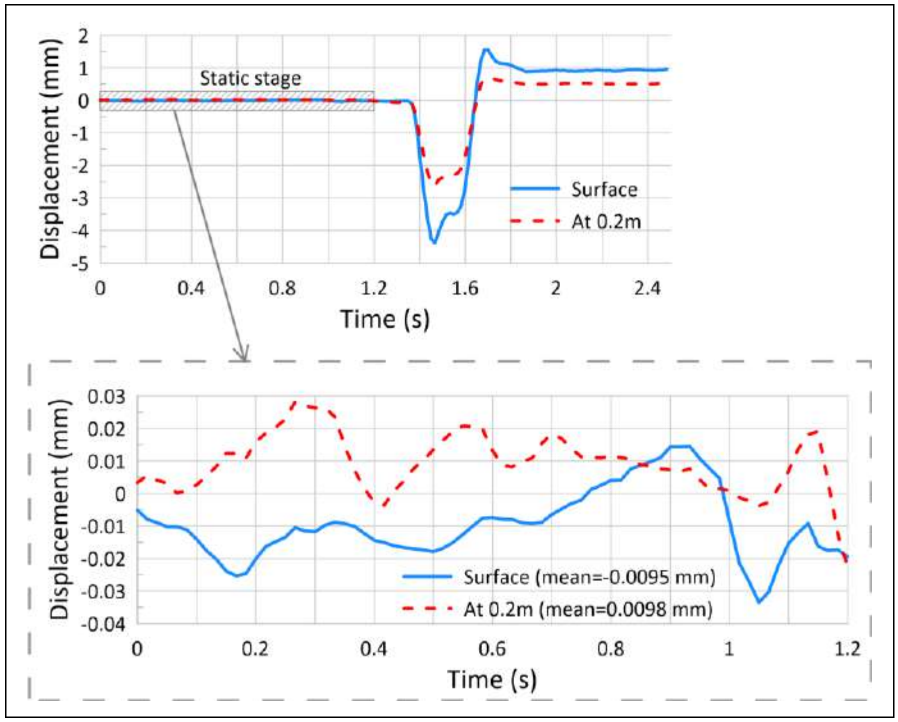

Figure 2-21: Displacements inferred by DIC at two control point for a Ricker wavelet of mean frequency = 2.3 Hz and A = 0.65 g and detail during static stage

Additionally, since the camera support is fixed to a beam of the frame that supports the soil container, there is a possibility of relative motion of the camera that can affect the measurements. To quantify this effect, we carried out a complementary analysis to assess the amplitude of this possible relative motion. To estimate this relative motion, we took advantage of a bolt in the steel frame that supports the glass, which was captured in the image. If the DIC analysis shows movement of the bolt, this would actually be movement of the camera and its support system. Results of this analysis are shown in the Figure 2-22 for the case of Ricker input of 3 Hz and 0.6g amplitude. Results indicate that the vibration of the shaking table trigger a vibration of the camera that produce a maximum relative displacement of about 0.10 mm in the image. As can be seen in the Figure 2-22d, at the instant of maximum surface movement (t = 0.7s), this relative movement is approximately -0.06 mm, which is twice our estimate of uncertainty. Consequently, we believe that there is not significant error introduced by the relative motion of the camera for the system shown in paper. Indeed, according to Figure 2-17a, the horizontal displacements of the soil in the container are at least an order of magnitude greater during the induced motion.

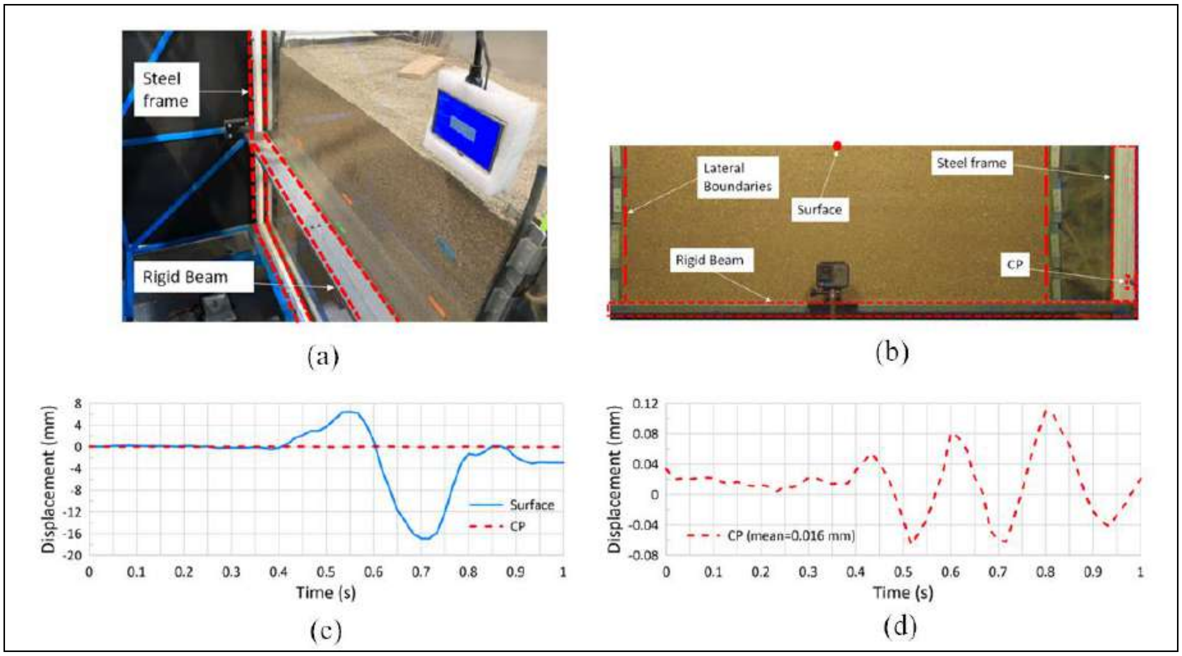

Figure 2-22: Relative motion assessment: (a) detail of the beam where the camera is fixed and steel frame ; (b) control point (CP); (c) Horizontal displacements at surface and CP ; (d) Relative motion estimation

2.4.6 Assessment of the friction on the transparent side

A computational model was performed to study the effects of boundary conditions of the experiment, such as the friction between the front side of the soil and the glass (Figure 2-23). The main purpose is to assess whether differences between DIC analysis and accelerometer measurement can be related to friction effects on the transparent side. The nonlinear analysis was conducted in the software LS-DYNA®; the soil material used was MAT_HYSTERETIC_SOIL due to the feasibility to reproduce the pressure-dependent soil behavior and cyclic degradation of the material. The main properties were calibrated based on the confinement dependent model of shear wave velocity presented in Eq. (2-1), as well as modulus degradation and damping increase curves shown in Figure 2-5. The developed mesh is shown in Figure 2-23. A stratified model of ten horizontal layers has been considered and each layer has uniform elastic parameters. The usual Coulomb friction criterion was considered for front and back faces, while kinematic constraints were considered on the lateral sides to force the shear-beam kinematic characteristic of laminar boxes. The dynamic motion is imposed as a prescribed displacement at the base of the finite element model. The motion shown in Figure 2-16a was selected for comparisons.

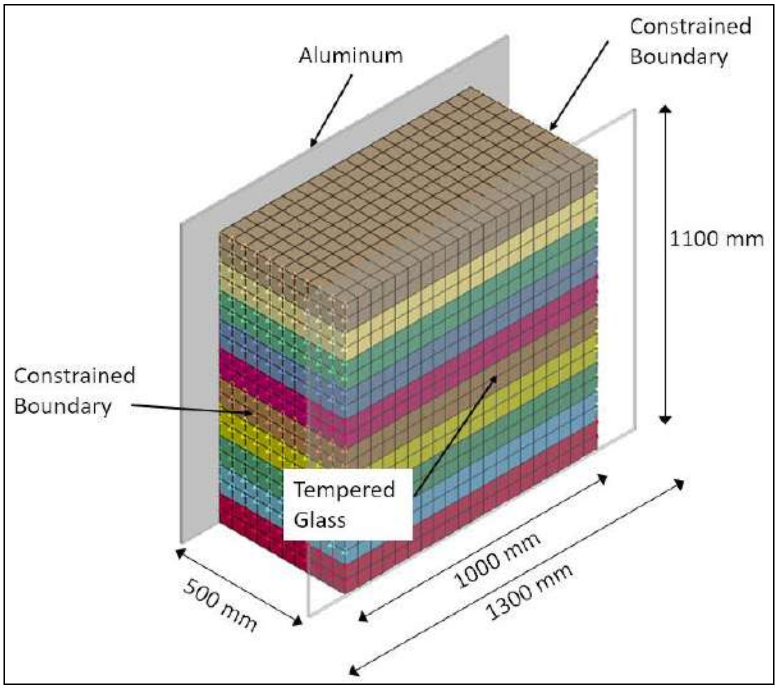

Figure 2-23: Finite element model (LS-DYNA)

The lateral friction model is driven by a dynamic friction coefficient (Fd). Figure 2-24a demonstrates the influence of this parameter on the lateral displacement of the soil in the middle of the box (where the accelerometers are located) and in the front glass, where DIC was used. To define the most suitable coefficient, a sensitivity analysis was performed by exploring different values of friction. As can be seen in Figure 2-24a, in general terms, the influence of the lateral friction coefficient is reduced in terms of the displacement differences between the middle and the photographed face; nevertheless, a significant influence can be noted on the values of the displacements. Comparing the results of the model against the available measurements, only low friction coefficients, i.e., about Fd = 0.1, produce a reasonable similarity between computed and observed displacements; for example, greater frictions tend to slow down movement both at the center of the container and at the glass face. On the other hand, according to the computational model with a value of Fd = 0.1, lateral friction has a minor impact on horizontal displacements and therefore would not explain the differences between the results of the accelerometers and the use of DIC. Figure 2-24b and Figure 2-24c present the comparison between the model and experimental results for two other instances. In general terms, the adjustment of the computational model improves as displacements grow. At the beginning of the motion (before 0.5s), experimental measurements show values of the order of twice what was predicted by the model in the upper part of the container; nevertheless, during the stronger part of the shaking, a relative horizontal displacement very close to the observations was produced. At the bottom of the container, they are closer to the accelerometer measurements, while at the top they are closer to the DIC results. In general terms, the computational approach is good enough to reproduce the key aspects of the nonlinear soil behavior in the container during the shaking, especially close to peak value at about 0.70 s.

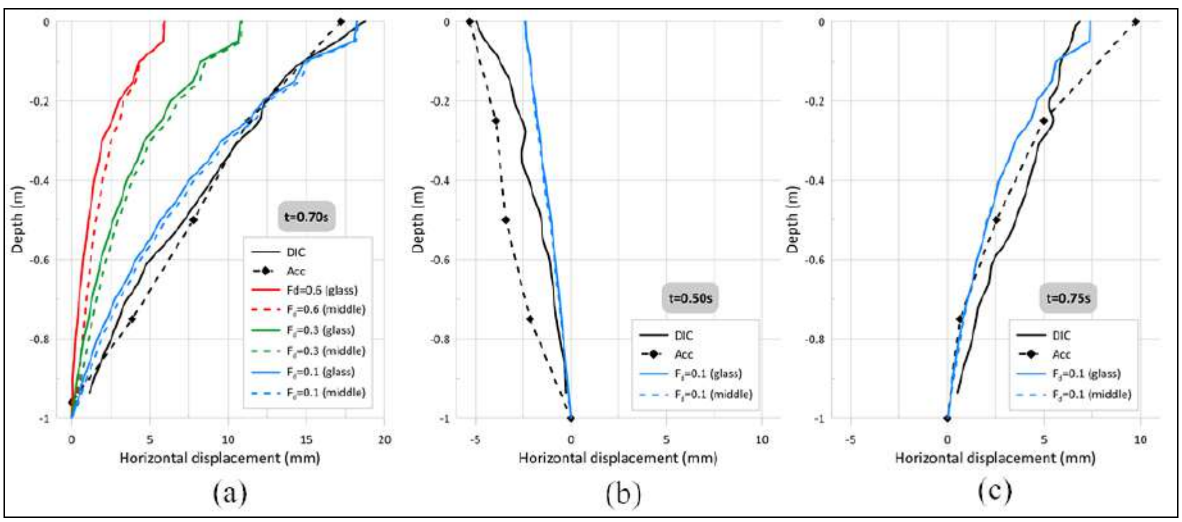

Figure 2-24: Relative horizontal displacement using a Ricker wavelet of f=3 Hz and A=0.6 g: (a) Effect of increasing the dynamic friction coefficient at 0.70 s. Comparison of numerical and experimental profiles: (b) at 0.5 s and (c) at 0.75 s

Despite the satisfactory agreement between the results obtained from the DIC analysis and ACC, the difference between observations varies depending on location and time. To provide a more quantitative comparison, relative differences are computed and presented in Table 2-2. In general, differences between both sets of experimental data are in the range of 6% to 30% in absolute terms in the upper half of the box container. These differences increase up to 50% when compared to the computational model. In the lower half of the box, relative differences increase, even exceeding 100% in one case, but in absolute terms, they remain in the order of 0.5 to 2 mm, as shown in Table 2-3. Consequently, the absolute differences are not significantly different in terms of the depth or the moment in time of the observation. In summary, according to computational results, there is no evidence that friction on the photographed face explains the differences between accelerometers and DIC measurements. The differences could be more related to experimental effects such as rotation of the accelerometers, brightness in the images, approximation errors from the double integration or double derivation of the data sets to be able to compare them, among other possible effects.

Table 2-2: Relative differences (%).

Depth (mm)	Acc - DIC			Acc – F_d=0.1 (middle)			DIC – F_d=0.1 (glass)		
	t_2=0.50 s	t_3=0.70 s	t_4=0.75 s	t_2=0.50 s	t_3=0.70 s	t_4=0.75 s	t_2=0.50 s	t_3=0.70 s	t_4=0.75 s
0	-6.0	9.0	-29.7	-54.8	6.3	-24.2	-52.2	-2.9	7.9
240	-35.6	5.8	10.0	-53.8	3.1	-13.2	-30.4	-5.8	-21.5
480	-54.4	-7.5	39.1	-67.4	-23.1	-18.9	-32.5	-21.0	-40.7
720	-64.6	-22.5	133.1	-74.9	-34.9	36.4	-33.5	-24.8	-45.6

Table 2-3: Absolute differences (mm).

Depth (mm)	Acc - DIC			Acc – F_d=0.1 (middle)			DIC - F_d=0.1 (glass)		
	t_2=0.50 s	t_3=0.70 s	t_4=0.75 s	t_2=0.50 s	t_3=0.70 s	t_4=0.75 s	t_2=0.50 s	t_3=0.70 s	t_4=0.75 s
0	0.3	1.6	-2.9	2.9	1.1	-2.4	2.6	-0.5	0.5
240	1.4	0.7	0.5	2.1	0.4	-0.7	0.8	-0.7	-1.2
480	1.9	-0.6	1.0	2.3	-1.8	-0.5	0.5	-1.5	-1.4
720	1.4	-0.9	0.9	1.6	-1.3	0.2	0.3	-0.7	-0.7

2.5 Conclusions

Dynamic soil behavior was characterized during one-dimensional shear wave propagation in a transparent laminar shear box on a shaking table. The ability of DIC to capture nonlinearity of the soil behavior during the load was validated. The continuous information obtained could be successfully processed; however, it is clear that the improvement of the camera resolution or the use of a camera array is a key aspect to consider in future work in order to measure smaller deformations in the soil.

The performance of the container in a wide range of frequency and amplitude was analyzed. According to the obtained results, lateral boundary effects are negligible and far enough from the free surface.

Dynamic soil properties determined in the shaking table are in good agreement with experimental results observed in cyclic torsional and resonant column tests; nevertheless, the use of accelerometers at different confinements presents better results than DIC in terms of minimum observable shear strain. The degradation curve obtained by accelerometers contains the data of 18 tests, whereas the curve obtained from DIC analysis was performed only with 2 harmonic tests of variable amplitude; DIC allows more information to be extracted than traditional dynamic instrumentation.

The influence of the friction between the walls and the soil was studied by the finite element method. It was determined that higher values of the dynamic friction coefficient mainly affect the amplitude of the soil displacements and have a limited influence on the displacements observed on the transparent face. Thus, friction on the photographed face is not enough to explain the differences between accelerometers and measurements with DIC.

The transparent laminar shear box developed provides an opportunity for monitoring the dynamic displacement field in a continuous way, making it possible to perform a direct comparison against an array of accelerometers inside the soil; it also provides significant information to study the performance of numerical models and to improve the understanding of the strain distribution during dynamic loading.

3. EVALUATION OF DYNAMIC SOIL-STRUCTURE INTERACTION EFFECTS IN BUILDINGS WITH UNDERGROUND STORIES USING 1-G PHYSICAL EXPERIMENTATION IN A TRANSPARENT SHEAR LAMINAR BOX

3.1 Introduction

The phenomenon of Dynamic Soil-Structure Interaction (DSSI) can play an important role in the seismic response of a building. The interaction between the building and surrounding soil is influenced by the contrast of stiffness that exists between both domains, the travelling waves through the soil are modified when they reach the foundation due to the abrupt increase of stiffness (kinematic interaction, KI). On the other hand, the forces that are transmitted from the structure's vibration to the foundation produce energy dissipation, since the soil provides flexibility to the system (inertial interaction, II). As a result, one of the main effects that has been identified on the dynamic properties of the structure is the increase on its vibration period and global damping.

The DSSI effects have attracted attention of researchers since 1970's, when the dynamic design of nuclear facilities took great importance (e.g. Lee & Wesley, 1973; N. C. Tsai et al., 1974; Matthees & Magiera, 1982). Several authors contributed to the development and investigation of this phenomenon, under the assumption of an elastic soil behavior (e.g. Luco & Contesse, 1973; Veletsos & Verbič, 1973; Chopra & Gutierrez, 1974; Kausel, 1981; Bielak & Christiano, 1984; Wolf & Obernhuber, 1985; Dobry and Gazetas, 1987, Pais & Kausel, 1988; Wolf, 1989). These works were deeply associated to the theory of machine foundation vibration. Later, Gazetas (1991), developed a compilatory work of impedance functions (i.e., dynamic stiffness) for surface and embedded foundations. In general, the influence of foundation embedment had been studied on the context of an elastic half-space media (Seed & Idriss, 1973; Bielak, 1974; Elsabee & Murray, 1977).

Avilés and Pérez-Rocha (1998) investigated the influence of foundation embedment on the effective period and damping, concluding that inertial effects are more significant than kinematic effects. In addition, Stewart et al. (1998) verified that the fixed base and flexible base periods are quite similar for slightly embedded structures, but damping ratio can increase in deeper embedded structures. Inertial interaction effects are commonly considered to have the greatest influence on DSSI (Stewart, Fenves, et al., 1999; Stewart, Seed, et al., 1999); as result, most building codes pay attention only on II effects, and KI effects are rarely considered (FEMA P-2082-1, 2020). Some recommendations for the analysis of significance of both interaction effects can be found in FEMA P-2091 (2020).

Takewaki et al. (2003) proposed a simple method to evaluate the SSI of embedded structures using the theory of cone models (Meek & Wolf, 1994). Mahsuli et al. (2009) studied DSSI effects as a function of the foundation embedment with emphasis on KI. They concluded that the ductility demand depends on the embedment depth. Saxena and Paul (2012) investigated the slip and separation between embedment levels and the surrounding soil. Clouteau et al. (2012) developed a coupled FEM-BEM approach to model DSSI for shallow and embedded foundations. The filtering effect on embedded foundations was studied by Conti et al. (2017). They found simplified expressions from dimensional analysis by relating the wave length and the foundation depth. Fu et al. (2017, 2018) reported numerical results of impedance functions considering the length-to-width ratio for embedded rectangular foundations. Bararnia et al. (2018) investigated the effects of the rocking foundation input motion on inelastic displacement ratios for embedded foundations. In addition, the influence of KI and II on the strength-ductility-period relationship was studied by Ahmadi (2019). Moreover, alternative methods were explored to incorporate nonlinear DSSI on embedded foundations, which are based on Winkler models (Asadi-Ghoozhdi et al., 2020). Analytical expressions to modify input motion at the basement level were provided by Sotiriadis et al. (2020).

In addition, the problem of dynamic pressures on soil-walls systems has been the subject of studies for decades. The simplest methods for evaluating these pressures are based on the original proposal by Scott (1973) that uses a far-field response evaluated through a fixed based vertical cantilever shear-beam connected to the wall through elastic horizontal massless springs. Later, Veletsos and Younan (1994) modified Scott's approach by introducing semi-infinite horizontal bars with distributed masses. However, seismic pressures differ significantly between “yielding” and “non-yielding” walls because the deformation modes are very different. In the case of non-yielding walls, such as the undergrounds walls studied in this paper, there is an analytical solution under the elastic soil hypothesis introduced by Wood (1973). According to this analytical model, the computed dynamic pressure increase is zero at the base of the wall and maximum at the top of the backfill with a recommended point of application of the resulting force at 60% of the height of the wall. This result has subsequently been revised, for example experimentally by Sherif et al. (1982) or analytically by Ostadan (2005) who illustrated the role of frequency content in the value of maximum dynamic pressure. However, very few structures are based on perfectly rigid walls, motivating several authors to study the role of soil-wall flexibility in the dynamic pressures, either experimentally (e.g., Wagner et al, 2016; Hushmand et al, 2016) or analytically (e.g., Brandenberg et al, 2020; Durante et al, 2022) proposing design procedures which take into account this effect.

The implementation of physical models at a reduced scale has been employed for decades to improve the comprehension of complex dynamic characteristics problems. The possibility of adjusting the studied variables and controlling the experimental conditions, becomes an outstanding advantage to understand in a clear and practical manner physical aspects of a given problem. In earthquake geotechnical engineering, the use of laminar containers capable of replicating the free field boundary conditions of the soil, have been used for many years to study DSSI problems (Wood et al., 2002; Jafarzadeh, 2004; Prasad et al., 2004; Brennan et al., 2005; Dietz & Muir Wood, 2007; Turan et al., 2009; C. J. Lee et al., 2012; C.-C. Tsai et al., 2016; Tabatabaiefar, 2016; Alaie & Chenari, 2018). These kinds of tests can be conducted at 1-g or n-g, where the latter can also reproduce real in-situ confinement pressures.

Pitilakis et al. (2008) performed numerical simulations on DSSI based on physical model tests identifying significant increases on damping. The influence of stratification of the soils on DSSI was studied by Rayhani and El Naggar (2012), concluding that the structural response was greatly influenced by the soil stratification and soil-structure interaction.

Turan et al. (2013) studied the influence of the geometric ratio on the dynamic interaction of embedment stories. They found that the frequency of models tends to approach a fixed-base condition by increasing embedment depth while damping ratio is not influenced by the basement depth. Hokmabadi et al. (2014) investigated the seismic response of buildings with pile foundation and shallow foundation by means of numerical and physical modeling. Both methods demonstrate that the use of pile foundation reduce the amplification of lateral displacements on the structure compared to the case of shallow foundation. Zhang et al. (2017) analyzed the damping characteristics of DSSI for two multi-story building models. They conclude that classical damping characteristics can be assumed for the soil and the structure when subjected to small motions.

As shown above, most of the previous research on the effect of embedment on DSSI focused in analytical or computational modeling and very few experimental results are available. In addition, most of them focus on the effects of the dynamic response of the superstructure with limited analysis of the dynamic interaction itself. Indeed, there is a very limited information about the dynamic pressure distribution on the walls at basement levels. On the other hand, as the cost of land is increasingly in urban environments, it is more and more common the increase of the number of undergrounds and therefore there is a need to advance in the understanding of DSSI in these configurations. The work presented in this paper takes advantage of the recent development of the transparent laminar box to advance in the understanding of the phenomenon, allowing probably for the first time to visualize continuously in space and time what happens in the soil because of this dynamic interaction, which is the major contribution of the work.

3.2 Experimental set-up

The experimental set-up includes a transparent laminar box, a shaking table, a series of sensors, and different techniques of data acquisition, which are described in the following sections. The model is composed by a small-scale building and a sandy soil foundation. The different building models used in these tests are based on real design of shear-wall buildings with several undergrounds stories (prototypes). All tests are designed to evaluate the nonlinear soil response including its interaction with the embedded levels of the structure in a controlled 1-g environment.

3.2.1 Transparent Laminar Box

The main advantage of laminar containers is their lateral flexibility, which allow the container compatibility with the strain of the soil at the boundary. These laminae are generally assembled allowing horizontal free sliding, i.e., the lateral boundary meet the kinematic condition of a shear beam, simulating a free field condition.

The laminar container used in this experiment (Figure 3-1) has a transparent front side. This feature allows the visualization of the soil particles, allowing the computation of the soil displacement field directly through the glass. The box comprises nine light weight fiber-glass rings. The inner dimensions of the box are 1000 mm x 500 mm x 960 mm (length x width x height). To prevent the escape of sand particles, rubber rounds are placed at the corners in contact between the rings and the glass. More detail about the functioning of the container and verifications performed can be found in Segaline et al. (2021).

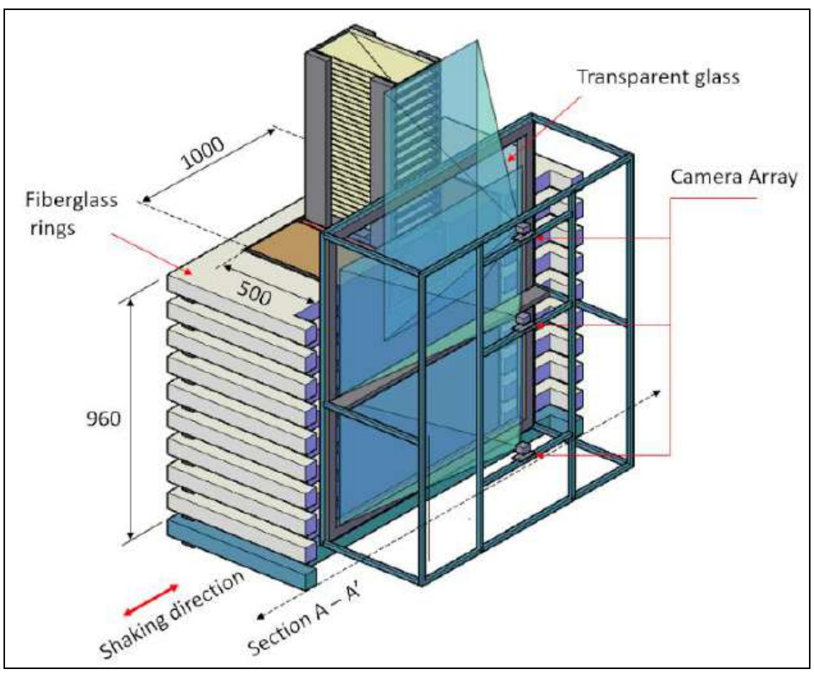

Figure 3-1: Laminar box and Image acquisition scheme

3.2.2 Prototype and Similitude laws

In small-scale modeling, the prototype and the model are related through a series of scaling factors, which is the ratio between the prototype physical property and the model corresponding property (e.g., length, material modulus, etc.). A series of scaling factors are defined in the literature for different properties, however, due to small-scale restrictions, it is usually impossible to simultaneously comply with all the scaling factors. For this reason, depending on the model objective, only the relevant physical properties shall be properly scaled.

In this study, prototype cases are defined from realistic shear-wall buildings, considering their fundamental period of vibration, geometry, stiffness and mass. The reduced scaled models were built with suitable materials to preserve the most relevant characteristics of the prototypes, but not all the variables can be preserved. According to Moncarz & Krawinkler (1981), these level of compliance with different parameters is divided into true, adequate and distorted models. Further works, such as Iai (1989), focused on compilating similarity rules of scaling parameters including length, mass and time. Besides, many DSSI researches developed through physical modeling in shaking table are based on these rules (e.g., Meymand, 1998; Pitilakis et al., 2008; Turan et al., 2013). The scaling relationships used in this work are summarized in Table 3-1.

Table 3-1: Scaling factors after Iai (1989)

Length	λ	Mass	λ^3	Time	$\lambda^{1/2}$
Force	λ^3	Mass density	1	Frequency	$\lambda^{-1/2}$
Stiffness	λ^2	Acceleration	1	Shear wave velocity	$\lambda^{1/2}$
Stress	λ	Strain	1	Modulus	λ

The physical models are divided into two groups; the first group correspond to mid-rise buildings (MB) and the second to high-rise buildings (HB), both cases represent 4-story and 15-story buildings, respectively. Each group has three combinations of embedded levels classified by the codes: 0B, 2B, and 4B (i.e., number of basement levels). The detailed configuration and dimensions of all models are presented in Figure 3-2.

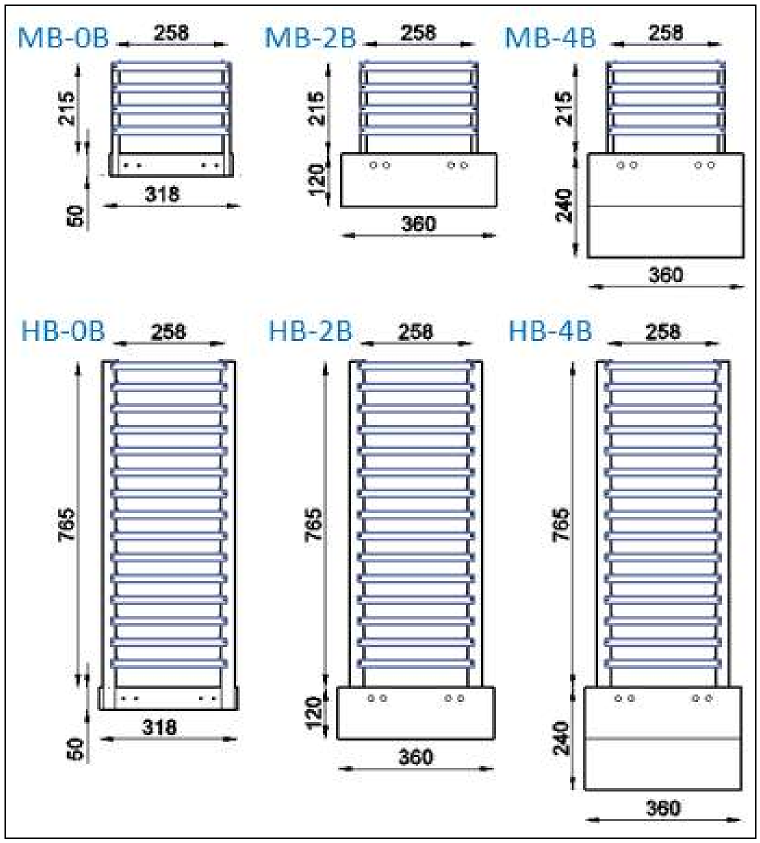

Figure 3-2: Physical Models used in shaking table tests. (Dimensions in millimeters)

The materials used for models were selected to preserve main physical properties described in Table 3-2. The slabs are made from AI-304 steel, taking advantage of its lightness and mass. On the other hand, the walls are made from polyvinyl chloride (PVC) due to its flexibility; while the underground levels were made using A-36 steel to obtain rigid walls in comparison to the soil and the superstructure. The fundamental fixed base-period of each model was adjusted using as reference empirical relations from real buildings of similar dynamic characteristics.

According to Soto et al., 2020, the fundamental elastic period of reinforced shear wall buildings can be estimated as the ratio between the number of levels and a constant equal to 20. For example, for the case HB-4B, 15 stories of the superstructure and 4 underground stories gives an approximate value of T = 0.95s. The scale factor used in this work correspond to $\lambda = 50$.

In the scaled models, the buildings lateral flexibility is given by the PVC walls, and their natural period of vibration was measured by free-vibration tests. The PVC material, and its geometry, provided a good match between the model natural period and the target prototype natural period using the empirical relationship from Soto et al., 2020. All the model and prototype parameters are summarized in Table 3-2.

Table 3-2: Scaling relationships for $\lambda = 50$

Case	Superstructure density (kg/m^3)		Basement density (kg/m^3)		Height Superstructure (m)		Height Basement (m)		Natural Period T (s)		
	Prototype	**Model**	**Prototype**	**Model**	**Prototype**	**Model**	**Prototype**	**Model**	**Prototype**	**Model (target)**	**Model* (empirical)**
MB-0B	400	400	433	433	10.75	0.215	-	-	0.2	0.03	0.03
MB-2B	400	400	433	433	10.75	0.215	6	0.12	0.3	0.04	0.08
MB-4B	400	400	433	433	10.75	0.215	12	0.24	0.4	0.06	0.10
HB-0B	400	400	433	433	38.25	0.765	-	-	0.75	0.11	0.12
HB-2B	400	400	433	433	38.25	0.765	6	0.12	0.85	0.12	0.17
HB-4B	400	400	433	433	38.25	0.765	12	0.24	0.95	0.13	0.16

* The scaled natural period for models was adjusted according to the prototype, however it could vary slightly

The soil used for the tests is a poorly graded sand without fines, classified as SP according to Unified Soil Classification System. This sand is characterized by mean particle size (D_{50}) of about 1 mm. After the placement in the container by ten layers with uniform compaction, the density inside the container was about 1.62 gr/cm^3 verified with a nuclear density gauge, which corresponds to a relative density of 70%. By measuring the ambient vibrations, it was verified that the average shear wave propagation velocity of the material, prior to the installation of the buildings, was approximately 60 m/s. Additional details of the soil properties are available in Segaline et al., 2021.

3.2.3 Shaking table tests

The shaking table used for these experiments was designed by ANCO Engineers Inc. It has one degree of freedom and can reach a maximum acceleration of 1-g. Its operational stroke range oscillates ± 450 mm (Figure 3-3). This shaking table can introduce horizontal motion at frequencies up to 15 Hz. The considered input motions are described in Table 3-3. Ricker wavelets were selected as input motions, to have a wide frequency range with a short test duration. The periods and amplitudes of Wavelets 2 to 4 were selected to reasonably match the spectral ordinates of the available rock records in Chile for the 2010 Maule (Mw 8.8) earthquake in the vibration range of the models according to Table 3-2. Only for Wavelet 1, an exceptionally high amplitude was selected for exploratory purposes of system performance.

Figure 3-3: Laminar box placed at the ANCO shaking table

Table 3-3: Summary of Ricker wavelet base motions

Wavelet	Input amplitude (g)	Frequency (Hz)	Assembly System
1	0.65	2.3	Shallow foundation SSI
2	0.20	3.4	Embedded and Shallow foundation SSI
3	0.20	5.0	Embedded and Shallow foundation SSI
4	0.20	7.0	Embedded and Shallow foundation SSI

3.2.4 DIC and data acquisition

The acquisition of images is based on a camera array (Figure 3-1). Each camera is located at the same distance from the objective but at different elevations, to capture the entire width and height of the model front side (soil and superstructure). The cameras were set to capture 60 frames per second (fps) at a resolution of 4k (i.e., 3840 x 2160 pixels) for all tests. The foundation soil has a high color-contrast of its particles, to facilitate the observation their displacements. The front side of structures was prepared with different color patterns to reach a reasonable correlation coefficient between pictures during image processing. Careful selection of adequate lighting conditions were required.

To analyze the front side of the basement, two strips of polyurethane foam were included at the contact between the basement structure and the transparent side of the laminar box, with the objective to prevent sand seepage (Figure 3-5b). Finally, the DIC analysis was conducted with the software MatchID® (Lava & Debruyne, 2010) using a subset size of 21 pixels and a step-size of 10 pixels.

The data acquisition was complemented with accelerometers distributed both on the soil and on the structure (Figure 3-6). Additionally, one accelerometer was placed at the base of shaking table to control and verify the effective input signals imposed by the shaking table.

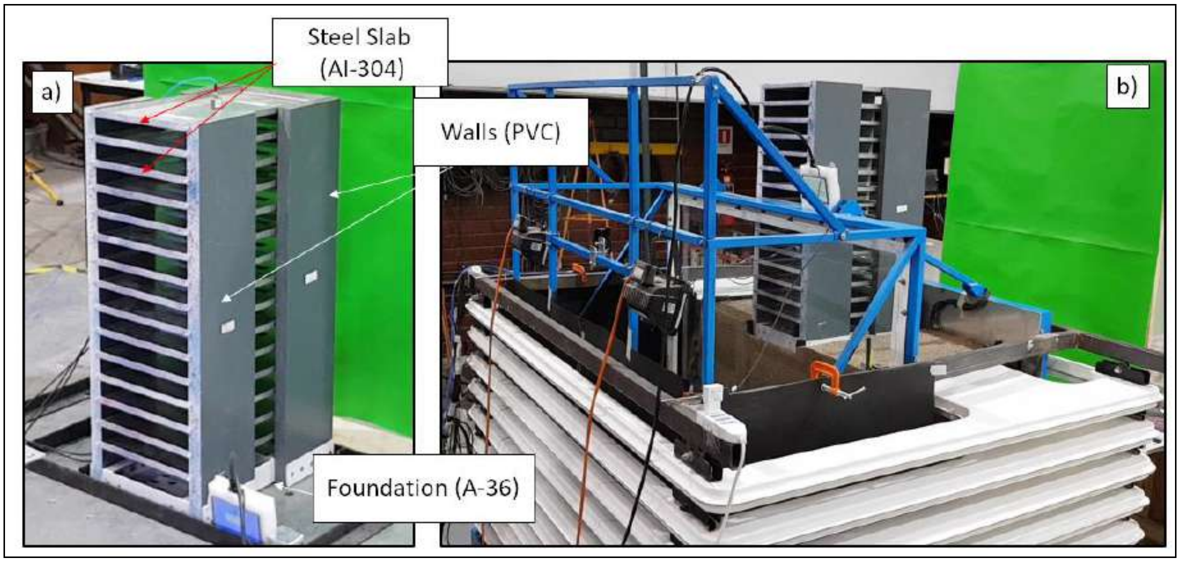

Figure 3-4: Physical model HB-0B: (a) fixed base and (b) flexible base.

3.2.5 Pressure mapping

The tactile pressure sensor consists of a sheet of highly sensitive piezoelectric cells distributed in length and width. For the HB-2B case there is an effective measuring area of 12 cm x 42 cm corresponding to 504 sensels, while for the HB-4B case, there are 1008 active sensels. The sensor used for this application was PMS-5315 from TekScan® (Figure 3-5a). This sensor covers the lateral wall of the basements. During the motion, a sampling rate of 100 Hz was acquired.

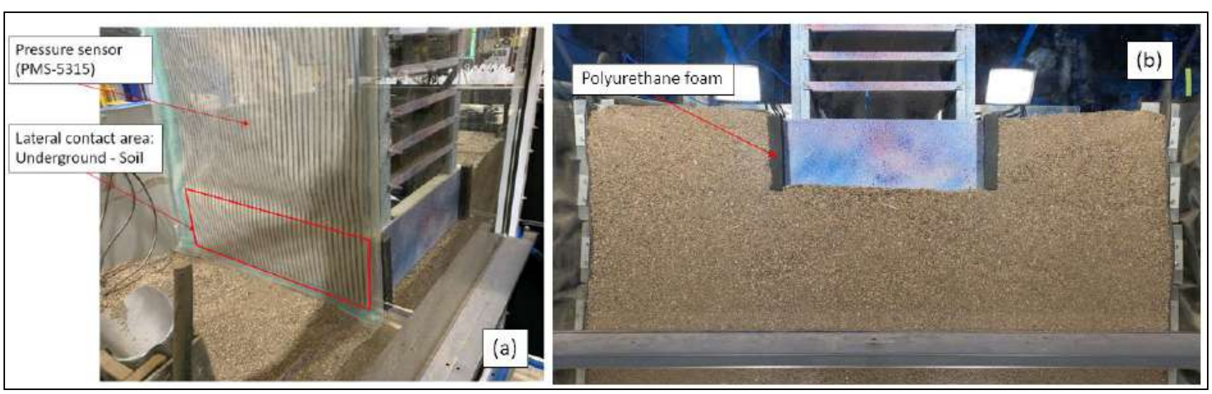

Figure 3-5: (a) Location of pressure sensor (PMS-5315) and active contact area; (b) example of final configuration for testing (HB-2B case)

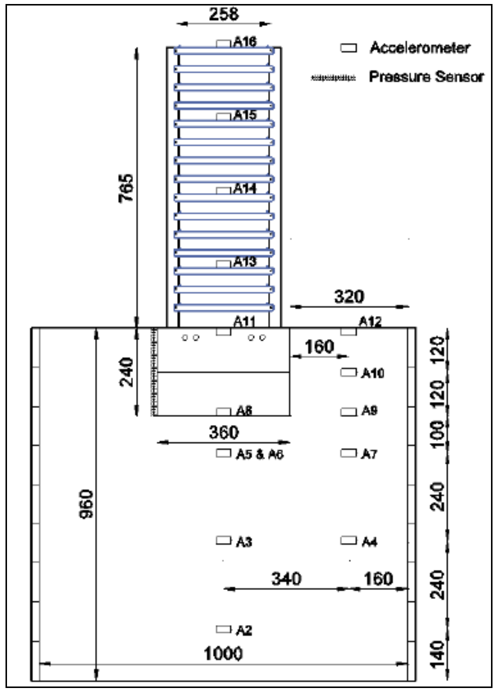

Figure 3-6: Acquisition data set

3.3 Results and discussion

3.3.1 Soil displacement analysis by DIC

The nonlinear soil-structure interaction during the motion is analyzed using the DIC technique, including the displacement fields of the soil and the movement of the structure. Taking advantage of the continuous view provided by the transparent laminar box, it is possible to track soil movements during the loading, a key aspect to evaluate the kinematic interaction effect on DSSI.

3.3.1.1 Effect of the ground confinement induced by the building self-weight

The model representing a high-rise building with shallow foundation (i.e., HB-0B) was considered to analyze the effect of the building self-weight in the behavior of the foundation soil. A time window between 0.8 s and 1.0 s of the input signal (Wavelet 1) was selected for DIC process (Figure 3-7a). The total displacement field, horizontal and vertical, from the processing of 12 images in this time interval is shown in Figure 3-7b. As the stiffness of the granular soil increases with confinement, areas that are heavily loaded by the building weight are stiffer and therefore show smaller displacements than areas outside of the building influence area, at the same depth and for the same dynamic loading. This effect explains the conical shape of the instantaneous displacement fields.

Note that far from the building (free field), a pattern tends to be slightly more horizontal, indicating a uniform displacement at the same depth. Depending on the time step, free-field displacements can be up to 20% larger in comparison to the motion below the foundation.

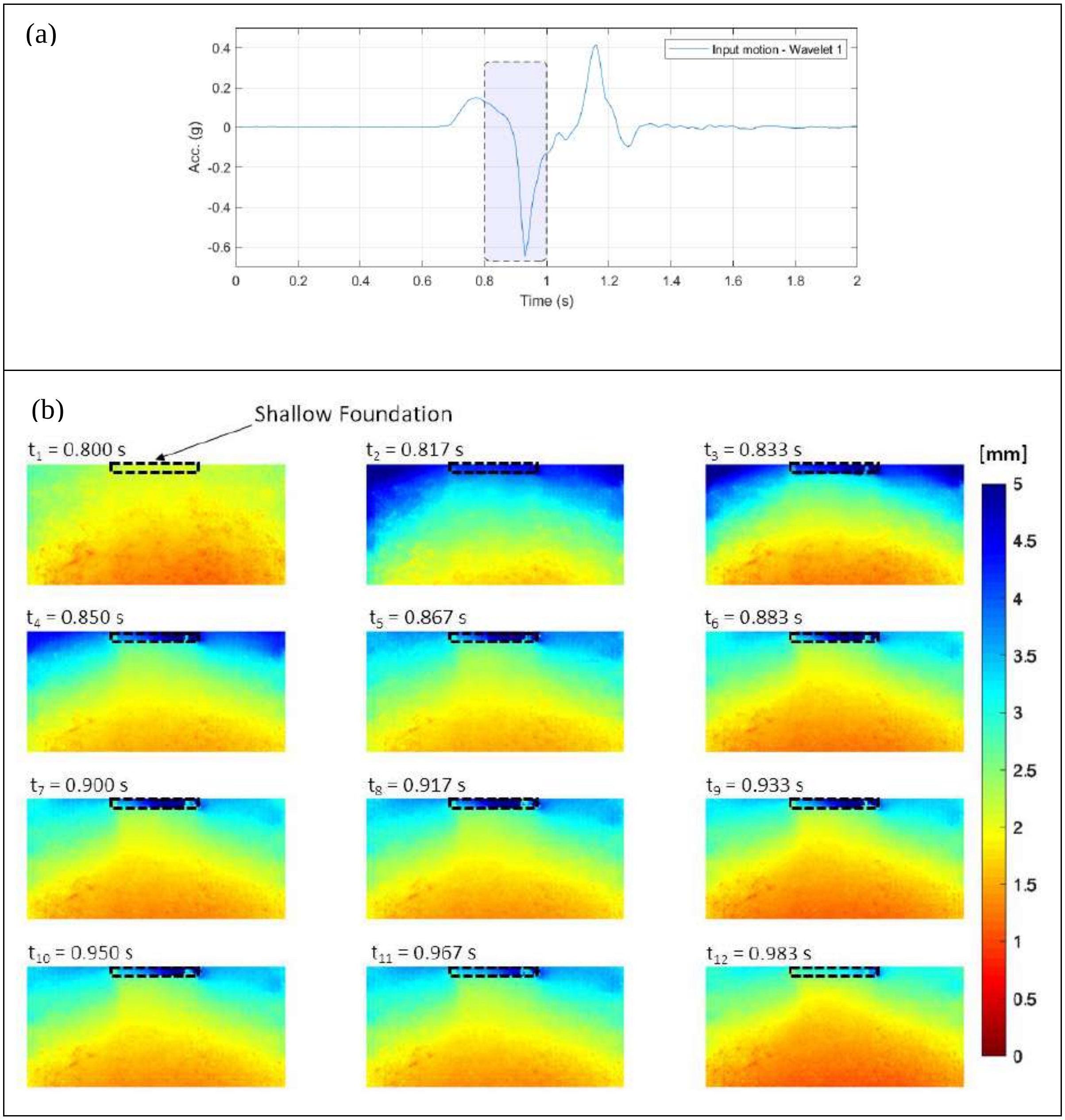

Figure 3-7: (a) Ricker signal used as Wavelet 1; (b) Total soil displacement inferred by DIC (Wavelet 1)

3.3.1.2 Lateral interaction and boundary effects

To illustrate the lateral interaction between the embedded part of the building and the lateral soil we selected the model HB-2B, i.e., with 2 underground levels. Figure 3-8a shows a profile of horizontal soil displacements, at four different distances from the basement wall, as a function of embedment depth H. All the profiles in Figure 3-8 correspond to the time t_0=0.43s of Wavelet 3 shown in Figure 3-10a. Blue line indicates the displacement of the soil in contact with the wall, showing a monotonic reduction in amplitude with depth, it can be noted that there is no separation between soil particles and the scaled building, which is one of the main conditions for simulating small-scale models (Iai, 1989), while profiles located at H/2 and H show a change in curvature. We will discuss below in the paper that this observation is related to the rocking of the superstructure. At 2H the profile shows again a monotonic reduction in depth. Near the edges of this region, the kinematics are strongly controlled by the boundary conditions: a large stiffness discontinuity near the building and shear-beam like kinematics at the boundary of the box. Between these two boundaries, the lateral deformation is more complex and could be associated with a higher frequency content resulting from wave reflection at these edges. Additionally, it can be noted that the displacement at 120 mm depth (H) is approximately the same in all profiles, therefore the lateral interaction effects reach approximately the embedment depth. Moreover, as seen in Figure 3-8b, the shear deformations are in the range ±0.1% indicating that the role of soil nonlinear stress-strain behavior plays a significant role.

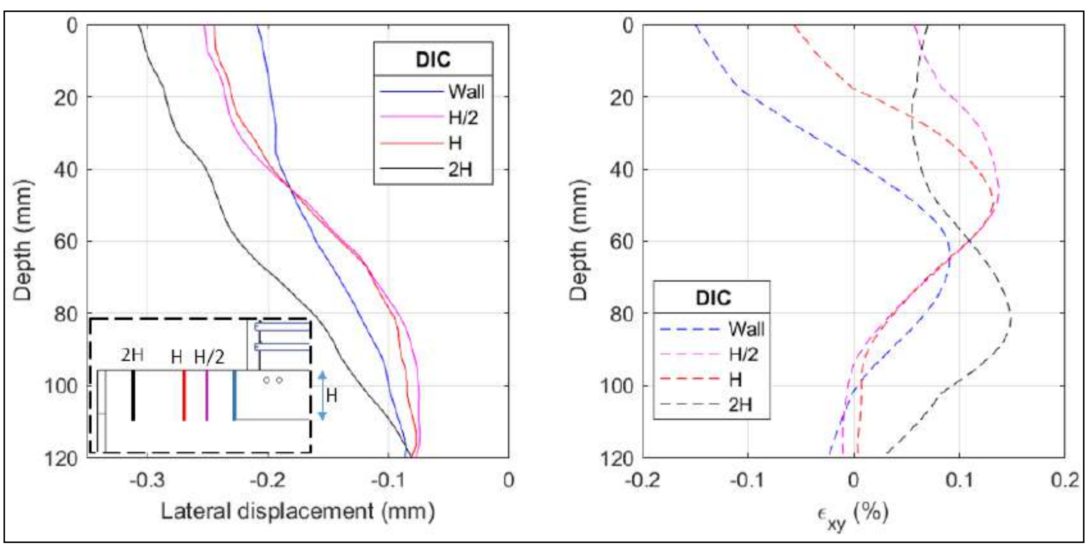

(a) (b)

Figure 3-8: Lateral displacement and shear strain for t_0

3.3.1.3 Kinematic interaction effects inferred by DIC

To isolate kinematic interaction, the input amplitude was fixed at 0.2g and only its predominant frequency was modified between 3.4 to 7 Hz. (Wavelets 2, 3 and 4 in Table 3-3). Each test was repeated 3 times modifying the number of underground levels (i.e., HB-0B, HB-2B and HB-4B).

The lack of compatibility of motion due the discontinuity of stiffness between the soil and the structure is one of the main characteristics on DSSI analysis. This interaction is shown for high-rise buildings in Figure 3-9b, Figure 3-10b-c, and Figure 3-11b in terms of horizontal displacements fields at four time steps at the beginning of the motion. In these figures, the instant at which the motion reaches the free field and the foundation level can be visualized.

In general terms, for all cases of the shallow foundations (HB-0B) the displacements below the building are mainly horizontal (horizontal arrows in the figures) and only near the edges of the box or very close to the surface, significant vertical components are observed (this effect is more evident in Figure 3-11a). In the case of the lowest frequency (Wavelet 2 in Figure 3-9) no major differences are observed between the HB-0B and HB-2B cases. However, when the frequency of the motion increases (Wavelet 3 in Figure 3-10 and 4 in Figure 3-11), the incompatibility of stiffnesses and the impact on the motion on the lateral soil become much more evident. In the case of HB-4B of Wavelet 3 and 4 the effect is much more significant, and it is very clear how the combined effect of lateral displacement and rocking of the building compresses and decompresses the lateral soil from one side and the other, modifying the soil response between each side of the building. The latter effect is linked to inertial rather than kinematic interaction. This effect is especially evident for Wavelet 3 and 4, probably because their frequency ranges are much closer to that of the fixed-base building (6.25 Hz according to Table 3-2).

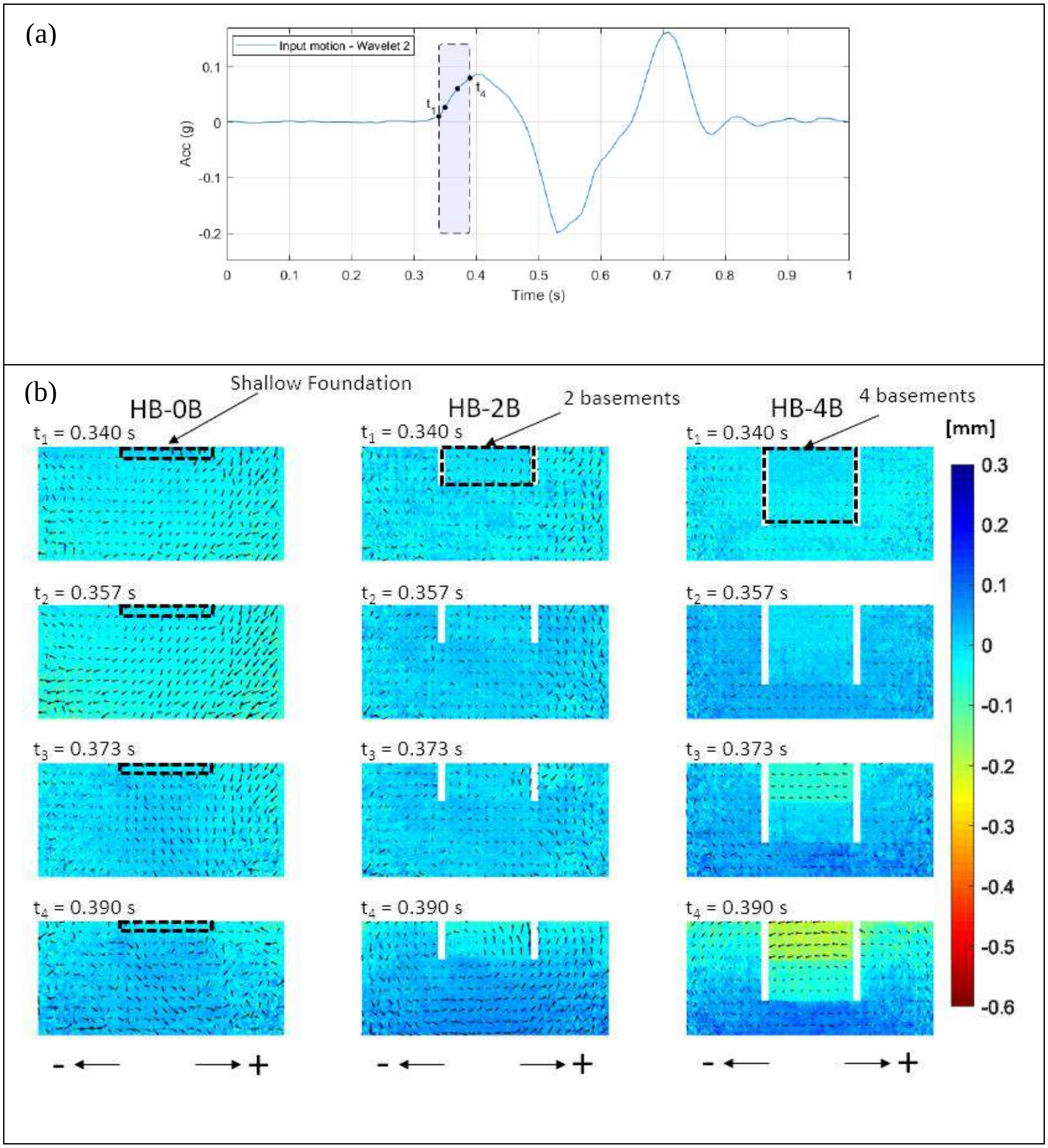

Figure 3-9: (a) Ricker signal used as Wavelet 2; (b) Horizontal displacement inferred by DIC in HB cases (Wavelet 2). Arrows indicate direction and magnitude in relative terms

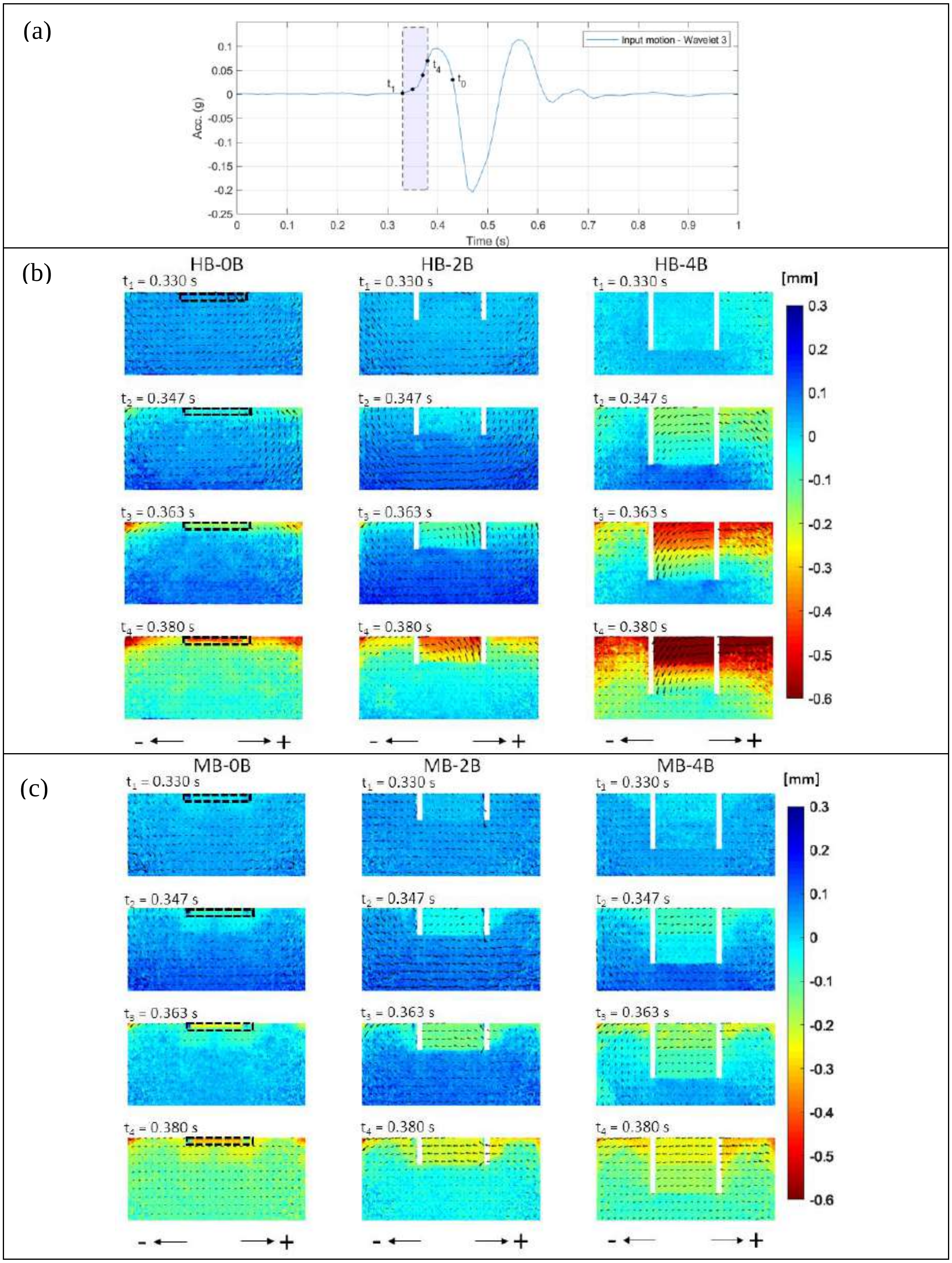

Figure 3-10: (a) Ricker signal used as Wavelet 3; (b) Horizontal displacement inferred by DIC in HB cases (Wavelet 3); (c) Horizontal displacement inferred by DIC in MB cases (Wavelet 3).

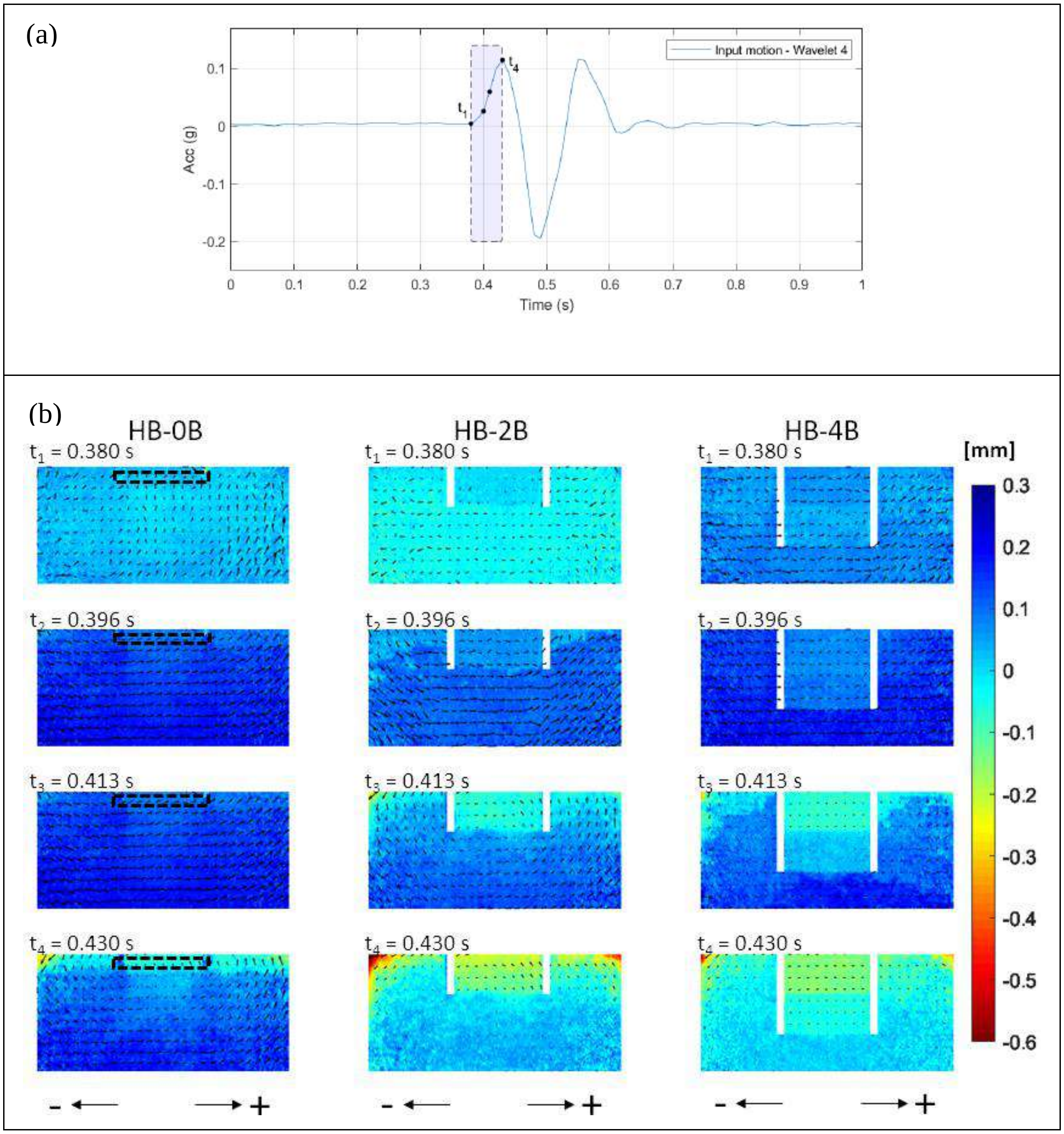

Figure 3-11: (a) Ricker signal used as Wavelet 4; (b) Horizontal displacement inferred by DIC in HB cases (Wavelet 4). Arrows indicate direction and magnitude in relative terms

In addition, the surface response was recorded at the control point CP 2 located in the middle between the basement walls and the boundary of the soil container (Figure 3-12). Depending on the input considered and the number of basement levels, the motion at the surface control point can be up to three times larger than the recorded below the building, due to the waves generated by the oscillation of the building and because the soil beneath the building is more confined and therefore more rigid. In terms of residual lateral displacements at the surface control point, the inputs associated to lower frequencies (Figure 3-13a and Figure 3-14a) are the ones that generate the maximum values, reaching up to 0.7 mm, while with higher frequency inputs (Figure 3-15a), these residual displacements are negligible.

The trend of the influence of the number of undergrounds levels in the observed displacements at controls points is not straightforward, as for example for Wavelet 2, the maximum influence is obtained for HB-2B (which is very similar to HB-0B), while for Wavelet 3, the maximum variation is reached for the building founded at greater depth (HB-4B). Since the superstructures of the three cases are identical, the differences in the observed displacements should have an origin mainly in kinematic effects, related to the wavelengths of the waves generated by the lateral interaction between the buildings and the soil.

Comparing the lateral motion at the base of HB-0B against its corresponding control point (base v/s CP 2), it is observed that the maximum values and the difference in the first peak of the motion tends to reduce as the frequency content of the input increases. After the first peak, more significant differences appear that can possibly be attributed to the inertial interaction due to the vibration of the building when the loading direction is reversed.

In the case of buildings with basements (HB-2B and HB-4B) the comparison between the control point and motion at the building base is more complex because of the combined effect of the increased confinement, the interaction of the foundation in terms of motion compatibility and the vibrations transferred from the superstructure to the ground. According to our results, this combination of effects produces an invariable reduction in effective base motion, suggesting that neglecting the effects of DSSI would be a conservative assumption.

In terms of frequency content, Figure 3-13b, Figure 3-14b and Figure 3-15b show the response spectra of the motions recorded at the base and at surface control point for each case. In general, these spectra show the main period of the input considered. Only in some cases, the vibration period of the tested building can be identified. For example, for the Wavelet 2 (Figure 3-13) of a mean period equal to 0.29s, a second peak close to 0.1s is observed, which is compatible with that of the scaled building (0.12s according to Table 3-2). The period associated with this peak increases slightly as the number of undergrounds increases, but it is not a significant change. When the period of the input is closer to that of the building (Wavelets 3 and 4), this second peak disappears because it is combined with the higher peak associated with the main frequency of the motion. It can be concluded that the motion at the base and at free field is influenced by the vibration of the building (inertial interaction), but this is a second order effect as the motion is dominated by the characteristics of the input. It can be noticed that in all these figures a smooth peak appears in the range 0.05-0.06s which is possibly related the vibration period of the soil in the box. Indeed, the elastic vibration period of the same soil without the building is about 0.066s (Segaline et al., 2021). Because the additional weight imposed by the building, we expect a shorter value in the tested configuration.

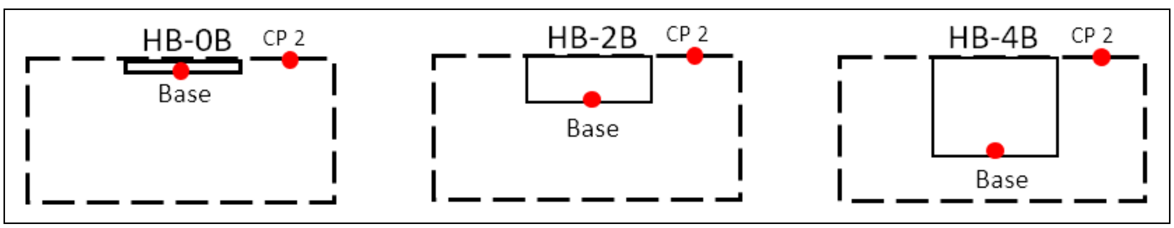

Figure 3-12: Distribution of control points (CP) on models

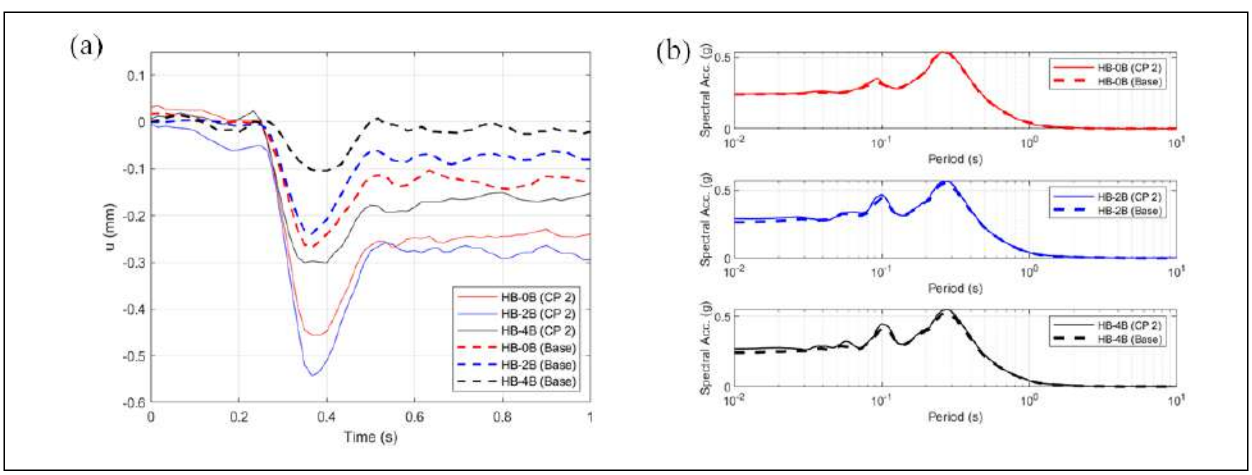

Figure 3-13: Response at surface control point CP 2, and under the base of building for Wavelet 2

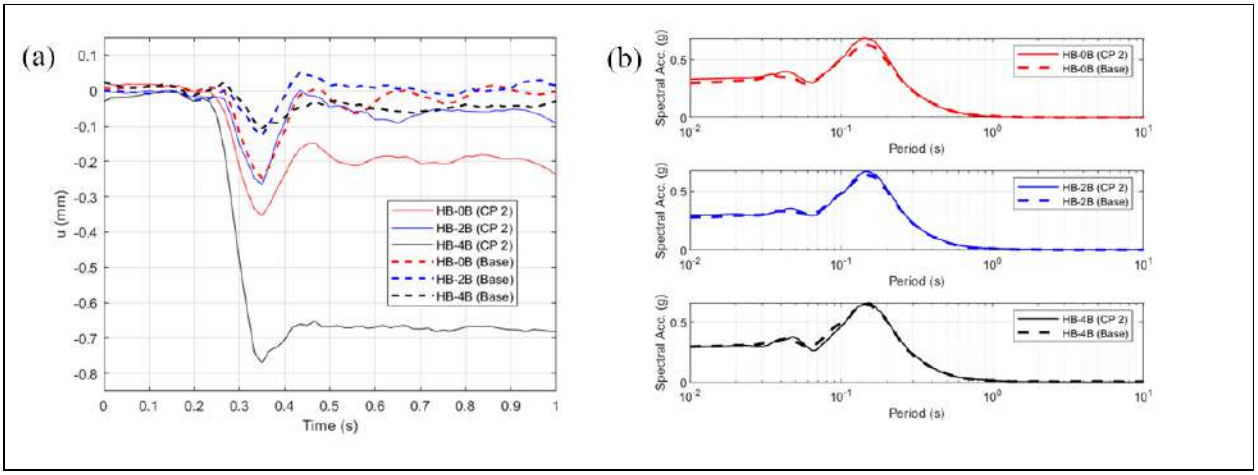

Figure 3-14: Response at surface control point CP 2, and under the base of building for Wavelet 3

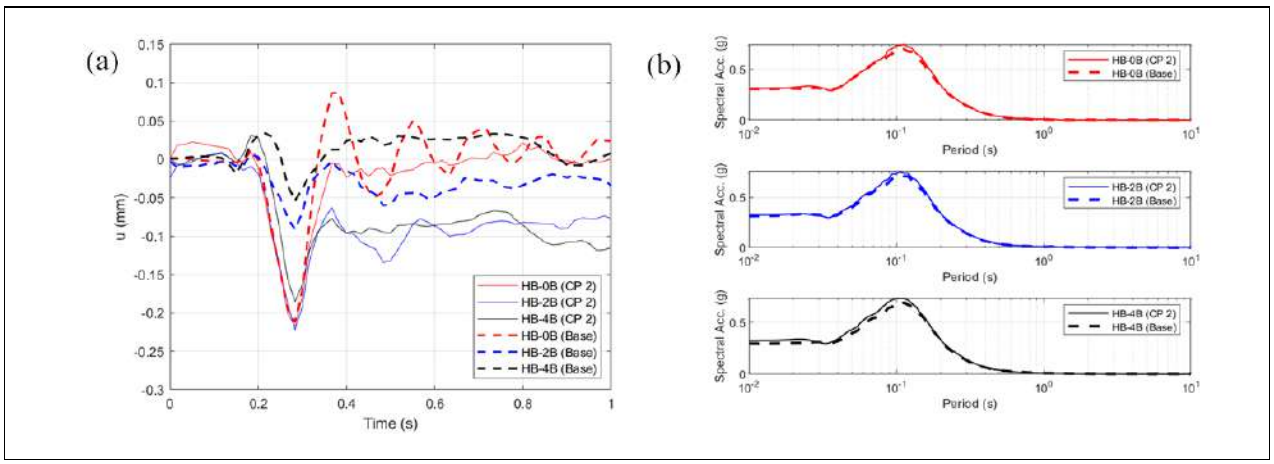

Figure 3-15: Response at surface control point CP 2, and under the base of building for Wavelet 4

3.3.2 Building response by DIC

The response of the buildings superstructure was evaluated for Wavelets 2, 3 and 4. As example, Figure 3-16 shows the horizontal relative displacement for DSSI system from DIC application. Both fields (i.e., superstructure and soil-structure) are analyzed separately because of the differences in displacements amplitude. In this figure, left color bar refers to soil-structure domain, while right color bar indicates the displacement scale of the building. From these results, the influence of the vibration of the building on the surrounding soil can be observed. For example, the difference in horizontal displacement between the underground portion of the building and the lateral soil can be noted. At t_1=0.330s the motion starts, and both the ground and the building have a very small displacement. At t_3=0.363s, the roof of the building has a negative displacement of about -4 mm (from right to left), while the soil wave is still arriving, imposing a positive displacement (from left to right) of about 0.3mm. At t_8=0.447s, the building roof starts a positive displacement with respect to the initial position, while the floor is already being loaded in the opposite direction (from right to left) with respect to the initial position. Finally, at t_{12}=0.513, the last cycle of the motion begins, and the system is in a position very similar to that indicated at t_1, with a close to zero displacement both at soil level and in the superstructure. It is verified that the experimental system allows to track in detail the dynamic interaction between the soil and the building, obtaining details of both the deformation of the building and the compliance between the underground and the surrounding soil.

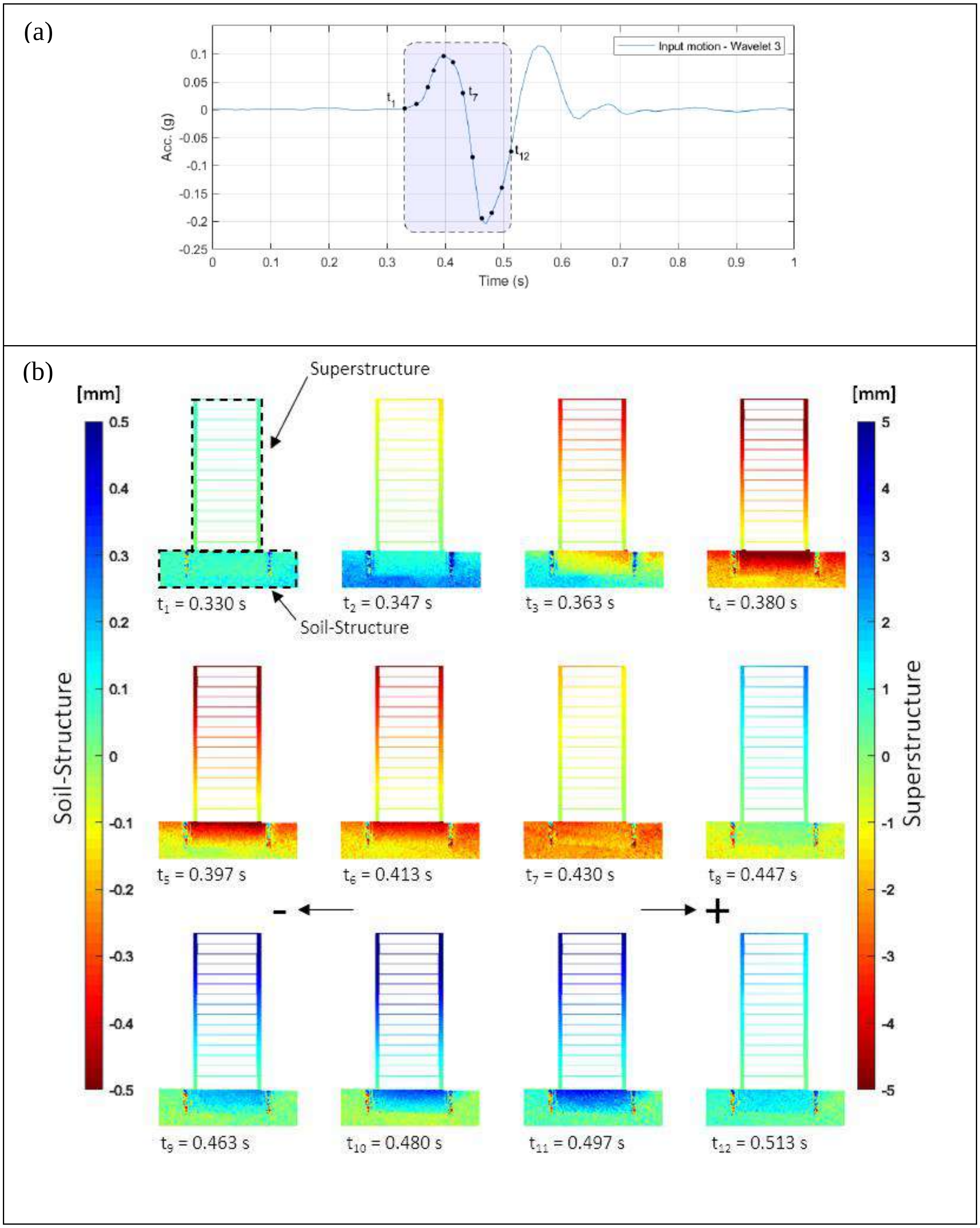

Figure 3-16: (a) Ricker signal used as Wavelet 3; (b) Horizontal displacement field of Building HB-2B inferred by DIC (Wavelet 3)

Employing continuous monitoring of motion-induced building displacement, the response of high-rise models with different undergrounds levels and subjected to three input motions are compared in Figure 3-17. At the beginning of the motion, the displacement of the buildings is very similar. However, depending on the frequency content of the input, the displacements in each case change in amplitude and lose phase due to the different embedment depth and lateral interaction. In general, there is no significant impact of embedment depth on roof displacement, obtaining similar maximum values. The only case where a greater impact can be noted is for the HB-4B case, where a greater displacement appears from the first loading cycle and a residual displacement of about 2 mm is observed. Indeed, as can be seen in Figure 3-10b, starting at 0.38s, a right-to-left rocking of building appears, with horizontal displacements in the buried portion up to 0.6mm. This large lateral movement causes a residual rotation of the superstructure inducing a permanent roof horizontal displacement. For convenience, Figure 3-18 extends the series of horizontal ground displacements to 0.647s. From these figures it can be concluded that even though the motion in the roof changes its direction, the deformation of the buried portion remains rotated which explains the change in response with respect to the HB-0B and HB-2B cases for the same input. Then, the dynamic lateral thrust of the soil plays a key role in the roof response.

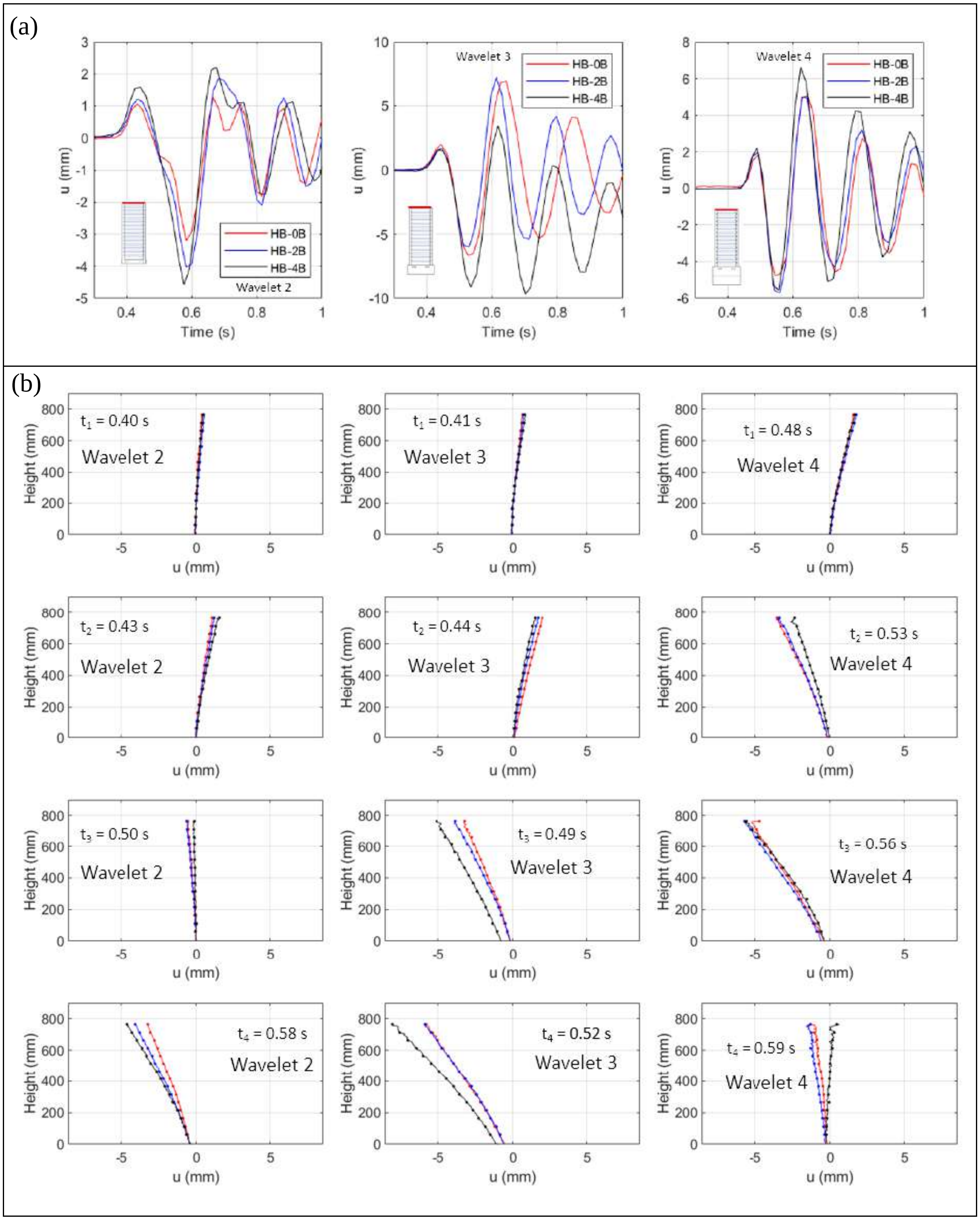

Figure 3-17: (a) Displacement of the 15th floor for Wavelet 2, 3 and 4; (b) Comparison of displacement between High-rise models inferred by DIC

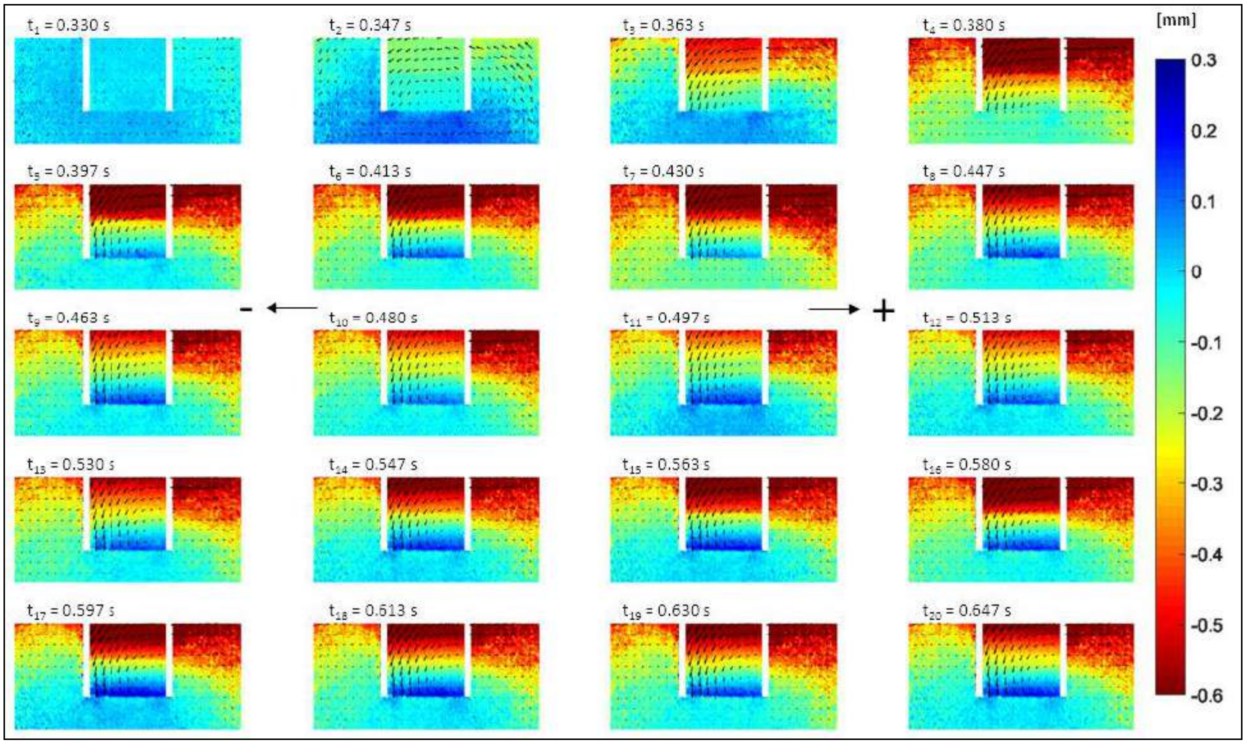

Figure 3-18: Horizontal displacement of HB-4B for Wavelet 3

3.3.3 Correlation between rocking and lateral thrust

Figure 3-19 to Figure 3-21 show the rocking of the building foundation for HB-2B and MB-2B cases, computed from DIC and the lateral thrust from the tactile sensor. Since the deformations of the tall building are of larger amplitude, the foundation rotations are better captured by DIC, and noisier records are obtained for the low building. In general terms, it can be observed that the peak of negative rocking (clockwise rotation) coincides very well with the minimum of the seismic thrust. In this case, the reduction of lateral confinement of the soil located at left side of the underground reduces the horizontal stresses with respect to the static value. The behavior at positive rotation (counterclockwise) is more erratic, since in some cases it also coincides with the maximum increase in seismic pressure due to kinematic compatibility (HB-2B for wavelet 3 and 4), but in the other cases the correlation is not so clear. The reason is that the signals were polarized to force the first significant rotation of the building to be clockwise (negative), while the second was counterclockwise (positive). Thus, the second rocking is more contaminated by the dynamic effects of the test (inertial effects, refracted waves, permanent soil deformations, etc.) and are more difficult to interpret. It is interesting to note that in all tests, static equilibrium is reached at about 1.8s, i.e., 1 second after the end of the stronger part of the motion, which shows that the system is still re-equilibrating while the building stops oscillating.

In relation to the absolute values of the thrusts, the inertial effect of the building is significant and variations of 2 to 4 times greater can be seen for the tall building versus the lower one. The effect of the frequency content of the signal under consideration can also be clearly observed. In the case of the lowest frequency motion (Wavelet 2 of 3.4 Hz) a reduction of the force is invariably obtained with respect to the static case on the monitored side. In the case of higher frequency inputs (Wavelet 3 and 4), a more effective loading of the tall building is initiated as they approach their natural frequency, and the pressures rise and fall with respect to the static value during the dynamic loading. Since the lower building has a much higher natural frequency than the considered motions, the thrust reduction follows the same trend with a slight reduction of the minimum value as loading frequency increases. It is concluded that in the cases studied, the dynamic effect on lateral soil thrust is dominated by the vibration triggered in the superstructure.

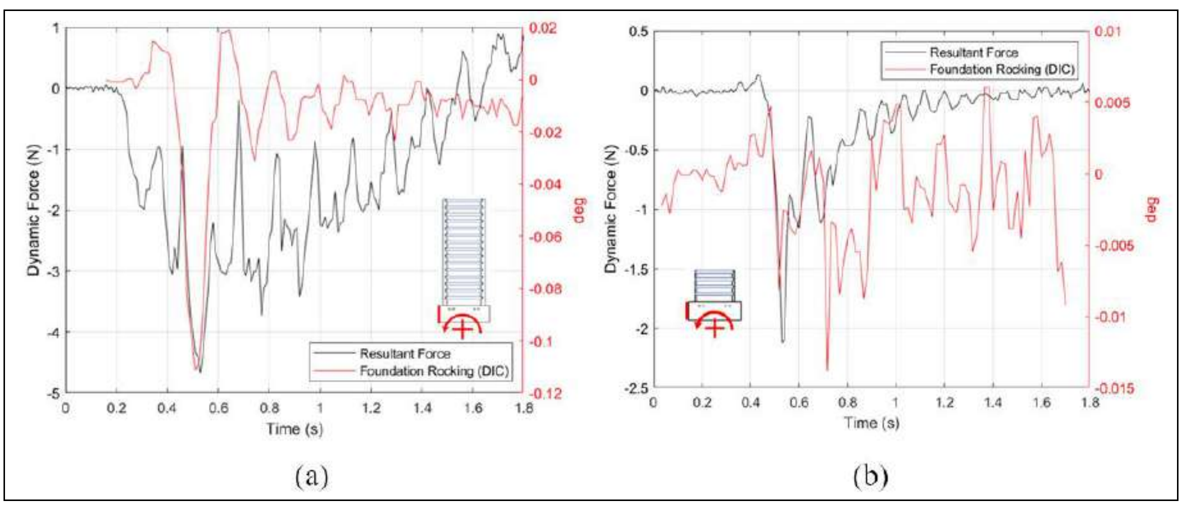

Figure 3-19: Measured force and rocking HB-2B (left) and MB-2B (right) (Wavelet 2)

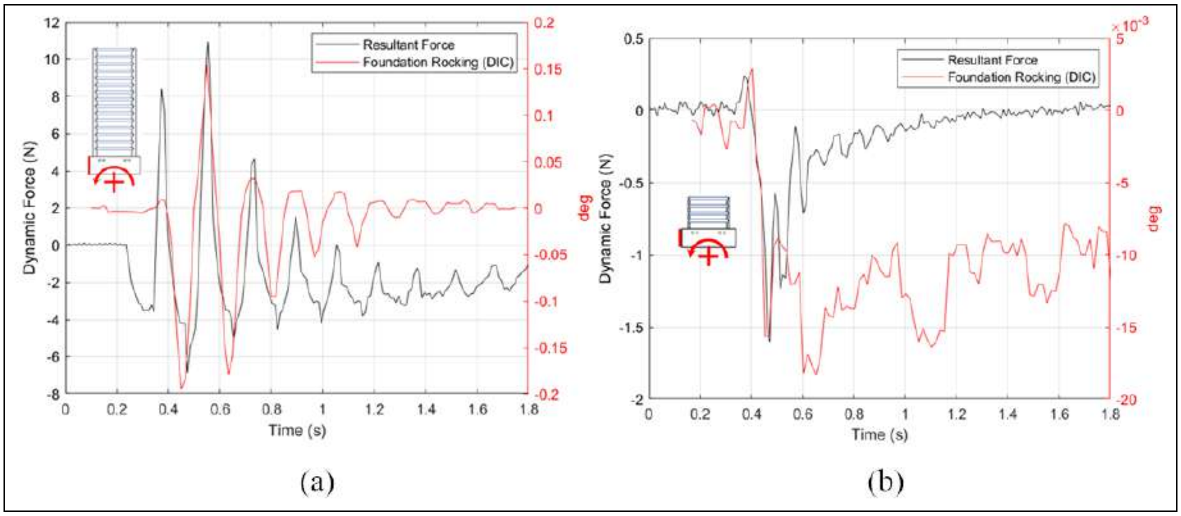

Figure 3-20: Measured force and rocking HB-2B (left) and MB-2B (right) (Wavelet 3)

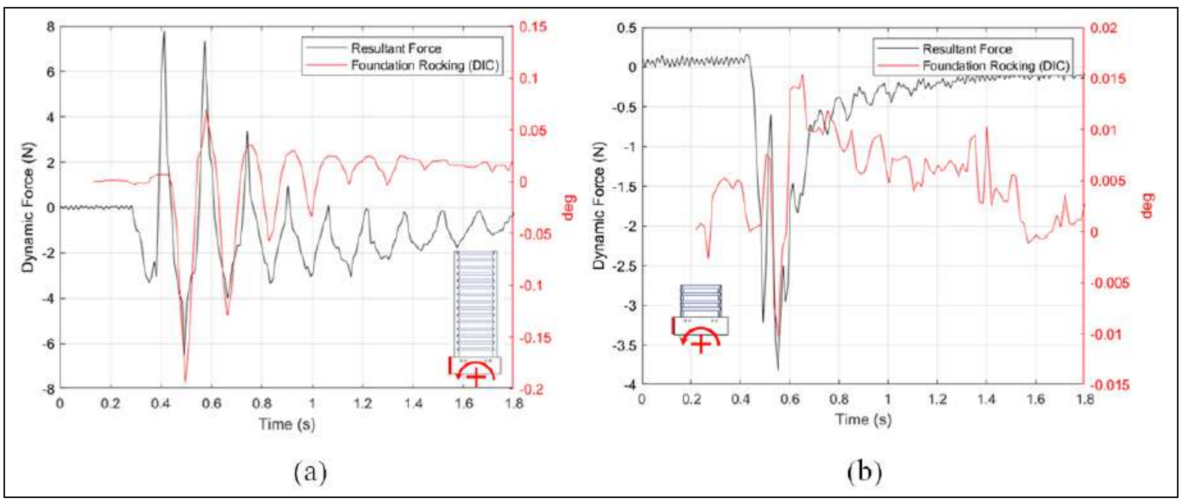

Figure 3-21: Measured force and rocking HB-2B (left) and MB-2B (right) (Wavelet 4)

3.3.4 Dynamic pressure distribution on basement walls

The dynamic pressure distribution was analyzed for the High-rise Buildings (HB) and the Mid-rise Buildings (MB). Figure 3-22 shows the dynamic pressures on 2-level basement (left panel) and 4-level basement (right panel). For the latter, an inflection point is observed almost at the same depth around 0.1 m despite the frequency content of the input. This is probably caused by the rocking of foundation and inertial forces from building vibration. In the case of the higher frequency motion (Wavelet 4), only for one of the instants a shallow inflection point is observed, which could be caused by the higher frequency waves (shorter wavelength) propagating in the soil. However, the lateral thrust is far from being uniform a distribution that is often used for the design of buried walls. In the HB-2B case, the distribution for low frequencies (longer wavelength) is like an inverted triangle. However, as the frequency increases, the center of gravity of the dynamic increase rises (Wavelet 3) and for Wavelet 4 an inflection point appears.

On the other hand, for 4-story building (lower model) and for the case of 4 basements (MB-4B), the dynamic pressure distribution tends to be more uniform and could be idealized as trapezoidal for low-frequency cases (Wavelet 2 and 3), as presented in Figure 3-23. For the highest frequency case, it approaches a triangular distribution. In the case of the two undergrounds, the distribution is also roughly trapezoidal for Wavelet 2 and 3, while for Wavelet 4 it looks triangular.

While there are differences in the maximum values of the thrusts when the input frequency is changed, they generally remain in the same order of magnitude. If the building and the number of undergrounds is maintained, the greatest impact of the input frequency is observed in the distribution of pressures. By changing only the building, for example comparing HB-4B and MB-4B for Wavelet 2, both the effect on the shape and values of the thrusts are observed, indicating that the inertial interaction plays a key role in the distribution and magnitude of the lateral thrusts. This effect is interesting, since in practice the estimation of lateral thrusts is limited to considering the soil properties and intensity of the movement without including the characteristics of the superstructure.

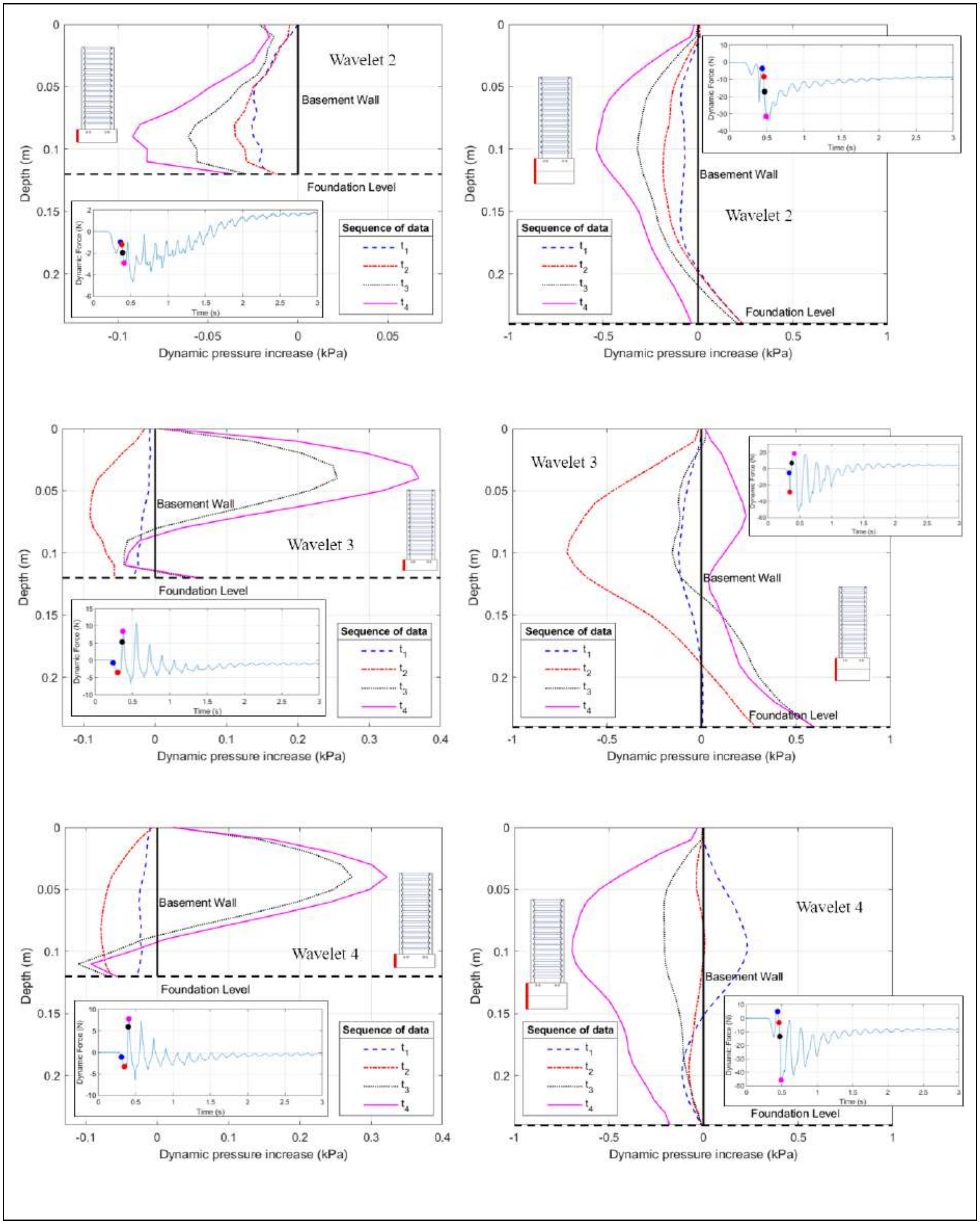

Figure 3-22: Dynamic pressure distribution on walls for High-rise Building cases: HB-2B and HB-4B

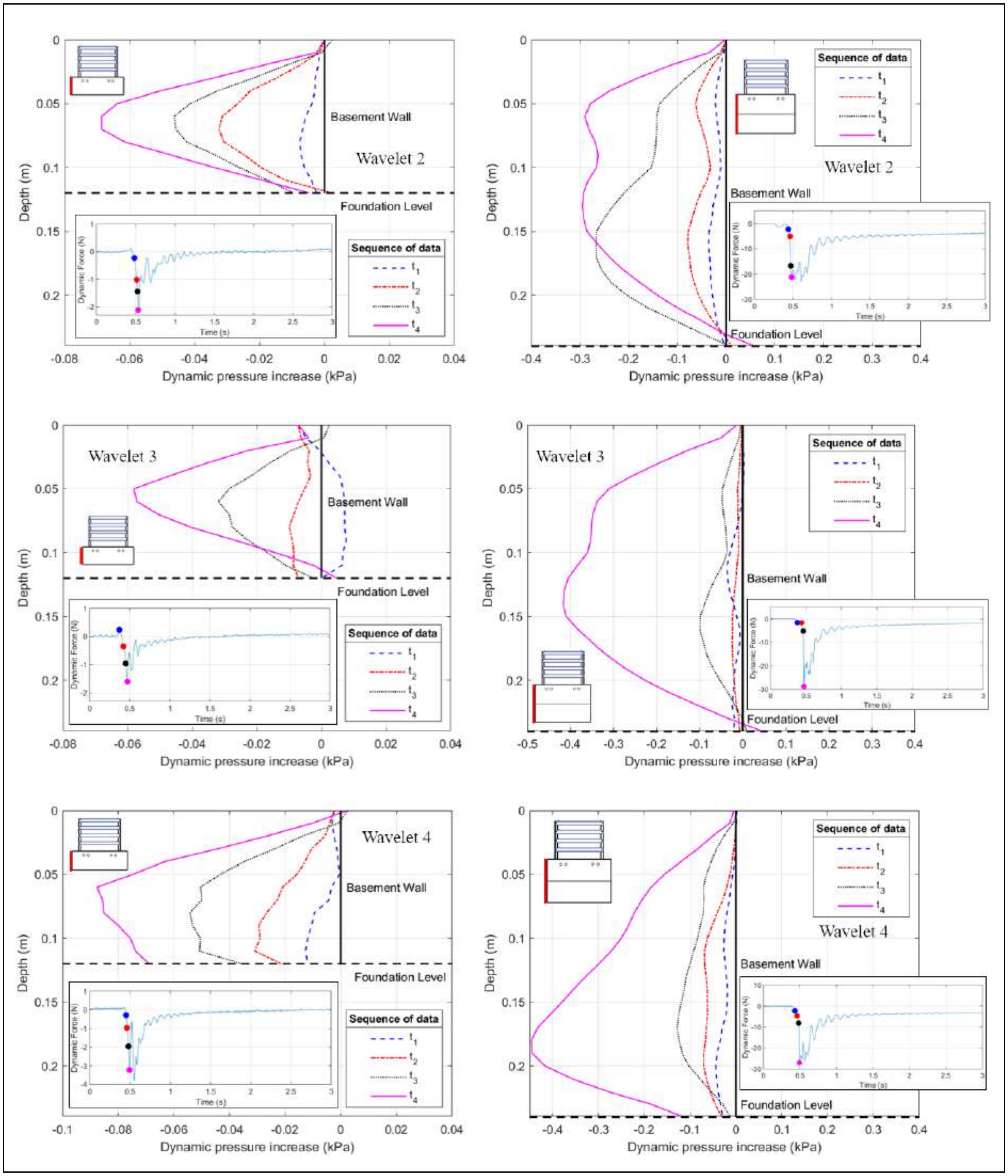

Figure 3-23: Dynamic pressure distribution on walls for Mid-rise Building cases: MB-2B and MB-4B

3.4 Conclusions

Physical tests were performed in a laminar box, in conjunction with the digital image correlation technique and dynamic pressure distribution, to evaluate the DSSI. Six small-scale physical models were studied, representing a building with underground stories and variable foundation embedment depth. The main conclusions are listed below:

Two general conclusions can be drawn:

1. The tests results show that the building`s inertial movement has an influence in the dynamic pressure acting on the basement walls. This physical phenomenon should also occur in full scale buildings, but it is not currently included in design codes or considered in engineering practice. Further research is needed in this topic.

2. The small-scale physical testing proved the usefulness of the transparent laminar box and the DIC technique, along with advanced sensors, such as the tactile pressure sensor. This allows further insight in the dynamic behavior of soils, and soil-structure interaction.

Additionally, the following conclusions are based on specific laboratory testing results:

1. It was possible to verify the effect of foundation soil confinement on the dynamic response of a building for the shallow foundation case (HB-0B) where a pattern of reduced movement is observed due to the overload imposed by the structure, this pattern extends conically in depth.

2. The images acquired thanks to the transparency of the laminar box open an outstanding opportunity to evaluate the continuous field of interaction between soil and structure. It is found that the lateral interaction effects reach approximately the embedment depth and, it was also shown how the rocking of the building compresses and decompresses the lateral soil from one side and the other, modifying the soil response between each side of the underground levels. The latter effect is linked to inertial rather than kinematic interaction. Additionally, we found that the motion at the base and at surface control point is influenced by the vibration of the building (inertial interaction), but this is a second order

effect as the motion is dominated by the characteristics of the input. In general, there is no significant impact of embedment depth on roof displacement, obtaining similar maximum values.

3. In the case of buildings with basements the comparison between the control point and motion at the building base is complex because of the combined effect of the increased confinement, the interaction of the foundation in terms of motion compatibility and the vibrations transferred from the superstructure to the ground. According to our results, this combination of effects produces an invariable reduction in effective base motion, suggesting that neglecting the effects of DSSI would be a conservative assumption.

4. It was possible to efficiently capture the shape of the dynamic distribution of pressures on the underground walls, in addition to the possibility of relating its behavior to the monitoring of images. We found that the dynamic effect on lateral soil thrust is dominated by the vibration triggered in the superstructure. Consequently, the inertial interaction plays a key role in the distribution and magnitude of the lateral thrusts. This result could have practical implications, since in general the estimation of lateral thrusts is limited to considering the soil properties and intensity of the movement without including the characteristics of the superstructure.

4. DYNAMIC PRESSURES AND SOIL DISPLACEMENT ASSESSMENT IN RIGID PARTIALLY EMBEDDED CANTILEVER RETAINING WALLS USING A TRANSPARENT LAMINAR BOX

4.1 Introduction

Design of soil retaining systems is one of the main branches in geotechnical engineering, particularly in seismic zones, where the dynamic earth pressures can vary significantly from the static case. Retaining walls (RW) are typically designed based on pseudo-static equilibrium considerations, and a small to moderate wall movement due to seismic pressures is usually acceptable, as long as it does not induce damage to neighboring structures and the failure of the retaining system.

The dynamic earth pressure on retaining systems began to acquire great attention in the 1920s after major earthquakes (e.g., the Great Kanto Earthquake, Japan, 1923). Mononobe (1929) and Okabe (1924) were the pioneers for the development of pseudo-static coefficients to modify the original Coulomb theory, and provided a first approach to assess the force induced by dynamic pressures acting on walls. From this initial work, significant research in relation to dynamic earth pressures in retaining systems, using either analytical, numerical or physical models, have been conducted for decades (e.g., Ichihara & Matsuzawa, 1973; Sherif et al., 1982, 1984; Bolton & Steedman, 1985; Ishibashi & Fang, 1987; Steedman & Zeng, 1990; Richards Jr et al., 1999; Geraili Mikola et al., 2016, among others). However, the use of the Mononobe-Okabe (M-O) method still prevails in international standards, e.g., NCHRP report (Anderson, 2008).

The study of retaining structures is normally divided into yielding and non-yielding walls, depending on the expected deformation of the soil-wall system. Yielding walls can slide or rotate, due to the partial or complete shear strength mobilization of the soil, and their stability is traditionally evaluated by means of the limit-equilibrium theory (Mononobe, 1929). In contrast, non-yielding walls are usually designed assuming a soil behavior close to linear elasticity (Sherif et al., 1984; J. H. Wood, 1975). Analytical expressions for dynamic earth pressures for non-yielding rigid and flexible retaining walls, under elasticity assumption, can be found in Veletsos & Younan (1994; 1997). Choudhury & Nimbalkar (2006) developed a pseudo-dynamic analysis to obtain an approximation to lateral earth pressure on yielding walls. They noted more realistic results due to the non-linear pressure distribution. Along with the limit-state theory, Mylonakis et al. (2007) proposed an alternative solution to the M-O method based on plasticity. Their analytical results showed good agreement compared to the numerical analysis, except for high accelerations. Bellezza (2014, 2015) developed a pseudo-dynamic method to calculate seismic earth pressures by modeling the backfill as a Kelvin-Voigt medium. The results showed that the active pressure distribution is strongly influenced by the horizontal acceleration and the angle of internal friction of the soil.

In relation to studies based on physical tests, in general, centrifuge tests are preferred because they preserve real in-situ stresses (Bolton, Britto, Powrie, & White, 1989; Bolton & Steedman, 1982, 1985; Ortiz et al., 1983). Steedman & Zeng (1990) proposed a pseudo-dynamic method based on the phase change of lateral acceleration. The results did not show large earth pressures increase compared to the pseudo-static method, however, a significant amplification in the lateral acceleration was observed. More recently, centrifuge experimental research has benefited from the improvements in the sensing systems of dynamic earth pressure (Dewoolkar et al., 2000; Mikola et al., 2016). However, these advances did not allow the description of the deformation pattern in the backfilled soil due to the discrete nature of the measurements at the location of the sensors. Dewoolkar et al. (2001) studied the seismic behavior of saturated cohesionless backfill. They found that the long-term residual thrust is directly proportional to wall flexibility for liquefiable soils. Nakamura (2006) evaluated the use of M-O method in gravity retaining walls; they conclude that the method did not represent the real behavior of the backfill according to experimental results. Al Atik & Sitar (2010) studied the distribution of the induced lateral earth pressure on cantilever walls; the results showed that the maximum dynamic earth pressures do not happen at the same time of the maximum inertial forces of the wall, therefore the M-O method could overestimate the results. Regarding partially embedded cantilever retaining walls, Conti et al. (2012) conducted centrifuge tests for propped and cantilevered cases. Because of the flexible behavior of the RW, permanent top displacements of up to 2% were recorded for the cantilever cases, and up to 1.5% for the propped cases. Afterwards, Conti & Viggiani (2013) proposed a new method of calculation based on the pseudo-static limit equilibrium. They concluded that the strength of the soil-wall system plays an important role on the wall displacements. This method was subsequently compared against a numerical analysis by Conti et al. (2015). They found that cantilever embedded walls achieve permanent displacements not necessarily when acceleration is at its maximum. Alternatively, models built in laminar containers subjected to 1-g have also been used to study foundations with micropile systems (Jalilian Mashhoud, Yin, Komak Panah, & Leung, 2020), inclined piles (Goit et al., 2021), DSSI problems such as the interaction with tunnels (Jiang, Chen, & Li, 2010), the case of buildings (Turan et al., 2013) or retaining systems. Wilson & Elgamal (2015) studied lateral earth pressures on walls with dense sand backfill. They concluded that the non-consideration of cohesion in the M-O method over-predicts the lateral forces. Latha & Krishna (2008) evaluated reinforced soil retaining walls. They noted the importance of backfill compaction to reduce damage in the wall, particularly for the case of higher accelerations. In some cases the geometric characteristics of retaining systems are modified, seeking additional benefits related to a better performance. Gao et al. (2017) studied the behavior of an anti-sliding retaining wall, as the horizontal degree of freedom is restricted, the rotation of the wall will be influenced by its own inertial force as the input base increases. Panah et al. (2015) studied soil reinforced retaining walls using polymeric strips. They demonstrated that the displacement of the wall can decrease up to 50% with the correct use of these reinforcements. Kloukinas et al. (2015) investigated seismic loads acting on cantilever walls; they observed that when the bending moment is maximum in the wall, the soil thrust does not depend on the active critical pressure.

Finally, computational models are a useful tool to verify or validate physical experimentation and analytical models. Green & Ebeling (2003) calibrated a numerical model to compute the dynamic behavior of cantilever RW. Psarropoulos et al. (2005) evaluated the seismic pressures of rigid and flexible walls by finite element models (FEM) models. They found that the M-O method also is able to generate a close enough approximation of the results of flexible systems. A similar analysis was also performed by Green et al. (2008) obtaining a good agreement between the M-O method and numerical models only for low accelerations. Additionally, they concluded that for high levels of acceleration, the M-O method underestimates the seismic earth pressures.

The literature review shows that, although detailed information on the dynamic behavior of retaining walls exists, there is still no unique relation between the distribution of seismic-induced dynamic pressures and yielding wall displacements. In addition, most of the theoretical and numerical research work needs experimental validation, as their link to case-histories is often scarce.

The present study includes the development of yielding retaining walls' physical 1-g models designed to continuously monitor the dynamic pressures and backfill movement, by means of a tactile sensor and the Digital Image Correlation (DIC) technique, respectively. The main objective is to correlate the motion of the soil and the wall with the dynamic pressures exerted on the retaining structure. With this purpose, three types of partially embedded cantilever retaining walls were analyzed, each one characterized by its height. These walls were subjected to Ricker wavelets with various frequency ranges and increasing acceleration amplitudes in conjunction with an appropriate scale factor.

4.2 Experimental set-up

All the tests were developed in a transparent laminar box mounted on a shaking table in a 1-g environment. The sensor system includes accelerometers distributed along the soil, a high-speed camera array equidistantly spaced from the front side of the box, and one tactile pressure sensor attached to both sides of the retaining wall. The experimental program considers three case studies based on prototypes. Each case is characterized by a different height of wall and embedment depth. In this way, it is possible to evaluate the influence of embedded portion of the cantilever wall in the overall performance of the retaining system.

4.2.1 Transparent Laminar box

The proper execution of small-scale dynamic tests in geotechnical engineering represents a great challenge. One of the major difficulties is related to the simulation of ground deformation due to propagation of seismic waves. The traditional way of solving this problem has been the use of laminar containers, characterized by having a lateral flexibility similar to the soil free field. Thus, boundary conditions imposed by the lateral sides mimic the kinematics of ground deformation to reduce the reflection of scattered waves.

In this investigation, a laminar container was used, with the special characteristic of a transparent front side (Figure 4-1). This feature allows visualization of the full field of soil displacement through a camera array. More details of the functioning of this laminar box can be found in Segaline et al. (2021). The same device and sensing techniques were used to study the dynamic behavior of non-yielding basement walls of buildings (Segaline et al., 2022), showing that the thrust acting on the non-yielding walls was strongly related with the building (superstructure) dynamic response. The present article focus on yielding cantilever walls in open excavations, without any building, under dynamic loading.

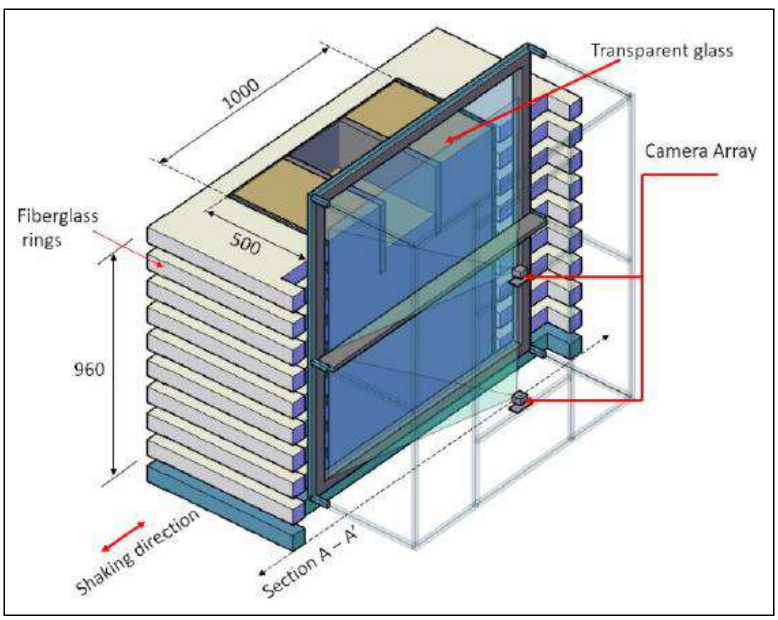

Figure 4-1: Laminar box: Isometric view (dimensions in mm).

4.2.2 Similitude laws

Acrylic plates were selected for modeling the retaining walls. This selection accomplishes most of the physical requirements needed to create the prototypes models. Since this experiment focused on soil-wall interaction, mass density and stiffness were the most important parameters for calibration. According to Goit et al. (2014), the acrylic material is suitable for a scaled retaining system experiment. The characteristic of this material allows the study of yielding walls due to the high stiffness contrast compared to the backfill soil. The physical models were scaled considering relationships of similitude developed by Iai (1989). All parameters are listed in Table 4-1, in terms of the scaling factor, η.

For this research, one of the main objectives was to preserve the dynamic characteristics between prototype and model; therefore, the ratio between the minimum wavelength (λ_{min}) and the height of wall (H) must be the same for both. Given this minimum wavelength, the maximum frequency is given by $f = Vs/\lambda_{min}$, where Vs is the shear wave velocity. A scale factor of η = 25 was selected given the size of the container, the stiffness of the materials and the capabilities of the shaking table.

Table 4-1: Scaling factors after Iai (1989)

Length	η	Mass	η^{3}	Time	$\eta^{1/2}$
Force	η^{3}	Mass density	1	Frequency	$\eta^{-1/2}$
Stiffness	η^{2}	Acceleration	1	Shear wave velocity	$\eta^{1/2}$
Stress	η	Strain	1	Modulus	η

To evaluate the influence of the height and embedment depth of the walls on their dynamic response, three cases were studied. These cases are identified as: RW-200, RW-250 and RW-325; the dimensions of each wall, together with all adopted values of the scaled parameters, are detailed in Table 4-2. The prototypes correspond to walls with a height between 5.0 m and 8.1 m, and an embedment depth between 1.75 m and 3 m. Figure 4-4 presents details of the model configuration.

Table 4-2: Scaling relationships for η = 25

Retaining wall parameter	**RW-200**			**RW-250**			**RW-325**		
	Prototype	**Model (Target)**	**Model* (Empirical)**	**Prototype**	**Model (Target)**	**Model* (Empirical)**	**Prototype**	**Model (Target)**	**Model* (Empirical)**
Young's modulus (GPa)	25	1	3	25	1	3	25	1	3
Density (t/m^3)	2.3	2.3	1.2	2.3	2.3	1.2	2.3	2.3	1.2
Height (m)	5	0.2	0.2	6.3	0.25	0.25	8.1	0.32	0.32
Thickness (m)	0.75	0.03	0.03	0.75	0.03	0.03	0.75	0.03	0.03
Embedded depth (m)	1.75	0.07	0.07	2.25	0.09	0.09	3	0.12	0.12

Soil parameter	**Prototype**	**Model**
Density (t/m^3)	1.7	1.7
Depth (m)	24	0.96
Shear wave velocity (m/s)	300	60

*The scaled model was adjusted to prototype values, however, it could have variations

4.2.3 Model preparation and retaining system configuration

A clean dry sand was used in this study, characterized by a high color contrast which is an important requirement for DIC. The soil was carefully placed into the container using the dry pluviation method to achieve a uniform density distribution of about 1700 kg/m^3, which corresponds to a Relative Density of DR = 70%. The retaining system is composed by two identical acrylic plates placed equidistant from the laminar boundaries. The tactile pressure sensor was glued to the backfill-side of the wall at the left side in Figure 4-2d. Both walls were fixed with a horizontal prop to ensure that no rotation or displacement occur during the dry pluviation. To prevent any leakage of sand from the walls backfill to the excavation, lubricated rubber bands were carefully installed in the contact between the lateral sides of the laminar box and the walls, ensuring a low friction sliding condition with the container. The configuration is symmetrical to compensate for static lateral thrusts on the rings of the laminar box. The sequence of installation is shown in Figure 4-2.

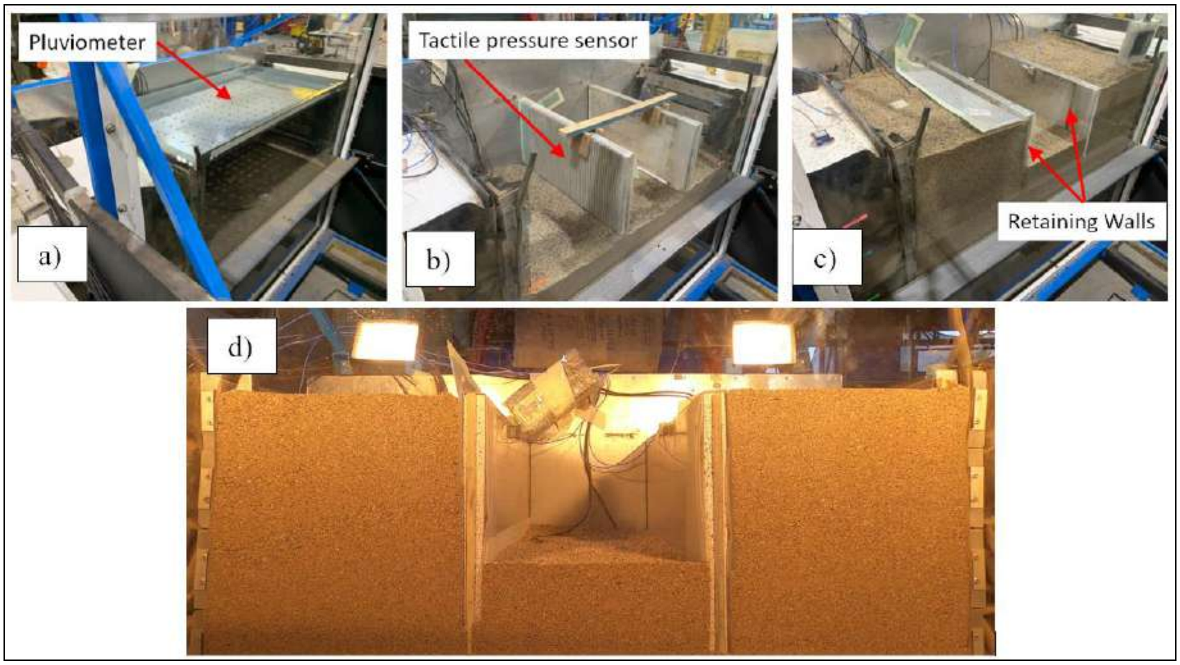

Figure 4-2: Installation of Retaining walls and pressure sensor: (a) Dry pluviation; (b) Tactile sensor; (c) Final configuration, isometric view; (d) Final configuration, camera 2

4.2.4 Shaking table tests

The one-directional shaking table used for this investigation has the ability to replicate seismic waves up to 1-g of acceleration under a payload of 1 ton. The base of the laminar container was fixed to the shaking table to avoid any slide during the tests. All the tests performed are described in Table 4-3; they were selected to preserve the ratio between the height of the wall (H) and the minimum wavelength of the prototypes λ_{min}/H=50, 40 & 30, respectively for RW-200, RW-250 & RW-325. Ricker wavelets (Figure 4-3) were used as input motion to allow a straightforward analysis of the dynamic pressures with the soil and wall motion. These figures show the motion imposed by the shaking table, recorded by the accelerometer located on the platform, so they differ somewhat from the theoretical inputs.

Table 4-3: Summary of Ricker wavelet base motions

Test code	Ricker Wavelet	Input amplitude (g)	Main Frequency (Hz)	Retaining Wall
E1	1	0.27	5.4	RW-200
E2	2	0.12	6.3	RW-200
E3	3	0.38	5.4	RW-200
E4	1	0.27	5.4	RW-250
E5	2	0.12	6.3	RW-250
E6	3	0.38	5.4	RW-250
E7	1	0.27	5.4	RW-325
E8	2	0.12	6.3	RW-325
E9	3	0.38	5.4	RW-325

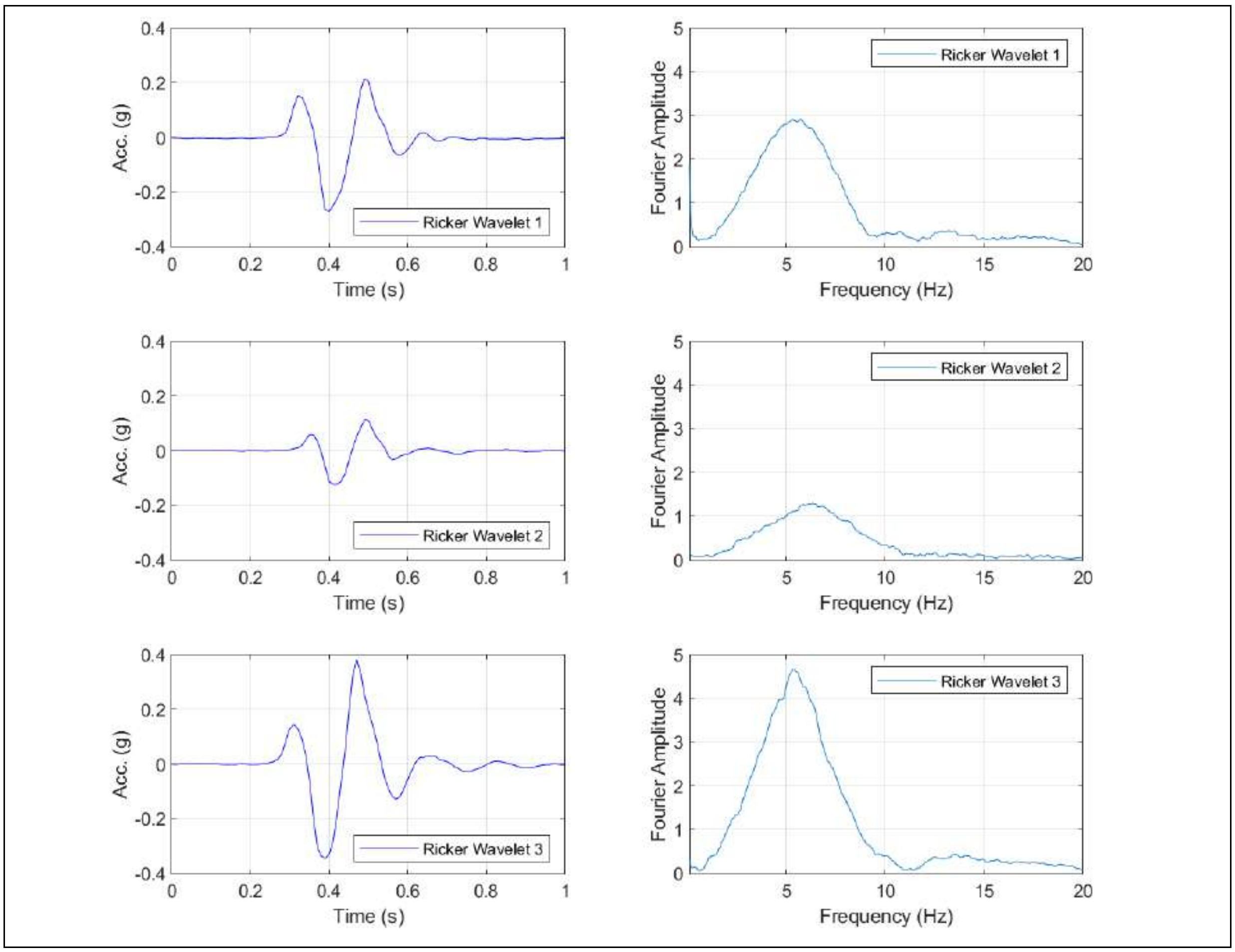

Figure 4-3: Ricker wavelet and Fourier amplitude

4.2.5 Data acquisition and instrumentation

The acquisition and instrumentation system consists of 14 uniaxial accelerometers placed in the soil and vertically distributed as presented in Figure 4-4, two high speed cameras (Figure 4-1) and the tactile sensor, to measure the dynamic pressure distribution of the soil acting on the left wall. The image acquisition was performed at a sampling rate of 60 Hz with 4k resolution (i.e., 3840 x 2160 pixels). Additionally, a lighting system was installed to have an optimal visualization of soil through the transparent glass and avoid shadows. Later, the analysis corresponding to DIC was developed with the software MatchID® (Lava & Debruyne, 2010), all images were processed with a subset size and step-size of 21 and 10 pixels, respectively.

The pressures mapping is acquired by a tactile sensor consisting of a matrix of sensitive piezoelectric cells (sensels), the sensor covers both sides of the left wall (active and passive areas). Table 4-4 summarizes the contact area and the total number of activated sensels for each wall during the tests. The sensor model used for this research was the PMS-5315 from Tekscan®. Finally, the sampling rate of pressure was 100 Hz.

Table 4-4: Pressure mapping acquisition

Retaining Wall	**Active area (cm^2)**	**Passive area (cm^2)**	**Total sensels**
RW-200	840	294	1134
RW-250	1050	378	1428
RW-325	1365	504	1869

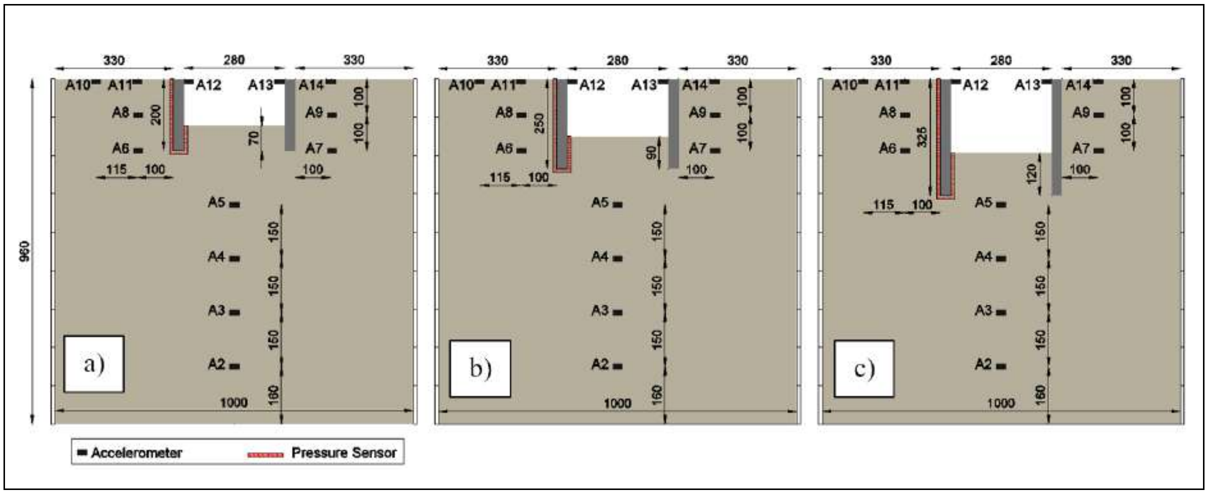

Figure 4-4: Cases of study: (a) Case 1, RW-200; (b) Case 2, RW-250; (c) Case 3, RW-325. All dimensions are in in millimeters

4.3 Numerical modeling

To have an independent basis for comparison against test measurements, a Finite Element model of each tested case was developed. The model was generated in Plaxis-2D® using as the constitutive model the HS-Small model (Benz, 2007) available in this software. Material parameters were calibrated using low confinement triaxial and Resonant Column tests (Figure 4-5). No volumetric strain was recorded since the tests were performed in dry sand. The calibrated parameters of the soil are presented in Table 4-5. The developed numerical model is shown in Figure 4-6. Lateral limits were modeled as tied boundaries to preserve a shear-beam like behavior. The lower boundary of the mesh was modeled as a compliant base, using a very high impedance contrast to replicate rigid boundary corresponding to steel surface of the shaking table. A small Rayleigh's damping of 1% was introduced to simulate the decay following the strong motion introduced by the shaking table. Finally, the retaining walls were modeled using elastic solid elements with appropriate acrylic parameters.

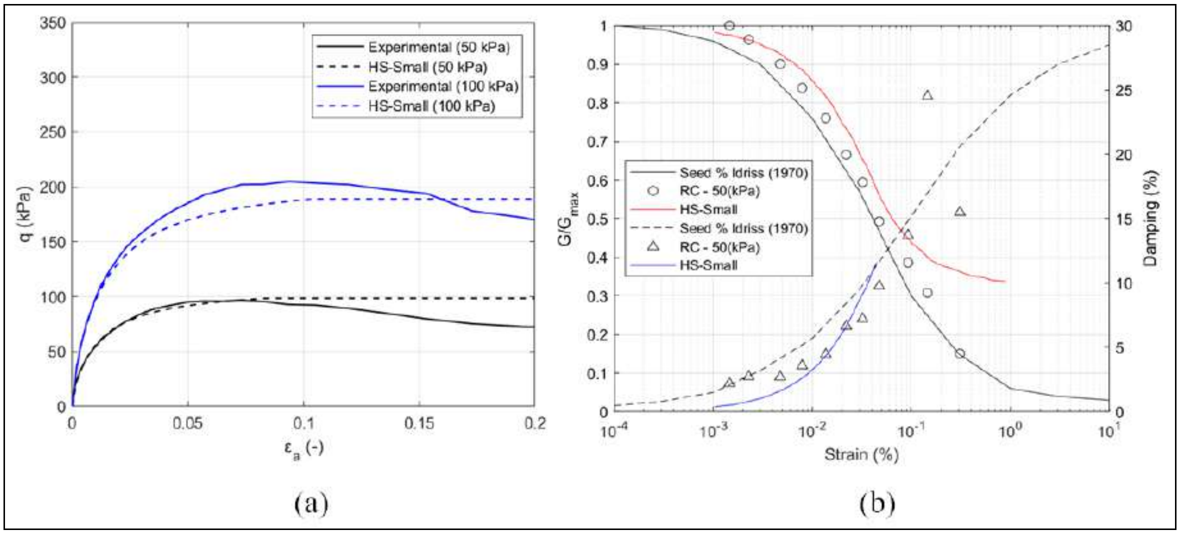

Figure 4-5: (a) Calibration curve for axial deformation and deviator stress (50 kPa and 100 kPa confinement); (b) Modulus reduction and damping curve from FEM calibration and resonant column tests (RC)

Table 4-5: HS-Small calibrated parameters

Parameter	**Unit**	**Value**
E_{50}^{ref}	(kN/m^2)	9502
E_{oed}^{ref}	(kN/m^2)	1.40E+04
E_{ur}^{ref}	(kN/m^2)	3.96E+04
$\boldsymbol{\varphi}$	deg	31
ψ	deg	0.23
$\gamma_{0.7}$	-	2.30E-04
G_0^{ref}	(kN/m^2)	5.00E+04

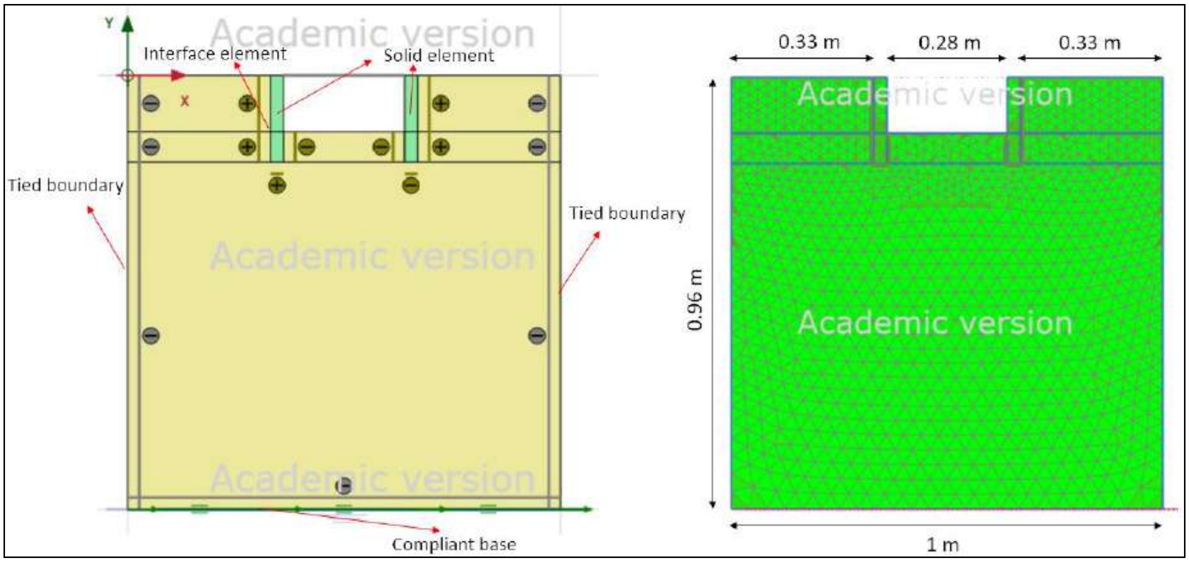

Figure 4-6: Retaining wall model, Plaxis 2D

4.4 Results

In this section, both static and dynamic results from physical tests are presented and discussed. In the static phase, the pressures recorded from the tactile sensor are compared with the computational model. In the dynamic phase, local measurements (accelerometers), and spatial measurements (tactile sensor and DIC) are compared against the FEM model. The emphasis of the analysis is to compare independent measurements and estimations from physical and numerical results to confirm data trends. Additionally, the DIC results are presented which aim to understand the overall performance of the system.

4.4.1 Static pressure distribution

The initial stress distribution measured by the tactile pressure sensor for the RW-200, RW250, RW-325 models, and the corresponding FEM results, are shown in Figure 4-7. Since each configuration was tested under the three Ricker wavelets inputs previously described, there are three independent static soil pressure measurements for each case. In general terms, an almost complete unloading of the upper half of the wall and a strong concentration of pressures below the level of the excavation are observed, suggesting the development of an arching effect (Terzaghi, 1936; Handy, 1985; Paik & Salgado, 2003; Clayton et al., 2014, among others). This effect is caused mainly by the rotation of the principal stresses (Handy, 1985). All measurements with the tactile sensor are very similar to each other under independent setups. In addition, the FEM model prediction follows approximately the same pressure distribution and similar magnitude compared with the experimental measurements for the active side. As shown in the following sections, these physical and FEM model differences in the static phase are less pronounced than in the dynamic phase. This suggests that the level of soil deformation at the static stage is probably too high to be properly modeled with a small-deformation approach and suggests that the model is not able to reproduce the complex stress redistribution related to the development of the arching effect.

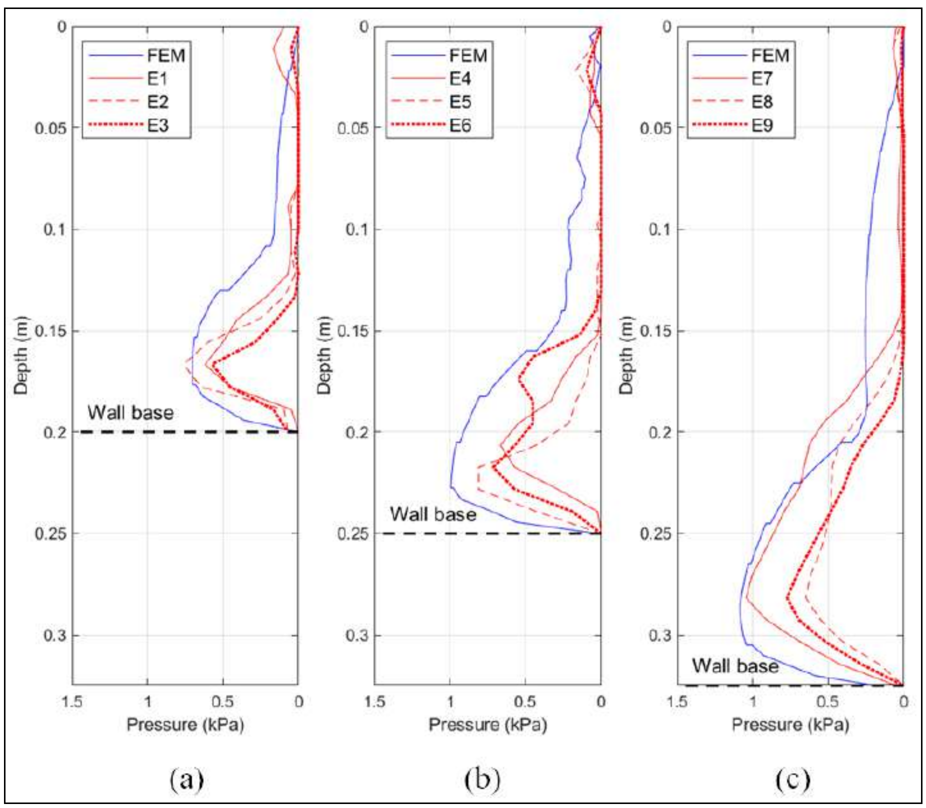

Figure 4-7: Static pressure distribution before the tests for retaining walls: (a) RW-200; (b) RW-250; (c) RW-325

4.4.2 Comparison of numerical model and local dynamical measurements

Figure 4-8(a-b) shows the acceleration and displacement at surface (CP-11) corresponding to the tests E1, E4 and E7. The numerical results are compared with the physical measurements of accelerations (Acc) and displacement (u). In general terms, a good agreement between accelerations is observed, in terms of both amplitude and shape. However, the maximum amplitudes of the accelerations in the numerical model tend to be somewhat higher than in the physical model. In terms of displacements, the numerical and physical results also show similarity. Very close to the surface (CP-11), the material is less confined, the stiffness is very small and the numerical model predicts very well the physical model displacements inferred by DIC, especially for the RW-250 case (E4). On the other hand, in both results (FEM and experimental) a reduction of the permanent surface displacement (CP-11) can be observed as the wall height increases.

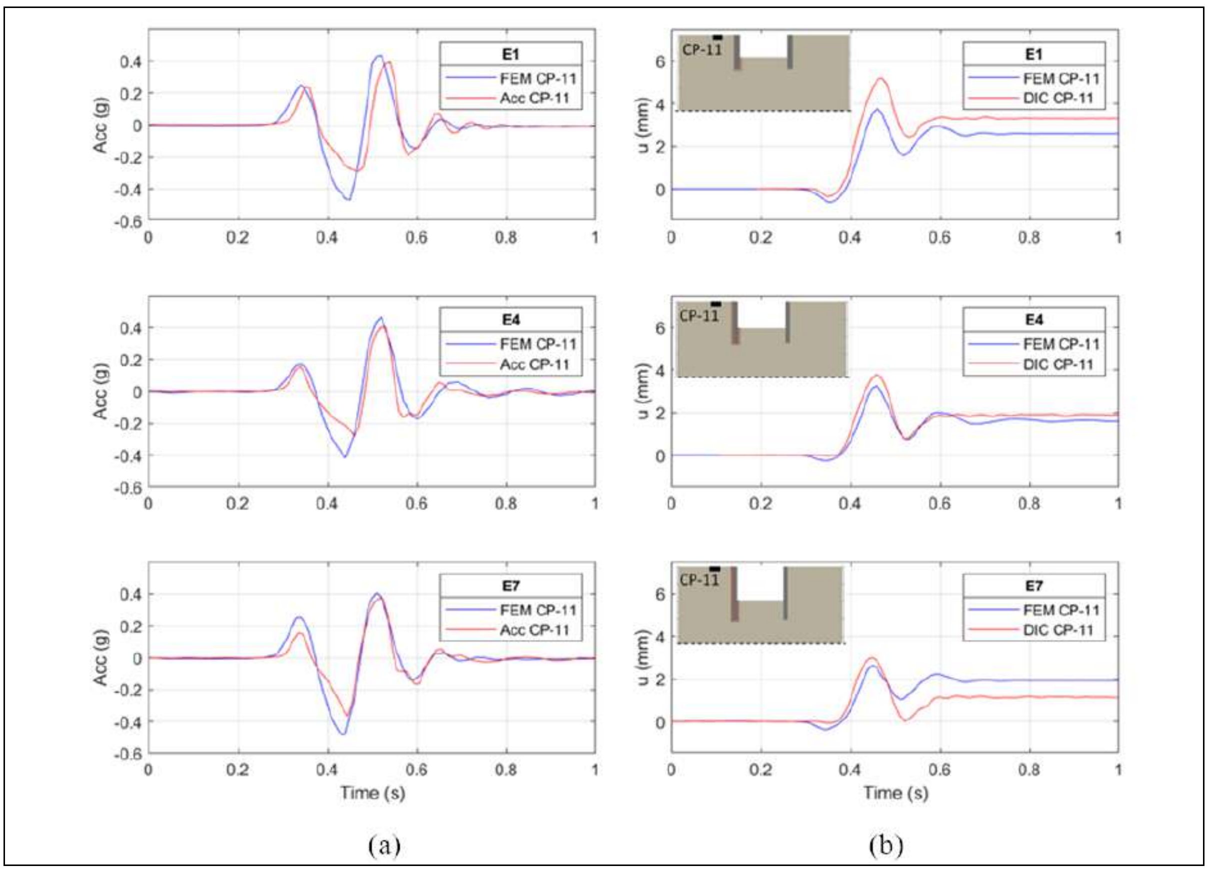

Figure 4-8: Comparison between numerical model (FEM) and: (a) accelerometers; (b) DIC

4.4.3 Global analysis of dynamical behavior of the retaining system by DIC and tactile sensor

The interaction of the backfill and the retaining system was monitored using the DIC technique, allowed by the complete and continuous visualization of the experiment through the transparent side of the laminar box. Both the backfill and wall are analyzed for each test together with the dynamic pressure distribution.

4.4.3.1 Backfill displacement and dynamic earth pressure

This section presents the displacement field of the retaining system and its relationship to the pressure distribution on both the active and passive sides. Figure 4-9 to Figure 4-11 are composed by three columns of images where the arrows indicate the direction of motion. Each column, left, middle, right, corresponds to one configuration, RW-200, RW-250 and RW-325, respectively; in the upper part the corresponding code of the test is indicated (E1, E2, etc.). The corresponding input motion is displayed in the upper panel of each figure.

For test E1, with an amplitude of 0.27 g and a central frequency of 5 Hz (Figure 4-9a), the development of the active wedge can be seen. However, the portion of the soil that concentrates the greatest displacements varies over time as this is observed particularly in the left wall. Comparing the most deformed zones for the same configuration and different motions (Figure 4-10 and Figure 4-11), it shows that the dynamic wedge cannot be considered fixed but it depends on the input motion and geometric characteristics of the wall. The size of this wedge is progressively reduced with the height of wall, except for the input motion of 0.38 g amplitude (E9), which develops larger displacement for the higher wall (Figure 4-11d). This result could be related to the greater rotation of the wall due to its height, which increases the horizontal dynamic displacement of the contained soil. On the contrary, the input motion of lower amplitude and higher frequency (E5) generates larger displacement for the medium-height wall RW-250 (Figure 4-10c), showing that the wedge formation also depends on the frequency content of the input.

For all cases, field displacement on the backfill is not uniform with a progressive change in the shape of the active wedge as time progresses. At the instant of maximum displacement, the shape of this wedge is approximately triangular as assumed in traditional design methods. On the other hand, Ricker wavelets were selected to avoid a symmetrical response and to induce a reduced load on the right-hand walls. On these walls, the development of an active wedge is only clear for some configurations with inputs of large amplitude (i.e., 0.27 g and 0.38 g).

The passive wedge presents relatively small displacements values compared with the active wedge. However, for the case of the highest wall (RW-325), a greater development of this wedge can be observed for tests E7, E8, and E9. This means that it is more influenced by the input magnitude than by the frequency, since tests E7 and E9 have the same frequency, but the latter is characterized by a greater acceleration amplitude.

The dynamically induced earth pressure distribution and the evolution of the lateral thrust increase for the active and passive side are shown in the lower part of the figure panel. The selected data times correspond to those of the DIC analysis for comparison purposes. It is observed that, for all cases, the dynamic pressure increase is very small in the upper portion of the backfill, and it is larger below the excavation grade. For the RW-200 and RW-250 cases, the passive dynamic thrust increase is higher than the active thrust; the reason is attributed to the translational component of a rigid body motion of the wall, which tends to compress the passive side of the soil. Also, it can be noted that the minimum active thrust coincides with a counterclockwise rotation of the wall. For the RW-325 case, the decrease in pressure is significantly greater than on the passive side.

In general terms, some boundary effects begin to appear for the highest amplitude signal (Ricker wavelet 3) due to an increase in displacements, therefore, especially for the case of the tallest wall, the results for the input number 3 have some contamination by boundary effects. For example, the left wedge begins to reach the boundary of the box, while a concentration of deformation appears in the upper right corner of the model, due to the right-to-left movement of the upper rings of the laminar box.

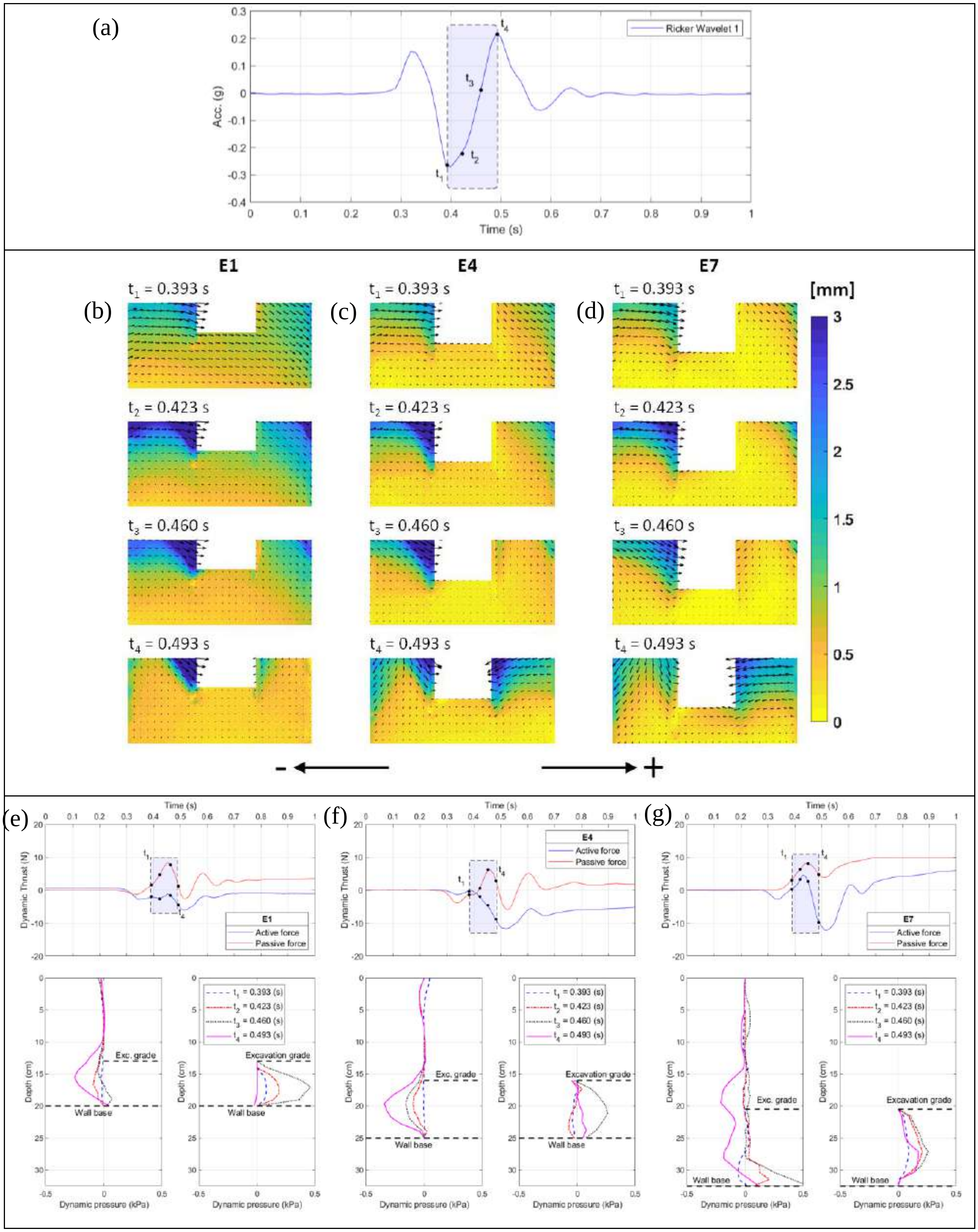

Figure 4-9: Response of the three cases of Retaining walls for Ricker wavelet 1

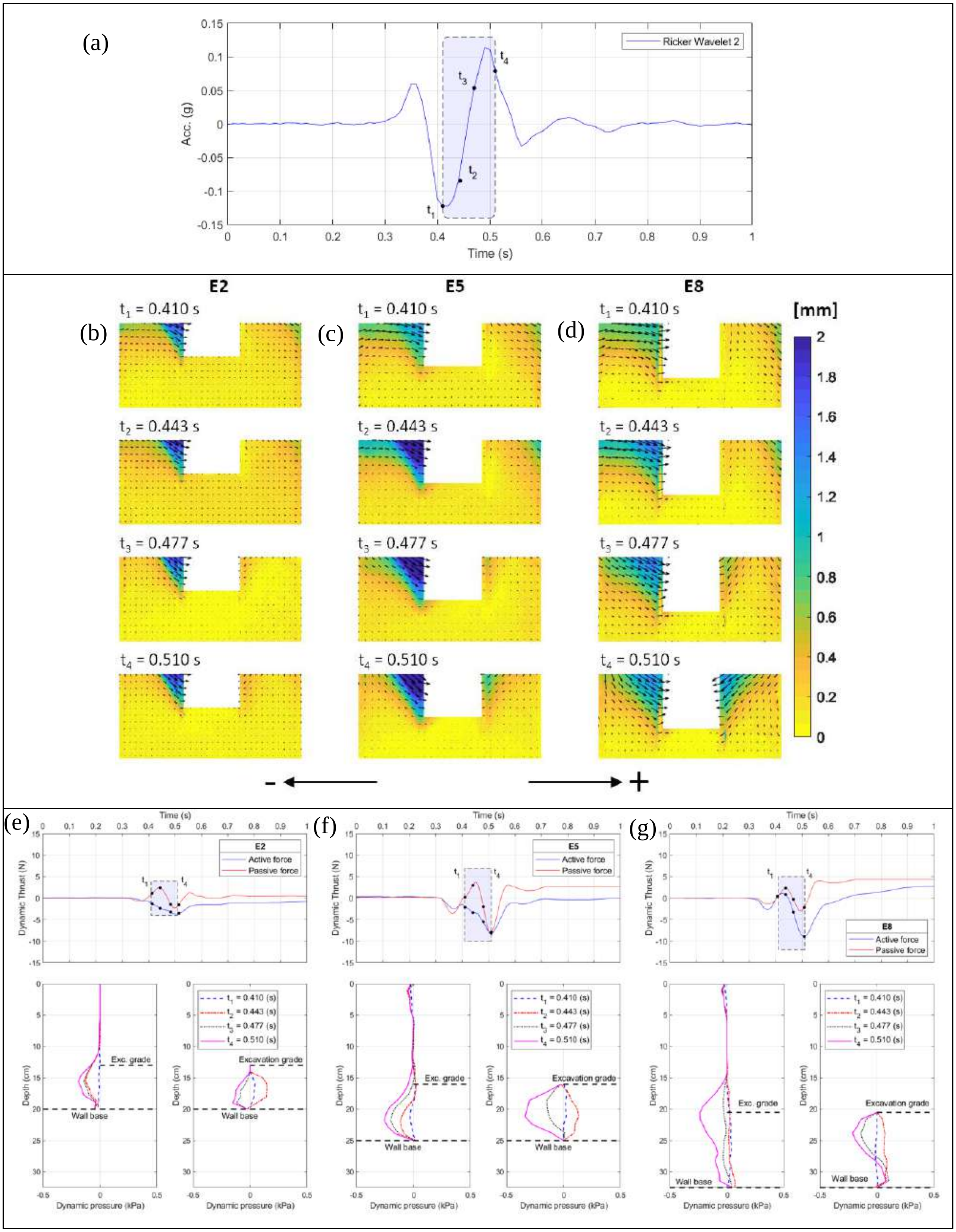

Figure 4-10: Response of the three cases of Retaining walls for Ricker wavelet 2

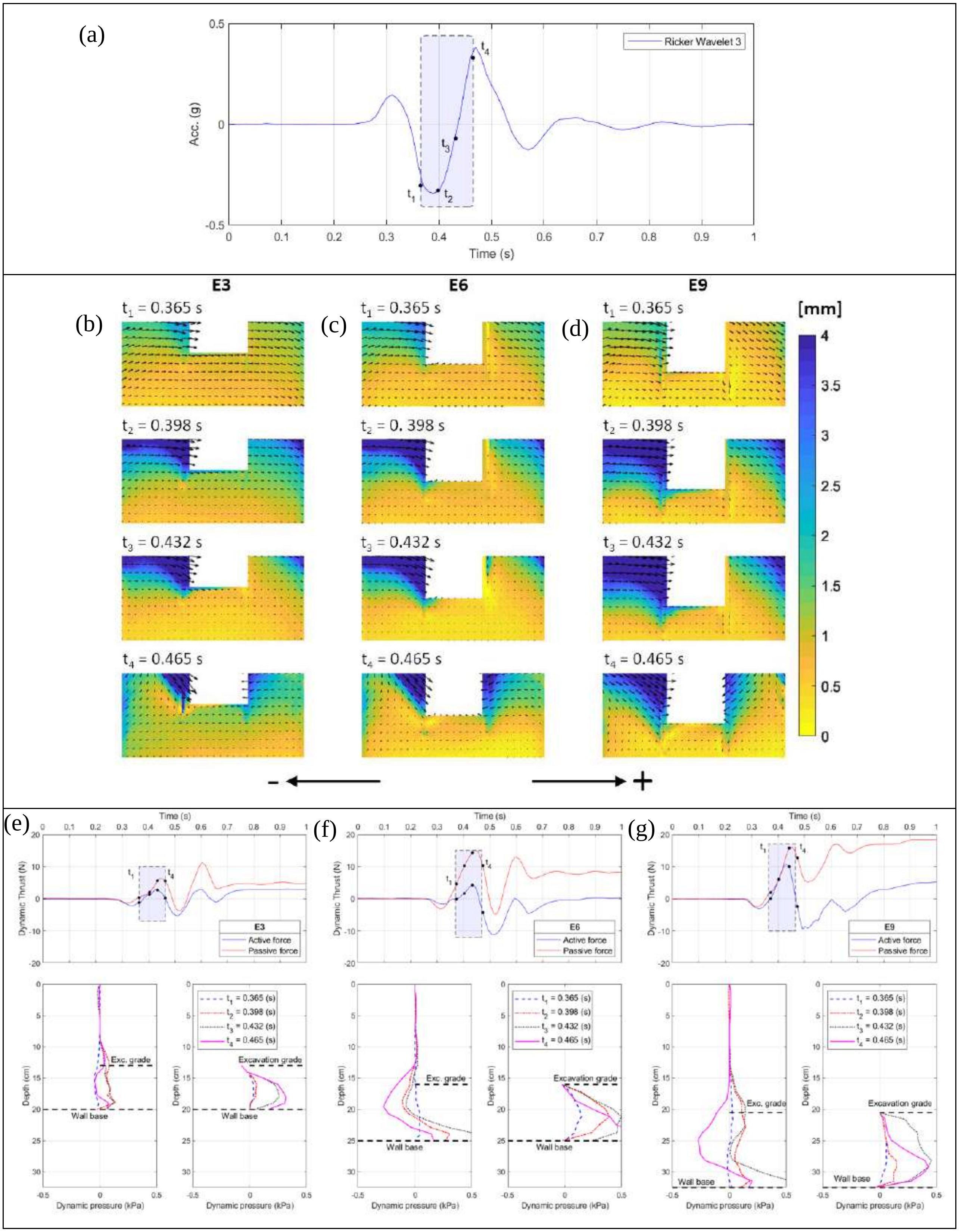

Figure 4-11: Response of the three cases of Retaining walls for Ricker wavelet 3

Figure 4-12 shows the active and passive dynamic thrusts increase for the three studied cases, both numerical and experimental values are similar but have some differences. Although the active and passive thrusts of the FEM model are very similar to each other, the test results show more variability. In general, the instants of the maximum and minimum values coincide, but with differences in their amplitudes. According to the experimental results, the passive force tends to be higher than the active force, suggesting that part of the lateral dynamic increase is transferred as a tangential force at the base of the wall. Since the wall rotates and the sensor can only measure the normal stress to the surface, this difference is also partially explained by the rotation of the wall. However, since it is a continuous tactile sensor that is bent at the corners of the wall, the measurement in these areas is also not accurate, which could introduce some error to the experimental results. Regarding the residual thrust at the end of the seismic loading, the values are very similar for the E3 case, while there are differences for the other two cases. For the E6 case, the residual active thrust is almost zero, while the passive thrust corresponds to approximately 60% of the maximum dynamic thrust. The FE model for this case produces intermediate values to these two readings. For the E8 case, the active and passive residual thrusts are similar, while that of the FE model is very small. It is also interesting to note that the maximum dynamic active thrust is similar in all three cases, but very different values are observed for the peak passive thrust.

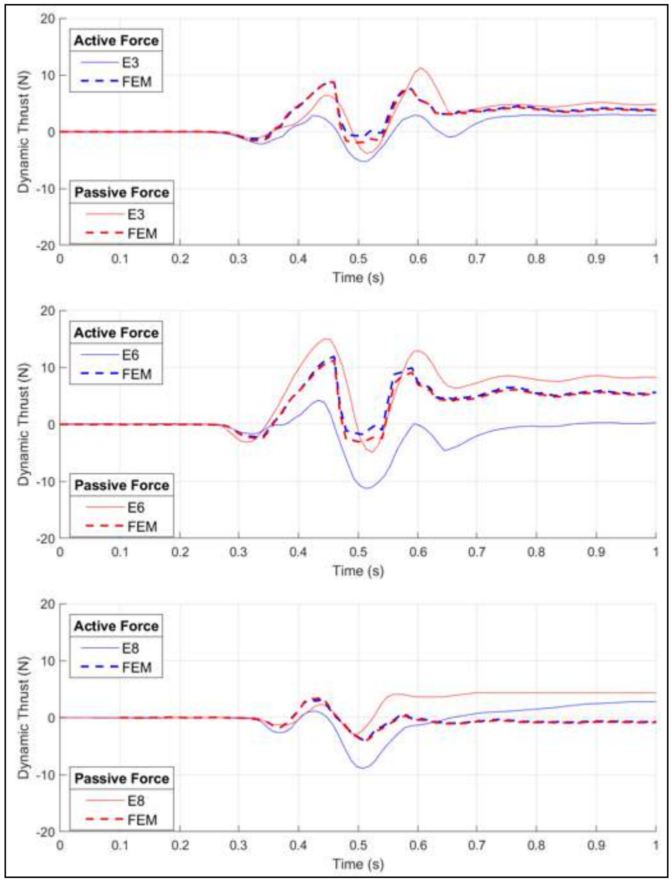

Figure 4-12: Comparison between FEM and experimental results

4.4.3.2 Wall rotation and acting force location

The rotation of left walls inferred by DIC is shown in Figure 4-13. The results indicate that the rotation of the highest wall RW-325 (E7, E8 and E9) is the smallest in comparison to the other two walls. This is probably because the highest wall is also the one with the largest buried length (although the ratio of wall height to buried portion is a constant for three configurations). Additionally, the smallest wall RW-200 (E1, E2 and E3) exhibited the greatest rotation probably because it has reduced passive force contribution and because of the lower confinement (and stiffness) of the backfill. The medium-height wall showed the maximum rotation (E5) only for the case of lower amplitude (0.12 g). Residual deformation is observed in all cases. Nevertheless, the increase in rotation is not monotonous, since a restitution effect could be noted for tests E3, E6 and E9, but with less extent in cases E1, E4 and E7.

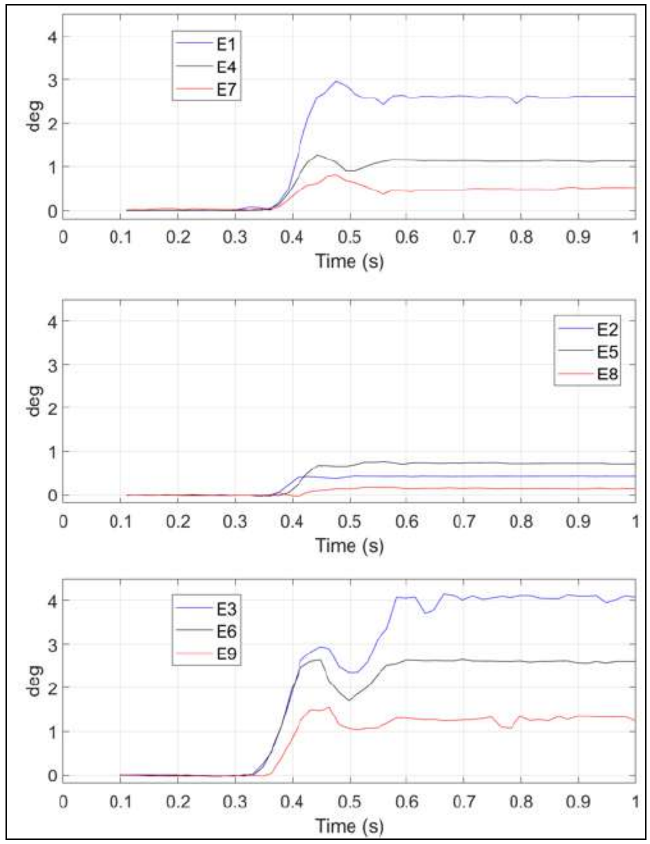

Figure 4-13: Rotation of walls for the different test configurations (positive values indicate a clockwise rotation of the wall)

The location of the acting dynamic force was determined by calculating the vertical centroid of the dynamic pressure distribution over time. To compare this height, considering all the wall configurations, the results are presented as a height ratio with respect to each wall, i.e., HR = force application height / total wall height (Figure 4-14). Besides, the rate of increase obtained by the FEM approach is very similar to the experimental one in most cases.

Figure 4-14 shows an increase in height of the application point of the dynamic thrust force with respect to the base of the walls. This increase occurs gradually as the active thrust develops and is correlated to the wall rotation. As can be noted from Table 4-6, walls with the lowest rotation (E2, E4, E5 and E8 with $\theta_{\mathrm{End}} \leq 1.1^{\circ}$) do not experience significant changes of HR, showing a close to constant value and even a small reduction in the HR with respect to the initial value.

Other cases with a more significant residual rotation (E1, E3, E6 y E9 with $\theta_{\mathrm{End}} \geq 1.2°$) show a tendency to increase the HR value during the dynamic loading. Therefore, the change in the location of the thrust application point of the active side of the wall is strongly influenced by the rotation. In general terms, although with some differences during the loading, the computational model was able to predict the HR_{End} value, although with a slightly higher estimate compared to the experimental observation in most cases.

Table 4-6: Height ratio (HR) evolution and wall rotation

RW-200				RW-250				RW-325			
Test	**HR_{Begin}**	**HR_{End}**	**θ_{End}(°)**	**Test**	**HR_{Begin}**	**HR_{End}**	**θ_{End}(°)**	**Test**	**HR_{Begin}**	**HR_{End}**	**θ_{End}(°)**
E1	0.29	0.45	2.6	**E4**	0.25	0.18	1.1	**E7**	0.24	0.29	0.5
E2	0.21	0.17	0.4	**E5**	0.21	0.20	0.7	**E8**	0.25	0.23	0.1
E3	0.23	0.45	4.1	**E6**	0.24	0.44	2.6	**E9**	0.19	0.38	1.2

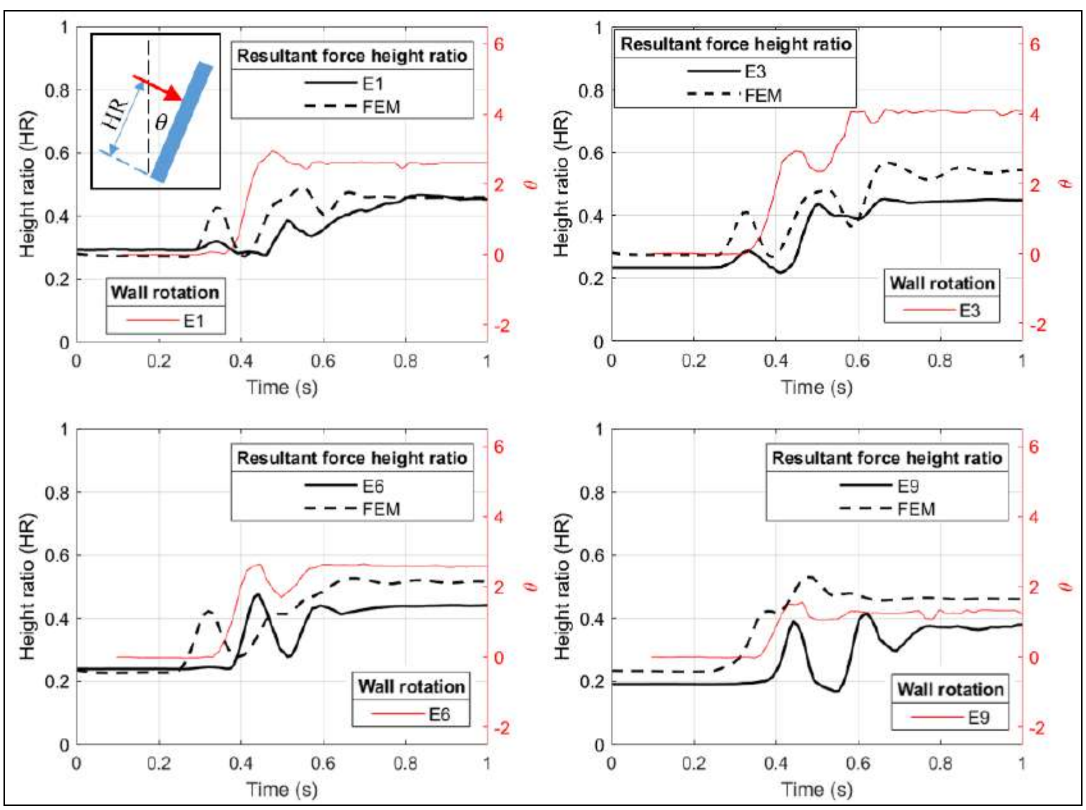

Figure 4-14: Height ratio and wall rotation evolution during the loading

4.5 Conclusions

The present study is based on 1-g physical small-scale models of retaining walls, considering three different heights and embedment depths. The models were built in a laminar box with a transparent side on a shaking table used to generate dynamic motion in terms of Ricker wavelets. The research includes continuous monitoring of the dynamic soil pressure distribution acting on the walls by means of a tactile sensor and backfill displacement analysis using the DIC technique. The movement of the soil and the wall was correlated with the dynamic thrusts exerted on the retaining structures. A numerical model (HS-Small) was calibrated to compare local and spatially distributed measurement of the experiment. The main conclusions are numerated below:

1. The actual distribution of dynamic pressures acting on the retaining walls was evaluated. Experimental and numerical results showed a distribution of static pressures different from the triangular shape expected for a rigid gravity wall. The results are consistent with pressure distributions associated with the generation of arching effect in the backfill. The differences found between the experimental and numerical models are quite reasonable.

2. The analysis of the soil displacement pattern carried out by the DIC technique reveals that the angle of the active wedge (i.e., size) cannot be considered constant during the dynamic loading. The backfill displacement and wall movement vary according to the intensity and frequency of the motion.

3. The variation of the vertical location of the resultant soil thrust is strongly affected by the wall rotation, indicating that there is a tendency to increase its height for larger residual wall rotation. On the contrary, for low levels of rotation, the location of the resulting force tends to be almost constant. Therefore, for design purposes, the estimation of the movement of the retaining structure and the location of the seismic thrust should be part of the calculation since they are strongly related.

5. SUMMARY AND OVERALL CONCLUSIONS

The aim of this research was to study the effects of DSSI in semi-buried structures, i.e., buildings with underground stories and partially buried retaining wall systems by means of physical modeling in a novel transparent laminar box. The specific objectives of the research can be summarized in the following stages:

1. Design, construct, and validate of a new transparent laminar box, as a tool for the analysis of the non-linear soil behavior during dynamic testing in a 1-g shaking table (***Paper I***).

2. Evaluate the effects of DSSI using a scaled building with underground stories in the physical model (***Paper II***).

3. Evaluate the effects of DSSI using a scaled retaining wall system in the physical model (***Paper III***).

4. Carry out numerical models reproducing the physical models using the finite element method for the studied configurations (***Paper I*** and ***III***).

Chapter 2 introduced a new device for physical modeling in geotechnical experiments. This device was able to replicate the non-linear soil behavior due to its flexibility characteristics. Besides, thanks to the transparency of the front side of the container, it was possible to track the soil behavior continuously in time and space and compare it against local measurements (i.e., accelerometers). The modulus reduction and damping curves for the studied sand, derived from images and accelerometers, agreed with the experimental results obtained from resonant column tests. Additionally, the complete displacement field was analyzed with the DIC technique.

Chapter 3 describes the DSSI effects for scaled buildings with different configurations of both number of stories and underground levels. The transparency of the laminar box makes it possible to reveal the correlation between the non-linear soil behavior, the dynamic induced pressures, and the building rocking. It was found that the kinematic interaction and the way the dynamic pressure is distributed along the wall is significantly influenced by the superstructure vibration.

Chapter 4 describes the nonlinear behavior of the soil and its interaction with retaining systems. The wall height was varied to study the effects of the embedded portion on the dynamic response. It was possible to correlate the dynamic pressure distribution with the soil motion through the DIC analysis. The results showed the variation of shape of the active wedge during the dynamic phase, which is contrary to theoretical assumptions that consider a static behavior. Furthermore, it is shown that the height of the application point of the resultant force varies as a function of wall rotation. Also, it was possible to replicate the experimental results using a finite element model in a commercial software.

This investigation demonstrates the importance to consider the DSSI effects in semi-buried structures. The way the problem was approached makes the study unique in comparison to similar research usually done in conventional laminar boxes with a limited local instrumentation. In contrast, the new laminar box benefits from a design that has no limitations in terms of deformation measurements in the soil and structure for a 2D analysis. In addition, not only the spatio-temporal measurement of the deformation pattern is evaluated, but it was also possible to correlate this measurement with a tactile sensor, capable of recording the distribution of pressures in the underground walls as well as in the retaining walls. Currently, this measurement could only be performed by means of locally distributed pressure transducers.

On the other hand, the distribution of pressures in walls has been a subject with very little progress in recent years and leaves a lot of uncertainty, even more so in dynamic conditions. Therefore, the results obtained could be of interest for design purposes since they allow having a more realistic description of the stresses and deformations present in this type of structures. An extrapolation is not adequate since we worked at 1-g confinement levels, however, the main idea was to identify in a qualitative way the mechanism of soil-structure interaction and to establish a correlation between soil displacement and the dynamic pressure distribution.

From a practical point of view, a methodology has been developed for the correct use of the transparent laminar box in future investigations, considering different technical aspects for the proper functioning of the experimental tests, such as the appropriate light intensity, the speed of image capture, as well as the image resolution and the focal distance to the target. Even the issue of data synchronization can be solved considering the aforementioned recommendations. Moreover, the choice of scaling factors was in accordance with the limitations of the shaking table, both in amplitude and frequency, and for a less computationally expensive analysis, we selected Ricker synthetic signals characterized by their short duration, in addition to having an equivalence in frequency content with real earthquakes. Several recommendations were considered from the internship at the University of Auckland, New Zealand, where, together with other researchers, the dynamic interaction between structure-soil-structure in physical models was evaluated through a generic laminar box, different strategies were learned that contributed to the development of this research.

Finally, the device developed in this research allows the evaluation of different types of configurations of soil-structure interaction systems that are characterized by being partially or totally buried as is the case of tunnels. In addition, it can also address the problem of discontinuous retaining systems such as piles. Besides, there is the possibility of improving the design of the laminar box that would enable: first, testing under saturated conditions to study the increase in pore pressure under different failure mechanisms and second, a modification to the back of the container to make it transparent would allow studying 3D problems with a suitable set of cameras.

5.1 Future research

The present research has successfully validated the use of a new laminar box device for DSSI experimentation in a 1-g environment. Thus, a contribution is made to the field of physical modeling. However, recommendations for further investigations are as follows.

1. The novel design of the laminar box used in this research allows to visualize the full field of the front side, and all tests are developed in dry conditions with

granular particles. However, an upgrade of the container to perform saturated tests would be encouraging for evaluating the pore pressure increase, for instance, the liquefaction phenomenon, since the transparency feature of the laminar box would reveal very relevant results in this kind of situations.

2. The physical models developed in this investigation for studying DSSI in buildings with underground stories are analyzed for the first vibration mode, an improvement of the shaking table to reach higher frequencies would allow the evaluation of higher vibration modes and their influence on the building response, since this issue is hardly considered in most analyses. This upgrade of the shaking table is currently in progress. Therefore, it is expected to be able to explore a wide range of scale factors in the future.

3. Taking advantage of the transparency of the laminar box, the investigation of Dynamic Structure-Soil-Structure Interaction (DSSSI) would reveal important results in this area. In addition, the interaction of completely buried structures (e.g., tunnels) could be studied individually and as a group.

4. Considering the satisfactory results obtained with the new transparent laminar box, it would be interesting the preparation of a new laminar box that is transparent on both sides instead of just one side. This feature would allow the use of transparent synthetic soils and other three-dimensional structures (e.g., pile groups, isolated foundations, etc.). Moreover, with the appropriate set of cameras and spatial distribution, 3D analysis can be easily performed as well as Particle Image Velocimetry (PIV).

BIBLIOGRAPHY

Abate, G., Massimino, M. R., Maugeri, M., & Wood, D. M. (2010). Numerical modelling of a shaking table test for soil-foundation-superstructure interaction by means of a soil constitutive model implemented in a FEM code. *Geotechnical and Geological Engineering*, *28*(1), 37–59.

Adrian, R. J. (1991). Particle-imaging techniques for experimental fluid mechanics. *Annual Review of Fluid Mechanics*, *23*(1), 261–304.

Ahmadi, E. (2019). Concurrent effects of inertial and kinematic soil-structure interactions on strength-ductility-period relationship. *Soil Dynamics and Earthquake Engineering*, *117*(August 2018), 174–189. https://doi.org/10.1016/j.soildyn.2018.10.043.

Al Atik, L., & Sitar, N. (2010). Seismic earth pressures on cantilever retaining structures. *Journal of Geotechnical and Geoenvironmental Engineering*, *136*(10), 1324–1333.

Alaie, R., & Chenari, R. J. (2018). Design and performance of a single axis shake table and a laminar soil container. *Civil Engineering Journal*, *4*(6), 1326–1337.

American Society of Civil Engineers. (2017). Seismic evaluation and retrofit of existing buildings. American Society of Civil Engineers.

Anderson, D. G. (2008). *Seismic analysis and design of retaining walls, buried structures, slopes, and embankments* (Vol. 611). Transportation Research Board.

Asadi-Ghoozhdi, H., & Attarnejad, R. (2020). A Winkler-based model for inelastic response of soil–structure systems with embedded foundation considering kinematic and inertial interaction effects. *Structures*, *28*, 589–603.

Avilés, J., & Pérez-Rocha, L. E. (1996). Evaluation of interaction effects on the system period and the system damping due to foundation embedment and layer depth. *Soil Dynamics and Earthquake Engineering*, *15*(1), 11–27.

Avilés, J., & Pérez-Rocha, L. E. (1998). Effects of foundation embedment during building-soil interaction. *Earthquake Engineering and Structural Dynamics*, *27*(12), 1523–1540.

Bararnia, M., Hassani, N., Ganjavi, B., & Amiri, G. G. (2018). Estimation of inelastic displacement ratios for soil-structure systems with embedded foundation considering kinematic and inertial interaction effects. *Engineering Structures*, *159*, 252–264.

Bellezza, I. (2014). A new pseudo-dynamic approach for seismic active soil thrust. *Geotechnical and Geological Engineering, 32*(2), 561–576.

Bellezza, I. (2015). Seismic active earth pressure on walls using a new pseudo-dynamic approach. *Geotechnical and Geological Engineering*, *33*(4), 795–812.

Benz, T. (2007). *Small-strain stiffness of soils and its numerical consequences* (Vol. 5). Univ. Stuttgart, Inst. f. Geotechnik Stuttgart.

Berenger, J.-P. (1994). A perfectly matched layer for the absorption of electromagnetic waves. *Journal of Computational Physics*, *114*(2), 185–200.

Bielak, J. (1974). Dynamic behaviour of structures with embedded foundations. *Earthquake Engineering & Structural Dynamics*, *3*(3), 259–274.

Bielak, J., & Christiano, P. (1984). On the effective seismic input for non-linear soil-structure interaction systems. *Earthquake Engineering & Structural Dynamics*, *12*(1), 107–119.

Biondi, G., Massimino, M. R., & Maugeri, M. (2015). Experimental study in the shaking table of the input motion characteristics in the dynamic SSI of a SDOF model. *Bulletin of Earthquake Engineering*, *13*(6), 1835–1869.

Bolton, M. D., Britto, A. M., Powrie, W., & White, T. P. (1989). Finite element analysis of a centrifuge model of a retaining wall embedded in a heavily overconsolidated clay. *Computers and Geotechnics*, *7*(4), 289–318.

Bolton, M. D., & Steedman, R. S. (1982). *Centrifugal testing of microconcrete retaining walls subjected to base shaking*. University of Cambridge Engineering Department.

Bolton, M. D., & Steedman, R. S. (1985). *The behaviour of fixed cantilever walls subject to lateral shaking*.

Brandenberg S.J., Durante M. G., Mylonakis G., Stewart J.P. (2020): "Winkler Solution for Seismic Earth Pressures Exerted on Flexible Walls by Vertically Inhomogeneous Soil", Journal of Geotechnical and Geoenvironmental Engineering, 146(11), 04020127

Brennan, A. J., Thusyanthan, N. I., & Madabhushi, S. P. (2005). Evaluation of shear modulus and damping in dynamic centrifuge tests. *Journal of Geotechnical and Geoenvironmental Engineering*, *131*(12), 1488–1497.

Çelebi, E., Göktepe, F., & Karahan, N. (2012). Non-linear finite element analysis for prediction of seismic response of buildings considering soil-structure interaction. *Natural Hazards and Earth System Sciences*, *12*(11), 3495–3505.

Chau, K. T., Shen, C. Y., & Guo, X. (2009). Nonlinear seismic soil–pile–structure interactions: shaking table tests and FEM analyses. *Soil Dynamics and Earthquake Engineering*, *29*(2), 300–310.

Chopra, A. K., & Gutierrez, J. A. (1974). Earthquake response analysis of multistorey buildings including foundation interaction. *Earthquake Engineering & Structural Dynamics*, *3*(1), 65–77.

Choudhury, D., & Nimbalkar, S. S. (2006). Pseudo-dynamic approach of seismic active earth pressure behind retaining wall. *Geotechnical & Geological Engineering*, *24*(5), 1103–1113.

Cilingir, U., & Madabhushi, S. P. G. (2010). Particle Image Velocimetry analysis in dynamic centrifuge tests. In *Physical Modelling in Geotechnics, Two Volume Set: Proceedings of the 7th International Conference on Physical Modelling in Geotechnics (ICPMG 2010), 28th June-1st July, Zurich, Switzerland* (Vol. 1, p. 319). CRC Press.

Clayton, R., & Engquist, B. (1977). Absorbing boundary conditions for acoustic and elastic wave equations. *Bulletin of the Seismological Society of America*, *67*(6), 1529–1540.

Clayton, C. R. I., Woods, R. I., & Milititsky, J. (2014). *Earth pressure and earth-retaining structures*. CRC press.

Clouteau, D., Broc, D., Devésa, G., Guyonvarh, V., & Massin, P. (2012). Calculation methods of Structure-Soil-Structure Interaction (3SI) for embedded buildings: Application to NUPEC tests. *Soil Dynamics and Earthquake Engineering*, *32*(1), 129–142. https://doi.org/10.1016/j.soildyn.2011.08.005

Conti, R, Madabhushi, G. S. P., & Viggiani, G. M. B. (2012). On the behaviour of flexible retaining walls under seismic actions. *Géotechnique*, *62*(12), 1081–1094.

Conti, R, Viggiani, G. M. B., & Burali d'Arezzo, F. (2015). Some remarks on the seismic behaviour of embedded cantilevered retaining walls. *Geotechnical Earthquake Engineering: Géotechnique Symposium in Print 2015*, 137–147.

Conti, Riccardo, & Viggiani, G. M. B. (2013). A new limit equilibrium method for the pseudostatic design of embedded cantilevered retaining walls. *Soil Dynamics and Earthquake Engineering*, *50*, 143–150.

Conti, R., Morigi, M., & Viggiani, G. M. B. (2017). Filtering effect induced by rigid massless embedded foundations. *Bulletin of Earthquake Engineering*, *15*(3), 1019–1035.

Deeks, A. J., & Randolph, M. F. (1994). Axisymmetric time-domain transmitting boundaries. *Journal of Engineering Mechanics*, *120*(1), 25–42.

Dewoolkar, M., Ko, H. Y., & Pak, R. Y. S. (2000). Experimental developments for studying static and seismic behavior of retaining walls with liquefiable backfills. *Soil Dynamics and Earthquake Engineering*, *19*(8), 583–593. https://doi.org/10.1016/S0267-7261(00)00069-5

Dewoolkar, M. M., Ko, H.-Y., & Pak, R. Y. S. (2001). Seismic behavior of cantilever retaining walls with liquefiable backfills. *Journal of Geotechnical and Geoenvironmental Engineering*, *127*(5), 424–435.

Dietz, M., & Muir Wood, D. (2007). Shaking table evaluation of dynamic soil properties. In *Proceedings of 4th international conference on earthquake geotechnical engineering*.

Dihoru, L., Bhattacharya, S., Moccia, F., Simonelli, A. L., Taylor, C. A., & Mylonakis, G. (2016). Dynamic testing of free field response in stratified granular deposits. *Soil Dynamics and Earthquake Engineering*, *84*, 157–168.

Dobry, R., Gazetas, G., & Stokoe, K. H. (1987). Dynamic response of arbitrarily shaped foundations: Experimental verification. *Journal of Geotechnical Engineering*, *113*(11), 1412–1416. https://doi.org/10.1061/(ASCE)0733-9410(1987)113:11(1412)

Durante MG, Stewart JP, Brandenberg SJ, Mylonakis G. Simplified solution for seismic earth pressures exerted on flexible walls. Earthquake Spectra. March 2022. doi:10.1177/87552930221083326

Ecemis, N. (2013). Simulation of seismic liquefaction: 1-g model testing system and shaking table tests. *European Journal of Environmental and Civil Engineering*, *17*(10), 899–919. https://doi.org/10.1080/19648189.2013.833140

Eichhorn, G. N., Bowman, A., Haigh, S. K., & Stanier, S. (2020). Low-cost digital image correlation and strain measurement for geotechnical applications. *Strain*, *56*(6), e12348.

Elgamal, A., Yang, Z., Lai, T., Kutter, B. L., & Wilson, D. W. (2005). Dynamic response of saturated dense sand in laminated centrifuge container. *Journal of Geotechnical and Geoenvironmental Engineering*, *131*(5), 598–609.

Elsabee, F., & Murray, J. P. (1977). Dynamic Behavior of Embedded Foundations. *R77-33*, *578*, 5–6.

Fayad, S. S., Seidl, D. T., & Reu, P. L. (2020). Spatial DIC errors due to pattern-induced bias and grey level discretization. *Experimental Mechanics*, *60*(2), 249–263.

FEMA P-2082-1. (2020). NEHRP (National Earthquake Hazards Reduction Program) Recommended Seismic Provisions for New Buildings and Other Structures.

FEMA P-2091. (2020). Federal Emergency Management Agency. A Practical Guide to Soil-Structure Interaction.

Fu, J., Liang, J., & Han, B. (2017). Impedance functions of three-dimensional rectangular foundations embedded in multi-layered half-space. *Soil Dynamics and Earthquake Engineering*, *103*, 118–122.

Fu, J., Todorovska, M. I., & Liang, J. (2018). Correction factors for SSI effects predicted by simplified models: 2D versus 3D rectangular embedded foundations. *Earthquake Engineering & Structural Dynamics*, *47*(9), 1963–1983.

Gao, H., Hu, Y., Wang, Z., Wang, C., & Chen, G. (2017). Shaking table tests on the seismic performance of a flexible wall retaining EPS composite soil. *Bulletin of Earthquake Engineering*, *15*(12), 5481–5510.

Gazetas, G. (1991). Formulas and charts for impedances of surface and embedded foundations. *Journal of Geotechnical Engineering*, *117*(9), 1363–1381.

Geraili Mikola, R., Candia, G., & Sitar, N. (2016). Seismic earth pressures on retaining structures and basement walls in cohesionless soils. *Journal of Geotechnical and Geoenvironmental Engineering*, *142*(10), 4016047.

Goit, C. S., Saitoh, M., Oikawa, H., & Kawakami, H. (2014). Effects of soil nonlinearity on the active length of piles embedded in cohesionless soil: Model studies. *Acta Geotechnica*, *9*(3), 455–467. https://doi.org/10.1007/s11440-013-0257-0

Goit, Chandra Shekhar, Saitoh, M., Igarashi, T., & Sasaki, S. (2021). Inclined single piles under vertical loadings in cohesionless soil. *Acta Geotechnica*, *16*(4), 1231–1245.

Green, R A, & Ebeling, R. M. (2003). Modeling the dynamic response of cantilever earth-retaining walls using FLAC. *3rd International Symposium on FLAC: Numerical Modeling in Geomechanics, Sudbury, Canada*.

Green, Russell A, Olgun, C. G., & Cameron, W. I. (2008). Response and modeling of cantilever retaining walls subjected to seismic motions. *Computer-Aided Civil and Infrastructure Engineering*, *23*(4), 309–322.

Guddati, M. N., & Tassoulas, J. L. (2000). Continued-fraction absorbing boundary conditions for the wave equation. *Journal of Computational Acoustics*, *8*(01), 139–156.

Hall, S. A., Bornert, M., Desrues, J., Pannier, Y., Lenoir, N., Viggiani, G., & Bésuelle, P. (2010). Discrete and continuum analysis of localised deformation in sand using X-ray [mu] CT and volumetric digital image correlation. *Géotechnique*, *60*(5), 315.

Hall, S. A., Wood, D. M., Ibraim, E., & Viggiani, G. (2010). Localised deformation patterning in 2D granular materials revealed by digital image correlation. *Granular Matter*, *12*(1), 1–14.

Handy, R. L. (1985). The arch in soil arching. *Journal of Geotechnical Engineering*, *111*(3), 302–318.

Hokmabadi, A. S., Fatahi, B., & Samali, B. (2014). Assessment of soil–pile–structure interaction influencing seismic response of mid-rise buildings sitting on floating pile foundations. *Computers and Geotechnics*, *55*, 172–186.

Hushmand A, Dashti S, Davis C and Hushmand B (2016) Seismic performance of underground reservoir structures: Insight from centrifuge modeling on the influence of structure stiffness. Journal of Geotechnical and Geoenvironmental Engineering 142(11): 04016058.

Hushmand, B., Scott, R. F., & Crouse, C. B. (1988). Centrifuge liquefaction tests in a laminar box. *Geotechnique*, *38*(2), 253–262.

Iai, S. (1989). Similitude for shaking table tests on soil-structure-fluid model in 1g gravitational field. *Soils and Foundations*, *29*(1), 105–118.

Ichihara, M., & Matsuzawa, H. (1973). Earth pressure during earthquake. *Soils and Foundations*, *13*(4), 75–86.

Ishibashi, I., & Fang, Y.-S. (1987). Dynamic earth pressures with different wall movement modes. *Soils and Foundations*, *27*(4), 11–22.

Jafarzadeh, B. (2004). Design and evaluation concepts of laminar shear box for 1g shaking table tests. *Proceedings of the 13th World Conference on Earthquake Engineering, Vancouver, Paper*, *1391*.

Jardine, R. J., Potts, D. M., Fourie, A. B., & Burland, J. B. (1986). Studies of the influence of non-linear stress–strain characteristics in soil–structure interaction. *Geotechnique*, *36*(3), 377–396.

Jalilian Mashhoud, H., Yin, J.-H., Komak Panah, A., & Leung, Y. F. (2020). A 1-g shaking table investigation on response of a micropile system to earthquake excitation. *Acta Geotechnica*, *15*(4), 827–846.

Jiang, L., Chen, J., & Li, J. (2010). Seismic response of underground utility tunnels: shaking table testing and FEM analysis. *Earthquake Engineering and Engineering Vibration*, *9*(4), 555–567.

Kapogianni, E., Tsafou, S., & Sakellariou, M. (2019). Image Analysis and Structural Monitoring of Physical Geotechnical Models Subjected to Seismic Loading. In *International Conference on Inforatmion technology in Geo-Engineering* (pp. 674–686). Springer.

Kausel, E. (1981). *An explicit solution for the Green functions for dynamic loads in layered media*. Department of Civil Engineering, School of Engineering, Massachusetts Institute of Technology, 1981.

Kim, J., Lee, E., & Lee, S. (2016). Boundary reaction method for nonlinear analysis of soil–structure interaction under earthquake loads. *Soil Dynamics and Earthquake Engineering*, *89*, 85–90.

Kloukinas, P., di Santolo, A. S., Penna, A., Dietz, M., Evangelista, A., Simonelli, A. L., Taylor, C., & Mylonakis, G. (2015). Investigation of seismic response of cantilever retaining walls: Limit analysis vs shaking table testing. *Soil Dynamics and Earthquake Engineering*, *77*, 432–445.

Kutanis, M., & Elmas, M. (2001). Non-linear seismic soil-structure interaction analysis based on the substructure method in the time domain. *Turkish Journal of Engineering and Environmental Sciences*, *25*(6), 617–626.

Langhaar, H. L. (1951). *Dimensional analysis and theory of models* (Vol. 2). Wiley New York.

Latha, G. M., & Krishna, A. M. (2008). Seismic response of reinforced soil retaining wall models: influence of backfill relative density. *Geotextiles and Geomembranes*, *26*(4), 335–349.

Lava, P., & Debruyne, D. (2010). *MatchID*. Catholic University College Ghent.

Lee, J. H., Kim, J. K., & Kim, J. H. (2014). Nonlinear analysis of soil–structure interaction using perfectly matched discrete layers. *Computers & Structures*, *142*, 28–44.

Lee, C. J., Wei, Y. C., & Kuo, Y. C. (2012). Boundary effects of a laminar container in centrifuge shaking table tests. *Soil Dynamics and Earthquake Engineering*, *34*(1), 37–51. https://doi.org/10.1016/j.soildyn.2011.10.011

Lee, T. H., & Wesley, D. A. (1973). Soil-structure interaction of nuclear reactor structures considering through-soil coupling between adjacent structures. *Nuclear Engineering and Design*, *24*(3), 374–387.

Liao, Z., & Wong, H. L. (1984). A transmitting boundary for the numerical simulation of elastic wave propagation. *International Journal of Soil Dynamics and Earthquake Engineering*, *3*(4), 174–183.

Lin, A. N., & Jennings, P. C. (1984). Effect of embedment on foundation-soil impedances. *Journal of Engineering Mechanics*, *110*(7), 1060–1075.

Liu, J., Bao, X., Wang, D., Tan, H., & Li, S. (2019). The internal substructure method for seismic wave input in 3D dynamic soil-structure interaction analysis. *Soil Dynamics and Earthquake Engineering*, *127*, 105847.

Lombardi, D., Bhattacharya, S., Scarpa, F., & Bianchi, M. (2015). Dynamic response of a geotechnical rigid model container with absorbing boundaries. *Soil Dynamics and Earthquake Engineering*, *69*, 46–56.

Luco, J. E., & Contesse, L. (1973). Dynamic structure-soil-structure interaction. *Bulletin of the Seismological Society of America*, *63*(4), 1289–1303.

Luco, Juan Enrique. (1980). Linear soil-structure interaction. *Report UCRL-15272*.

Lysmer, JFER, & Richart Jr, F. E. (1966). Dynamic response of footings to vertical loading. *Journal of the Soil Mechanics and Foundations Division*, *92*(1), 65–91.

Lysmer, John, & Kuhlemeyer, R. L. (1969). Finite dynamic model for infinite media. *Journal of the Engineering Mechanics Division*, *95*(4), 859–877.

Madhavi Latha, G., & Murali Krishna, A. (2008). Seismic response of reinforced soil retaining wall models: Influence of backfill relative density. *Geotextiles and Geomembranes*, *26*(4), 335–349. https://doi.org/10.1016/j.geotexmem.2007.11.001

Mahmoudpour, S., Attarnejad, R., & Behnia, C. (2011). Dynamic analysis of partially embedded structures considering soil-structure interaction in time domain. *Mathematical Problems in Engineering*, *2011*. https://doi.org/10.1155/2011/534968

Mahsuli, M., & Ghannad, M. A. (2009). The effect of foundation embedment on inelastic response of structures. *Earthquake Engineering & Structural Dynamics*, *38*(4), 423–437.

Matsuo, H., & Ohara, S. (1960). Lateral earth pressure and stability of quay walls during earthquakes. In *Proceedings of the Second World Conference on Earthquake Engineering* (Vol. 1, pp. 165–181). Science Council of Japan Tokyo-Kyoto, Japan.

Matthees, W., & Magiera, G. (1982). A sensitivity study of seismic structure-soil-structure interaction problems for nuclear power plants. *Nuclear Engineering and Design*, *73*(3), 343–363.

Meek, J. W., & Wolf, J. P. (1994). Cone models for embedded foundation. *Journal of Geotechnical Engineering*, *120*(1), 60–80.

Meymand, P. J. (1998). *Shaking table scale model tests of nonlinear soil-pile-superstructure interaction in soft clay*.

Moghadam, M. R., & Baziar, M. H. (2016). Seismic ground motion amplification pattern induced by a subway tunnel: shaking table testing and numerical simulation. *Soil Dynamics and Earthquake Engineering*, *83*, 81–97.

Moncarz, P. D., & Krawinkler, H. (1981). *Theory and application of experimental model analysis in earthquake engineering* (Vol. 50). Stanford University California.

Mononobe, N. (1929). On determination of earth pressure during earthquake. In *Proc. World Engineering Congress* (Vol. 9, pp. 177–185).

Moss, R. E. S., Kuo, S., & Crosariol, V. (2011). Shake table testing of seismic soil-foundation-structure-interaction. In *Geo-Frontiers 2011: Advances in Geotechnical Engineering* (pp. 4369–4377).

Murray, C. A., Hoult, N. A., & Take, W. A. (2017). Dynamic measurements using digital image correlation. *International Journal of Physical Modelling in Geotechnics*, *17*(1), 41–52.

Mylonakis, G., Kloukinas, P., & Papantonopoulos, C. (2007). An alternative to the Mononobe-Okabe equations for seismic earth pressures. *Soil Dynamics and Earthquake Engineering*, *27*(10), 957–969. https://doi.org/10.1016/j.soildyn.2007.01.004

Nakamura, S. (2006). Reexamination of Mononobe-Okabe theory of gravity retaining walls using centrifuge model tests. *Soils and Foundations*, *46*(2), 135–146.

Nakamura, Y. (1989). A method for dynamic characteristics estimation of subsurface using microtremor on the ground surface. *Railway Technical Research Institute, Quarterly Reports*, *30*(1).

Okabe, S. (1924). General theory on earth pressure and seismic stability of retaining wall and dam. *Proc. Civil Engrg. Soc., Japan*, *10*(6), 1277–1323.

Ortiz, L. A., Scott, R. F., & Lee, J. (1983). Dynamic centrifuge testing of a cantilever retaining wall. *Earthquake Engineering & Structural Dynamics*, *11*(2), 251–268.

Ostadan F. (2005) Seismic soil pressure for building walls – an updated approach. J Soil Dyn Earthq Eng (25):785–93.

Paik, K. H., & Salgado, R. (2003). Estimation of active earth pressure against rigid retaining walls considering arching effects. *Geotechnique*, *53*(7), 643–653.

Pais, A., & Kausel, E. (1988). Approximate formulas for dynamic stiffnesses of rigid foundations. *Soil Dynamics and Earthquake Engineering*, *7*(4), 213–227. https://doi.org/10.1016/S0267-7261(88)80005-8

Panah, A. K., Yazdi, M., & Ghalandarzadeh, A. (2015). Shaking table tests on soil retaining walls reinforced by polymeric strips. *Geotextiles and Geomembranes*, *43*(2), 148–161.

Pecker, A., Paolucci, R., Chatzigogos, C., Correia, A. A., & Figini, R. (2014). The role of non-linear dynamic soil-foundation interaction on the seismic response of structures. *Bulletin of Earthquake Engineering*, *12*(3), 1157–1176.

Pitilakis, D., Dietz, M., Wood, D. M., Clouteau, D., & Modaressi, A. (2008). Numerical simulation of dynamic soil–structure interaction in shaking table testing. *Soil Dynamics and Earthquake Engineering*, *28*(6), 453–467.

Politopoulos, I., Sergis, I., & Wang, F. (2015). Floor response spectra of a partially embedded seismically isolated nuclear plant. *Soil Dynamics and Earthquake Engineering*, *78*, 213–217.

Prasad, S. K., Towhata, I., Chandradhara, G. P., & Nanjundaswamy, P. (2004). Shaking table tests in earthquake geotechnical engineering. *Current Science*, 1398–1404.

Psarropoulos, P. N., Klonaris, G., & Gazetas, G. (2005). Seismic earth pressures on rigid and flexible retaining walls. *Soil Dynamics and Earthquake Engineering*, *25*(7–10), 795–809. https://doi.org/10.1016/j.soildyn.2004.11.020

Rayhani, M. T., & El Naggar, M. H. (2012). Physical and numerical modeling of seismic soil-structure interaction in layered soils. *Geotechnical and Geological Engineering*, *30*(2), 331–342.

Richards Jr, R., Huang, C., & Fishman, K. L. (1999). Seismic earth pressure on retaining structures. *Journal of Geotechnical and Geoenvironmental Engineering*, *125*(9), 771–778.

Rocha, M. (1958). The possibility of solving soil mechanics problems by the use of models.

Romero, A., Galvín, P., & Domínguez, J. (2013). 3D non-linear time domain FEM–BEM approach to soil–structure interaction problems. *Engineering Analysis with Boundary Elements*, *37*(3), 501–512.

Roscoe, K. H. (1968). Soils and model tests. *Journal of Strain Analysis*, *3*(1), 57–64.

Sáez, E., Lopez-Caballero, F., & Modaressi-Farahmand-Razavi, A. (2011). Effect of the inelastic dynamic soil–structure interaction on the seismic vulnerability assessment. *Structural Safety*, *33*(1), 51–63.

Saxena, N., & Paul, D. K. (2012). Effects of embedment including slip and separation on seismic SSI response of a nuclear reactor building. *Nuclear Engineering and Design*, *247*, 23–33. https://doi.org/10.1016/j.nucengdes.2012.02.010

Scott, R.F. (1973). Earthquake-induced pressures on retainign walls. In *Proceedings of the 5th World Conference on Earthquake Engineering* (Vol. 2, pp. 1611-1620).

Seed, Harry Bolton. (1970). Soil moduli and damping factors for dynamic response analysis. *EERC*.

Seed, H. B., & Idriss, I. M. (1973). Soil-structure interaction of massive embedded structures during earthquakes. *Proc. 5th Wld Conf. Earthq. Engng*.

Seed, Harry Bolton, & Lysmer, J. (1977). Soil-Structure Interaction Analyses by FEM State of art, *32*(May), 147–156.

Segaline, H., Sáez, E., & Ubilla, J. (2021). Continuous characterization of dynamic soil behavior by Digital Image Correlation in a transparent shear laminar box. *Acta Geotechnica*. https://doi.org/10.1007/s11440-021-01351-1

Segaline, H., Sáez, E., & Ubilla, J. (2022). Evaluation of dynamic soil-structure interaction effects in buildings with underground stories using 1 g physical experimentation in a transparent shear laminar box. *Engineering Structures*, *266*, 114645.

Sherif, M. A., Fang, Y.-S., & Sherif, R. I. (1984). KA and K o Behind Rotating and Non-Yielding Walls. *Journal of Geotechnical Engineering*, *110*(1), 41–56.

Sherif, M. A., Ishibashi, I., & Lee, C. Do. (1982). Earth pressures against rigid retaining walls. *Journal of the Geotechnical Engineering Division*, *108*(5), 679–695.

Smith, W. D. (1974). A nonreflecting plane boundary for wave propagation problems. *Journal of Computational Physics*, *15*(4), 492–503.

Sotiriadis, D., Klimis, N., Margaris, B., & Sextos, A. (2020). Analytical expressions relating free-field and foundation ground motions in buildings with basement, considering soil-structure interaction. *Engineering Structures*, *216*, 110757.

Soto, V., Sáez, E. & Magna-Verdugo (2020), Numerical modeling of 3D site-city effects including partially embedded buildings using spectral element methods. Application to the case of Viña del Mar city, Chile, Engineering Structures, 223, 111188.

Stanier, S. A., Blaber, J., Take, W. A., & White, D. J. (2016). Improved image-based deformation measurement for geotechnical applications, *739*(October 2015), 727–739.

Steedman, R. S., & Zeng, X. (1990). The influence of phase on the calculation of pseudo-static earth pressure on a retaining wall. *Geotechnique*, *40*(1), 103–112.

Stewart, J. P., Fenves, G. L., & Seed, R. B. (1999). Seismic soil-structure interaction in buildings. I: Analytical methods. *Journal of Geotechnical and Geoenvironmental Engineering*, *125*(1), 26–37.

Stewart, J. P., Seed, R. B., & Fenves, G. L. (1998). *Empirical evaluation of inertial soil-structure interaction effects* (Issue 7). Pacific Earthquake Engineering Research Center Univ. of California, Berkeley, CA.

Stewart, J. P., Seed, R. B., & Fenves, G. L. (1999). Seismic soil-structure interaction in buildings. II: Empirical findings. *Journal of Geotechnical and Geoenvironmental Engineering*, *125*(1), 38–48.

Suzuki, K., Babasaki, R., & Suzuki, Y. (1991). Liquefaction Tests by a Laminar Box in a Centrifuge.

Tabatabaiefar, H. R. (2016). Detail design and construction procedure of laminar soil containers for experimental shaking table tests. *International Journal of Geotechnical Engineering*, *10*(4), 328–336. https://doi.org/10.1080/19386362.2016.1145419

Takewaki, I., Takeda, N., & Uetani, K. (2003). Fast practical evaluation of soil-structure interaction of embedded structures. *Soil Dynamics and Earthquake Engineering*, *23*(3), 13–20. https://doi.org/10.1016/S0267-7261(02)00225-7

Tatsuoka, F., & Haibara, O. (1985). Shear resistance between sand and smooth or lubricated surfaces. *Soils and Foundations*, *25*(1), 89–98.

Teng, Y., Stanier, S. A., & Gourvenec, S. M. (2017). Synchronised multi-scale image analysis of soil deformations. *International Journal of Physical Modelling in Geotechnics*, *17*(1), 53–71. https://doi.org/10.1680/jphmg.15.00058

Terzaghi, K. (1936). *A fundamental fallacy in earth pressure computations* (Issue 3). Harvard University.

Todorovska, M. I. (1992). Effects of the depth of the embedment on the system response during building-soil interaction. *Soil Dynamics and Earthquake Engineering*, *11*(2), 111–123. https://doi.org/10.1016/0267-7261(92)90049-J

Tsai, C.-C., Lin, W.-C., & Chiou, J.-S. (2016). Identification of dynamic soil properties through shaking table tests on a large saturated sand specimen in a laminar shear box. *Soil Dynamics and Earthquake Engineering*, *83*, 59–68.

Tsai, N. C., Niehoff, D., Swatta, M., & Hadjian, A. H. (1974). The use of frequency-independent soil-structure interaction parameters. *Nuclear Engineering and Design*, *31*(2), 168–183.

Turan, A., Hinchberger, S. D., & El Naggar, H. (2009). Design and commissioning of a laminar soil container for use on small shaking tables. *Soil Dynamics and Earthquake Engineering*, *29*(2), 404–414.

Turan, A., Hinchberger, S. D., & El Naggar, M. H. (2013). Seismic soil–structure interaction in buildings on stiff clay with embedded basement stories. *Canadian Geotechnical Journal*, *50*(8), 858–873.

Ulgen, D., Saglam, S., & Ozkan, M. Y. (2015). Dynamic response of a flexible rectangular underground structure in sand: centrifuge modeling. *Bulletin of Earthquake Engineering*, *13*(9), 2547–2566.

Veletsos, A., & Younan, A. (1994). Dynamic soil pressures on rigid vertical walls. *Earthquake Engineering & Structural Dynamics*, *23*(3), 275–301.

Veletsos, Anestis S, & Younan, A. H. (1997). Dynamic response of cantilever retaining walls. *Journal of Geotechnical and Geoenvironmental Engineering*, *123*(2), 161–172.

Veletsos, A. S., & Verbič, B. (1973). Vibration of viscoelastic foundations. *Earthquake Engineering & Structural Dynamics*, *2*(1), 87–102.

Veletsos, A. S., and Younan, A. H. (1994). "Dynamic Modeling and Response of Soil-Wall Systems." J. Geotech. Eng., 120 (12), pp. 2155-2179

Wang, H. feng, Lou, M. lin, Chen, X., & Zhai, Y. mei. (2013). Structure-soil-structure interaction between underground structure and ground structure. *Soil Dynamics and Earthquake Engineering*, *54*, 31–38. https://doi.org/10.1016/j.soildyn.2013.07.015

Wang, K.-L., & Lin, M.-L. (2011). Initiation and displacement of landslide induced by earthquake—a study of shaking table model slope test. *Engineering Geology*, *122*(1–2), 106–114.

Wagner N and Sitar N (2016) On seismic response of stiff and flexible retaining structures. Soil Dynamics and Earthquake Engineering 91: 284–293.

White, D. J., Take, W. A., & Bolton, M. D. (2003). Soil deformation measurement using particle image velocimetry (PIV) and photogrammetry. *Geotechnique*, *53*(7), 619–631. https://doi.org/10.1680/geot.2003.53.7.619

White, David J, Take, W. A., & Bolton, M. D. (2001). Measuring soil deformation in geotechnical models using digital images and PIV analysis. In *10th international conference on computer methods and advances in geomechanics* (pp. 997–1002).

Wilson, P., & Elgamal, A. (2015). Shake table lateral earth pressure testing with dense c-ϕ backfill. *Soil Dynamics and Earthquake Engineering*, *71*, 13–26. https://doi.org/10.1016/j.soildyn.2014.12.009

Wolf, J. P., & Obernhuber, P. (1985). Non-linear soil-structure-interaction analysis using dynamic stiffness or flexibility of soil in the time domain. *Earthquake Engineering & Structural Dynamics*, *13*(2), 195–212.

Wolf, J. P. (1989). Soil-structure-interaction analysis in time domain. *Nuclear Engineering and Design*, *111*(3), 381–393.

Wood, D. M., Crewe, A., & Taylor, C. (2002). Shaking table testing of geotechnical models. *International Journal of Physical Modelling in Geotechnics*, *2*(1), 1–13.

Wood, J. H. (1975). Earthquake induced pressures on a rigid wall structure. *Bulletin of the New Zealand Society for Earthquake Engineering*, *8*(3), 175–186.

Wood, J.H. (1973). Earthquake induced soil pressures on structures. PhD thesis, California Institute of Technology, Pasadena.

Zeghal, M., Elgamal, A.-W., Tang, H. T., & Stepp, J. C. (1995). Lotung downhole array. II: Evaluation of soil nonlinear properties. *Journal of Geotechnical Engineering*, *121*(4), 363–378.

Zeghal, M., Elgamal, A.-W., Zeng, X., & Arulmoli, K. (1999). Mechanism of liquefaction response in sand–silt dynamic centrifuge tests. *Soil Dynamics and Earthquake Engineering*, *18*(1), 71–85.

Zhang, Z., Wei, H., & Qin, X. (2017). Experimental study on damping characteristics of soil-structure interaction system based on shaking table test. *Soil Dynamics and Earthquake Engineering*, *98*, 183–190.

Zhang, P., Peterson, S. D., & Porfiri, M. (2019). Combined particle image velocimetry/digital image correlation for load estimation. *Experimental Thermal and Fluid Science*, *100*, 207–221.